

TIME-DEPENDENT DESCRIPTION OF HEAVY-ION COLLISIONS

By

Hao Lin

A DISSERTATION

Submitted to
Michigan State University
in partial fulfillment of the requirements
for the degree of

Physics – Doctor of Philosophy

2020

ABSTRACT

TIME-DEPENDENT DESCRIPTION OF HEAVY-ION COLLISIONS

Hao Lin

In this thesis, we aim to advance the time-dependent transport theories for the description of heavy-ion collisions, from two perspectives. As an attempt to address multifragmentation in nuclear collisions, we develop a stochastic transport model based on one-body Langevin dynamics. The new model is subsequently tested and benchmarked with a series of other existing models with satisfaction. The model is also applied to address and confirm the so-called “hierarchy effect” observed in the multifragmentation for certain systems around Fermi energies. Parallel to the development towards a stochastic theory, we also extend an approach based on non-equilibrium Green’s function for the description of correlated nuclear systems in one dimension.

Firstly, we present a new framework to treat the dissipation and fluctuation dynamics associated with nucleon-nucleon scattering in heavy-ion collisions. The two-body collisions are effectively described in terms of the diffusion of nucleons in viscous nuclear media, governed by a set of Langevin equations in momentum space. The new framework combined with the usual mean-field dynamics, forming the basis of the new stochastic model, can be used to simulate heavy-ion collisions at intermediate energies.

Subsequently, as a proof of principle for the new model, we simulate Au + Au reactions at 100 MeV/nucleon and at 400 MeV/nucleon and look at observables such as rapidity distribution and flow as a function of rapidity.

The results are found to be consistent with other existing models under the same constrained conditions. To demonstrate the model’s ability to describe multifragmentation, we also study the formation of fragments in Sn + Sn reactions at 50 MeV/nucleon, and the fragment distribution and properties are discussed and compared to two other models commonly employed for collisions.

Next, we move on to tackle the “hierarchy effect” observed experimentally for reactions around Fermi energies. We simulate Ta + Au at 39.6 MeV/nucleon and compare mainly the charge and velocity distributions of the projectile-like fragments with experimental data. Our simulation results can reproduce the trends observed in data, and a semi-quantitative agreement can be reached. This is the first time, to our knowledge, that one has succeeded in addressing the “hierarchy effect” with a dynamical model. The simulation of U + C is also discussed.

Finally, we present a fully quantum-mechanical model based on non-equilibrium Green’s function, with short-range two-body correlations incorporated as an extension. We examine its applications to one-dimensional nuclear systems, such as the preparation and properties of the ground states, the isovector oscillation of symmetric systems and the boosting of a “slab” in a periodic box. In particular, the dissipation brought by two-body correlations and the Galilean covariance of the theory are demonstrated. These studies lay the ground for the future exploration of collisions of correlated nuclear systems in one dimension.

ACKNOWLEDGEMENTS

I would first like to thank my advisor, Paweł Danielewicz, for not only his academic guidance but also his support, patience and liberty. He is that kind of liberal and laid-back person, who would not complain about my not following his words and meandering with little progress. I can be pessimistic and, at times, depressed, and his kindness and optimism never fail to ease my nerves and lighten me up a bit. I also appreciate that he has provided me with a great many support and opportunities to travel and to attend conferences, and that he would go the extra mile to hunt for job opportunities for me and connect me to people.

I am grateful to my other committee members, Betty Tsang, Carlo Piermarocchi, Filomena Nunes, Gary Westfall, and Morten Hjorth-Jensen, for their guidance, be it critical questions or heartfelt advice, and for, of course, putting up with my talks every year.

I would also like to thank Scott Pratt and Maria Colonna for fruitful discussions and suggestion and for their time and efforts in writing references for me. I also want to say thank you to Hermann Wolter for providing me with a comfortable and hospitable stay in Munich as well as offering references.

I also want to thank Elizabeth Deliyski and Gillian Olsen for their diligent work and assistance along the way, especially when I had created mess before and after my trips. Among my favorite lecturers at MSU are Scott Bogner, Morten Hjorth-Jensen and Vladimir Zelenvinsky.

The spiritual support and accompany of my peers means a great deal to me. I shall take this opportunity to send my gratitude and best wishes to my cohort including, but not limited to, Maxwell Cao, Mengzhi Chen,

Xian-Gai Deng, Linda H'lophe, Jun Hong, Tong Li, Kuan-Yu Lin, Dan Liu, Jian Liu, Amy Lovell, Hossein Mahzoon, Xingze Mao, Zachary Matheson, Pierre Nzabahimana, Avik Sakar, Tommy Tsang, Jonathan Wong, Heda Zhang, Boyao Zhu, Kuan Zhu ... and, last but not least, whoever is reading this!

Contents

List of Figures	ix
List of Tables	xvi
1 Introduction	1
1.1 Heavy-Ion Collisions	1
1.2 Transport Models	4
1.3 Fluctuations and Quantum effects	7
1.4 Outline	10
2 One-body Langevin transport model	11
2.1 Introduction	11
2.2 Formulation	13
2.2.1 The Boltzmann framework	13
2.2.2 The mean-field dynamics	14
2.2.3 The dissipation and fluctuation dynamics	15
2.2.4 Initialization with the Thomas-Fermi equations	19
2.2.5 Brownian motions of nucleon wave-packets	21
3 Applications to heavy-ion collisions at intermediate energies	30
3.1 Benchmarks	30

3.1.1	One-body observables for Au + Au system	31
3.1.2	Fragmentation dynamics with Sn + Sn at 50 MeV/nucleon	37
3.1.3	Summary and discussion	42
4	Investigating “hierarchy effect” in multifragmentation at Fermi energies with the Brownian motion model	45
4.1	Simulation setup: physical inputs and selection of impact parameter b	46
4.2	Comparison with experimental data	49
4.2.1	Charge distribution	53
4.2.2	Velocity distribution	57
4.3	Absence of the “hierarchy effect” for U + C	63
4.4	Summary	64
5	Nonequilibrium Green’s function approach for many-body quantum systems	66
5.1	Introduction	66
5.2	Extending the non-equilibrium Green’s function approach for nuclear systems	70
5.3	Preparing finite correlated nuclear systems	76
5.4	Exploring dissipation with isovector oscillation in a finite system	86
5.5	Galilean Covariance	91
5.6	Summary and future prospects	93
6	Conclusion	97
Appendix A Fokker-Planck equation and Langevin equation		100

Appendix B Generalized Einstein relation in thermal equilibrium	104
Bibliography	106

List of Figures

1.1 Schematics of heavy-ion collisions in the center of mass frame. The left part depicts the two approaching nuclei, and b is the so-called impact parameter. The dotted lines are boundaries of the overlap regions. The right part depicts the aftermath of the collisions: the colored dots in the central region represent the nucleons as well as possible new particles generated in the participant zone; the two “caps” flying off are knowns as the spectators. This figure is taken from [1].	3
1.2 Illustration of the effects of fluctuations in HIC. Under stable conditions void of fluctuations on the left panel, the dynam- ical trajectories of identically prepared systems tend to be very much similar, leading to a unique outcome. The right panel shows that trajectories can spread out in the prescence of fluctuations during the evolution and end up in diverse configurations. This figure is taken from [2].	8
2.1 (Color online) Density profiles of stable nuclei ^{58}Ni and ^{197}Au obtained from solutions of the Thomas-Fermi equations. . .	28
2.2 (Color online) Time evolution of radial density profiles for single nuclei ^{58}Ni and ^{197}Au in steps of 40 fm/c.	29

- 3.1 (Color online) Final rapidity distributions as a function of reduced rapidity for $^{197}\text{Au} + ^{197}\text{Au}$ at beam energies of 100 MeV/nucleon (upper panel) and 400 MeV/nucleon (lower panel) at an impact parameter $b = 7$ fm. Solid curves, dashed curves and the dashed-dot curve correspond to the Brownian model, BUU-type models, and QMD-type models [3], respectively. 32
- 3.2 (Color online) Final average in-plane flow as a function of reduced rapidity for $^{197}\text{Au} + ^{197}\text{Au}$ collisions at beam energies of 100 MeV/nucleon (upper panel) and 400 MeV/nucleon (lower panel) and an impact parameter $b = 7$ fm. Solid curves, dashed curves and the dashed-dot curve represent the Brownian model, BUU-type models, and QMD-type models [3], respectively. 34
- 3.3 (Color online) Flow slope parameter for different transport models [3] for $^{197}\text{Au} + ^{197}\text{Au}$ collisions at beam energies of 100 MeV/nucleon (blue squares) and 400 MeV/nucleon (red triangles) at an impact parameter $b = 7$ fm. The error bars represent the fitting uncertainties. These become invisible when they are smaller than the symbols. The colored bands correspond to roughly 52% confidence intervals from the statistics of calculations from both the BUU-type and the QMD-type models. (See text for a more detailed explanation.) 35

3.5 (Color online) Density contours for nucleons projected onto the reaction plane in the reaction $^{112}\text{Sn} + ^{112}\text{Sn}$ at 50 MeV/nucleon at an impact parameter of $b = 0.5$ fm, at different times during the reaction. Results calculated with the Brownian motion model are displayed in the first row of the panels. The bottom two rows show results from SMF and AMD calculations [4]. The densities for the projected contours start at 0.07 fm^{-2} and consecutively increase by 0.1 fm^{-2}	38
3.6 (Color online) Distribution of IMF multiplicity obtained from different models for the reaction $^{124}\text{Sn} + ^{124}\text{Sn}$ at 50 MeV/nucleon at an impact parameter $b = 0.5$ fm. The upper panel shows the multiplicity distribution of IMFs with charge $Z > 2$ and the lower panel with $Z > 6$ [4].	41
4.1 Centrality analysis of the events in the simulation. (a) shows the distribution of the actual impact parameter b sampled in the simulation; (b) shows the histograms of b for each event group of definite PLF multiplicity M_{IMF} ; (c) shows the distributions of centrality estimator $E_{t12}/E_{\text{c.m.}}$ for each event group specified by M_{IMF} ; (d) displays the relationship between $E_{t12}/E_{\text{c.m.}}$ and b within the events that are color-coded by their corresponding M_{IMF}	47

4.4 Means and standard deviations of the charge distributions sorted by the multiplicity M_{IMF} in ascending order from left to right and by the impact parameter b in ascending order from top to bottom. The distributions within each panel are further ranked by their corresponding charge Z and color-coded. Theoretical means are represented by asterisks, and experimental ones are by open circles. Standard deviations are represented as “error bars”.	56
4.5 Means and standard deviations of the distribution of parallel velocity V_z , organized in a way similar to Fig. 4.3.	58
4.6 Density plots of two simulated events at 180 fm/c. Event (a) is central, while event (b) is semi-peripheral. The density contours are ranked by $0.1 \rho_0, 0.2 \rho_0, 0.4 \rho_0, 0.6 \rho_0$ and $0.8 \rho_0$ from the outermost to the innermost. Neither case provides any direct proof of the neck formation.	60
4.7 Means and standard deviations of the distribution of parallel velocity V_z , sorted by the impact parameter b in the simulation and organized in a way similar to Fig. 4.4.	62
5.1 Second-order direct Born diagrams for neutron and proton self-energies $\Sigma_{n/p}$. Note that the particle species in the loop can be the same as or the opposite of the species of the propagator in the line to the left of the diagram. In the present work, the interaction transfers no isospin within the Born diagram, making the scattering independent of isospin.	72

5.7 Evolution of the lowest three moments of the neutron slab. The red lines and the black lines correspond to calculations with mean field only and the full calculations, respectively.	89
5.8 Evolution of density for a correlated $N = Z = 2$ slab boosted with velocity $V = 0.176 c$. The initial density is illustrated with a dash-dotted line in every panel. The panels (b)-(d) show evolution advanced subsequently over $30 \text{ fm}/c$, with the latest profile illustrated with a solid line. Intermediate pro- files at every $15 \text{ fm}/c$ are illustrated with dashed lines. . . .	93

List of Tables

2.1 Parameters for the mean-field interaction.	15
5.1 Parameters for the auxiliary field in Eq. (5.13).	75

Chapter 1

Introduction

The work presented in this thesis aims to bring new developments to transport theories on nuclear collisions. To address the phenomenon of multi-fragmentation, I developed a new stochastic transport model that treats the dissipation and fluctuations tied to two-body correlations on an equal footing. Towards a fully quantum-mechanical transport theory, I studied the non-equilibrium Green's function theory and applied it to describe one-dimensional nuclear systems.

In the following sections, I will briefly introduce heavy-ion collisions and the transport models for describing them. The introduction will be followed by a discussion of incorporating fluctuation and quantum effects into transport models, where both motivation and some state-of-the-art attempts will be presented. An outline of the upcoming chapters will be given in the end.

1.1 Heavy-Ion Collisions

In this thesis, we will focus on heavy-ion collisions (HIC) at intermediate energies. These are very involved nuclear processes, in which a heavy

projectile, typically with a mass number $A > 4$, impinges on another heavy target at an incident energy ranging from tens of MeVs up to a few GeVs per nucleon.

The two nuclei come into contact quickly afterwards, and a finite system composed of hot and dense nuclear matter is formed as the two nuclei compress against one another. The temperature and density achieved in the compression phase may depend critically on the incident energies and the alignment of the centers of the two nuclei (also known as centrality). In general, a higher incident energy and a greater centrality will result in hotter and denser matter. With varying incident energies and projectile-target pairs, HIC allows one to probe the properties of nuclear Equation of State (EoS), especially those with strong dependence on density, and is therefore a popular playground for both experimentalists and theorists. The study of nuclear EoS through HIC is of particular interest to astrophysicists, as the behaviors of the nuclear EoS beyond twice saturation density ($\rho_0 = 0.16 \text{ fm}^{-3}$) affect properties of neutron stars, such as the mass-radius relation [6] and the tidal deformability [7]. For now, HIC experiment is the closest thing that one can perform to achieve the high density nuclear environment of neutron stars on Earth. At the other end of the spectrum concerning the low-density behaviors of the nuclear EoS, the possible liquid-gas phase transition [8, 9] and the possible consequences of multifragmentation [10, 11] and formation of exotic structures [12] also received a fair amount of attention in the recent decades.

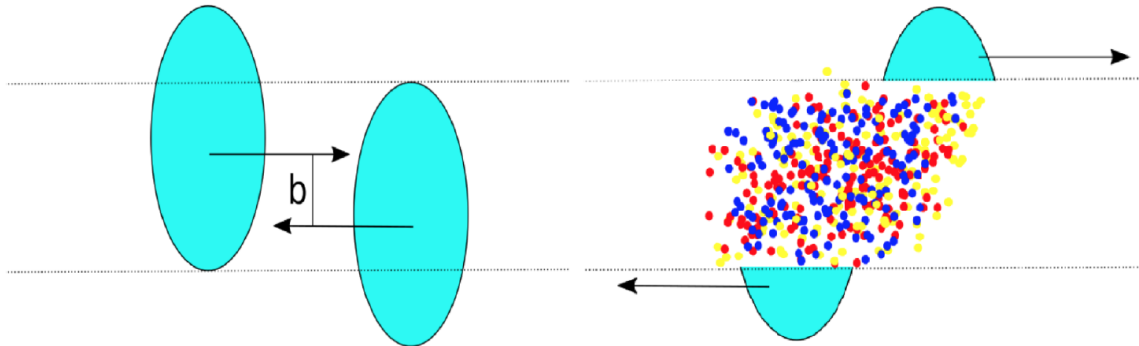


Figure 1.1: Schematics of heavy-ion collisions in the center of mass frame. The left part depicts the two approaching nuclei, and b is the so-called impact parameter. The dotted lines are boundaries of the overlap regions. The right part depicts the aftermath of the collisions: the colored dots in the central region represent the nucleons as well as possible new particles generated in the participant zone; the two “caps” flying off are knowns as the spectators. This figure is taken from [1].

Fig. 1.1 depicts schematically a simplified scenario of the collisions of two heavy-nuclei in the center-of-mass frame, with the initial stage on the left and the nearly-final stage on the right. Such a phenomenological description of HIC is usually known as the fireball model [13]. On the left-hand-side of Fig. 1.1, the misalignment the b is often referred to as the impact parameter, which is a geometrical measure of the overlap of the two nuclei. The smaller b is, the greater the overlap is. If one ignores the minute Fermi motion in the transverse directions, only the nucleons lying within the overlap region of the two nuclei can interact and slow down and they are known as the participants. The other nucleons, referred to as the spectators, outside the overlap region will just fly away as there are

no opposing nucleons to stop them. It is in the participant regions that nucleons are actively and frequently interacting and bouncing off one another. Nucleons in the central region will ultimately decompress, fall apart and be caught by detectors. By measuring the distributions of the final particles, clusters and fragments and comparing the results to theoretical simulations, one may hopefully obtain some constraints on the expected behaviors of the nuclear EoS.

1.2 Transport Models

HIC differs from few-body direct reactions in terms of the large degrees of freedom involved as well as the more complex reaction processes with many more steps. The fireball model [13] mentioned previously is a simple phenomenological model to capture the essence of HIC. As more details and sophistication were presented by HIC experiments over time, fully many-body and microscopic theoretical descriptions of HIC were called for.

One of the very first microscopic models used for comparison with experimental data is the cascade model [14]. The cascade model describes both the positions and momenta of all the nucleons in the system in a time-dependent manner. The interaction among nucleons comes solely from the two-body nucleon-nucleon scatterings, which are usually simulated by a geometric means. Within the same time step, one checks the closest approaches of all possible nucleon-nucleon pairs. For pairs with a closest approach $d < \sqrt{\sigma(\sqrt{s})/\pi}$, where \sqrt{s} is the relative energy of the two nucleons and σ is the energy-dependent total cross section, one sam-

ples randomly the final momenta of the pair from the underlying angular differential cross section. This type of geometric treatment is still used as a paradigm of two-body scatterings in many of the more up-to-date transport models.

A serious problem with the cascade model is that nuclei tend to fall apart far too quickly due to the lack of a potential that binds and stabilizes the nucleons. And the cascade plus mean field model came later as an improvement. A popular choice of mean field parametrization is the so-called Skyrme parametrization. The simplest form of a mean field potential reads $U(\rho) = A(\rho/\rho_0) + B(\rho/\rho_0)^\sigma$, where $A < 0$, $B > 0$ and $\sigma > 1$. The parameters are typically adjusted to reproduce nuclear matter properties. More sophisticated forms of the mean-field parametrization as well as discussion will be presented in Chapter 2. With the inclusion of mean field, positions and momenta of individual nucleons are updated according to Hamilton's equation (see more details in Chapter 2), on top of the geometric treatment of the hard nucleon-nucleon scatterings.

Another issue with the naive cascade model is the violation of Pauli exclusion principle. As a remedy, one can impose a Pauli-blocking probability for each hard two-body scattering.[15] Let the initial momenta of a pair of colliding nucleons be $(\mathbf{r}_1, \mathbf{p}_1)$ and $(\mathbf{r}_2, \mathbf{p}_2)$, and the final momenta be $(\mathbf{r}_1', \mathbf{p}_1')$ and $(\mathbf{r}_2', \mathbf{p}_2')$. Note that initial and final positions are not altered in the cascade approach. One builds two spherical phase space regions of radius R in coordinate space and of radius P in momentum space around $(\mathbf{r}_1, \mathbf{p}_1')$ and $(\mathbf{r}_2, \mathbf{p}_2')$ and finds out the respective phase space occupancy $f = N/N_{\max}$, where $N_{\max} = (4\pi/3)^2(RP/h)^3$ and N is the number of nucleons in the region under consideration. The scattering is allowed with

a probability of $\max\{(1 - f_1')(1 - f_{2'}), 0\}$. There is, unfortunately, not a universal and/or all-around prescription of the radii R and P though. For a smoother and more accurate description of the phase space occupancy, one can also consider representing a nucleon by a group of test particles. Some relevant discussions can be found in Chapter 2.

With the incorporation of mean-field dynamics and the Pauli-blocking procedure on top of the raw cascade model, we, in effect, obtain a simulation method based on the Boltzmann-Uehling-Uhlenbeck (BUU) equation.

$$\frac{\partial f_1}{\partial t} + \frac{\mathbf{p}_1}{m} \frac{\partial f_1}{\partial \mathbf{r}} - \frac{\partial U}{\partial \mathbf{r}} \frac{\partial f_1}{\partial \mathbf{p}_1} = \frac{g}{h^3} \int d\mathbf{p}_2 d\Omega v_{12} \frac{d\sigma}{d\Omega} \times \left(\tilde{f}_1 \tilde{f}_2 f_{1'} f_{2'} - f_1 f_2 \tilde{f}_{1'} \tilde{f}_{2'} \right), \quad (1.1)$$

where $f_1 = f(\mathbf{r}, \mathbf{p}_1, t)$ is the phase space density, U is the mean-field potential, g is the degeneracy factor, $\frac{d\sigma}{d\Omega}$ is the NN-differential cross section, and $\tilde{f} = 1 - f$. The left-hand-side of the equation governs the mean-field dynamics, and on the right is the two-body collision term, which describes how binary collisions of the form $(1, 2) \longleftrightarrow (1', 2')$ induce depletion (\rightarrow) and accretion (\leftarrow) of particles at the phase space site 1.

The BUU equation Eq. (1.1) serves as the foundation of the two major types of transport models for HIC frequently used nowadays: the BUU type and the QMD type. The BUU-type models tend to be more truthful in solving the BUU equation with the test particle techniques, combining elements of the mean-field evolution and the cascade model. The QMD-type models represent nucleons as rigid wavepackets of finite extension and simulate the mean-field evolution and the binary collision of the centroids of those wavepackets. Numerical fluctuations in the QMD-type models are generally not washed out as they are in the case of the BUU-type models,

but QMD-type models do tend to suffer from issues of violation of Pauli principle. More discussion regarding the Boltzmann equation as well as the traditional transport models will be given in Chapter 2.

1.3 Fluctuations and Quantum effects

The Boltzmann equation Eq. (1.1) represents a truncation up to two-body correlations in the Bogoliubov–Born–Green–Kirkwood–Yvon (BBGKY) hierarchy, and thus cannot be the whole story. The deterministic nature of the Boltzmann equation predicts a single averaged evolution trajectory for HIC, as is illustrated on the left of Fig. 1.2, which is clearly at odds with the diverse fragmentation in HIC observed in experiments [16, 17].

The formation of light clusters relies on beyond-two-body (e.g. 3-body, etc.) correlations, and the production of IMFs is thought to be the result of the spinodal decomposition seeded by density fluctuations. Incorporating many-body correlations, even on a semi-classical level, is prohibitively complex. Alternatively, one may introduce the effects of higher-order correlations as fluctuations in phase space. The effects of higher-order correlations scale like ρ^n , where n is the order, and they are perturbatively small when the density is low. The erratic and complex behaviors of higher-order correlations, although not random in a strict sense in the semi-classical theory, render them highly sensitive to initial conditions and hence unpredictable, which justifies a stochastic treatment of the perturbations, leading to the introduction of fluctuations into transport models.

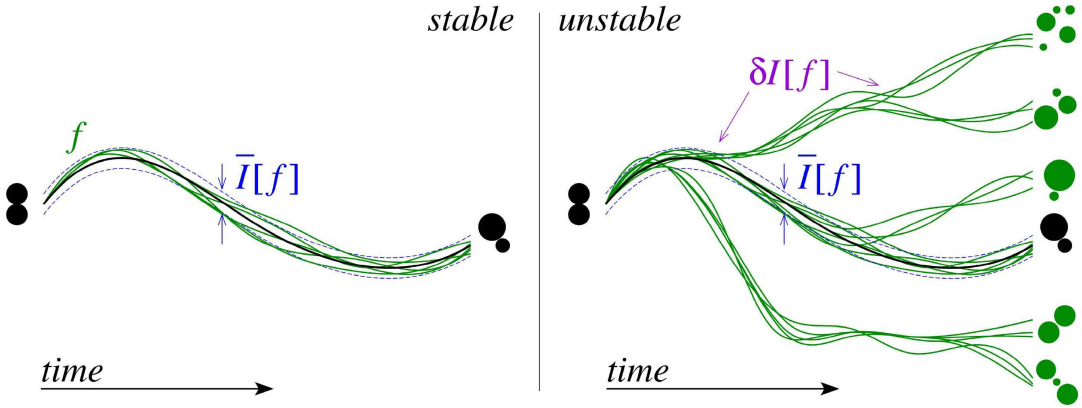


Figure 1.2: Illustration of the effects of fluctuations in HIC. Under stable conditions void of fluctuations on the left panel, the dynamical trajectories of identically prepared systems tend to be very much similar, leading to a unique outcome. The right panel shows that trajectories can spread out in the presence of fluctuations during the evolution and end up in diverse configurations. This figure is taken from [2].

The so-called Boltzmann-Langevin (BL) equation [2, 18] has been introduced to include the fluctuation $\delta I[f]$ of the averaged collision integral $\langle I_{\text{coll}}[f] \rangle$,

$$\frac{\partial f}{\partial t} + \frac{\mathbf{p}}{m} \frac{\partial f}{\partial \mathbf{r}} - \frac{\partial U}{\partial \mathbf{r}} \frac{\partial f}{\partial \mathbf{p}} = \langle I_{\text{coll}}[f] \rangle + \delta I[f]. \quad (1.2)$$

The fluctuation term $\delta I[f]$ is typically assumed to be normally distributed with a vanishing mean and a variance equal to $\langle I_{\text{coll}}[f] \rangle$. [2] The inclusion of $\delta I[f]$ induces fluctuations in the phase space density f along the evolution and drives the system towards a wide variety of exit channels, as is illustrated on the right of Fig. 1.2.

The BL equation provides a formalism of the incorporation of fluctuations, the most truthfully exact numerical implementation of which is only available in two dimension [19–21] to my best knowledge. Some attempts of treating fluctuations [22] in transport theory indeed predate the birth of BL equation, while many of the other modern stochastic transport models

[23, 24] amount to approximate solutions of the BL equation in one way or another. The stochasticity of most of the QMD-type models is largely statistical in nature, with the use of wavepackets of finite extension, whose tie to the BL equation is perhaps even less clean-cut. As such, the BL equation needs not be treated as the gold standard of stochastic treatment in semi-classical transport theories. In Chapter 2, I will bring up my work of treating the dissipation and fluctuation dynamics in HIC, from a rather different starting point and perspective.

So far, we have discussed only semi-classical transport theories, which do come with some limitations, in spite of their simplicity and success in interpreting HIC physics: 1. New approaches and techniques in other fields of nuclear physics are mostly on a quantum mechanical basis, which makes them difficult to be promptly transferred and applied to the semi-classical transport models; 2. An exact antisymmetrization is also hard to achieve in semi-classical models, as they often suffer from imperfections in enforcing the Pauli-blocking in binary collisions [25]; 3. It remains largely unknown how large a role quantum correlations play in HIC physics.

The Time-Dependent Hatree Fock (TDHF) theory has been developed for low-energy nuclear collisions [26, 27]. The dissipation in TDHF, however, originates solely from mean-field dynamics, which is insufficient for collisions at higher energies. The Time-Dependent Density Matrix (TDDM) theory [28], for instance, has been developed to take into account of two-body correlations, but its application has mostly been restricted to collective vibrations [29] and fusion [30] at this point, due to its complexity. Alternative attempts, such as the Stochastic Mean-Field (SMF) approach by Ayik *et al.* [28, 31] and the Stochastic-TDHF (STDHF) [32] theory have

also been made to incorporate beyond-mean correlations by introducing either initial fluctuations or continuous random noise during the evolution, which should simplify the calculations in principle. Yet, applications of these stochastic quantum approaches target predominantly low-energy nuclear collisions [28]. In Chapter 5, we will present a quantum-mechanical transport model based on the theory of non-equilibrium Green’s function. The model includes short-range two-body correlations to mimic binary collisions in semi-classical models, which should provide sufficient stopping for intermediate-energy HIC.

1.4 Outline

Chapter 2 will give a formal introduction and formulation of the stochastic transport model based on one-body Langevin dynamics, followed by some applications to heavy-ion collisions and benchmarks with other models in Chapter 3. In Chapter 4, I will attempt to address the “hierarchy effect” in multifragmentation observed in experiment with the new model. In Chapter 5, I will turn to the quantum transport approach based on non-equilibrium Green’s function and discuss its application to nuclear systems in one dimension. Finally, a summary and conclusion will be given in Chapter 6.

Chapter 2

One-body Langevin transport model

2.1 Introduction

In heavy-ion collisions at modest energies, two nuclei approach and collide to form a composite nuclear system. At very low incident energies and moderate charges, the system tends to remain fused and de-excites by emission of a few nucleons and light clusters. The picture gains in complexity as the incident energy increases, since more energy is available for the system to populate a greater volume of phase space leading up to a plethora of exit channels. In violent collisions, the composite nuclear system formed is highly excited, and its evolution can be envisioned to be very sensitive to the instabilities present in the system. These instabilities may deform the shape of the system in phase space in an exotic manner, resulting in a breakup into multiple fragments.

The fragmentation phenomenon was experimentally observed [33] as early as in the late 1970s. Since the early 1990s, more experimental efforts have been devoted to the study of intermediate-mass-fragment multiplicities [34].

On the other hand, while different transport models have been success-

fully applied to describe many one-body observables, our understanding and treatments of the fragmentation mechanism have yet to be reconciled. The inclusion of fluctuations into transport theories is expected to be of particular importance. It is worth noting that heavy-ion collision experiments make observations and measurements over an *ensemble* of nearly identically prepared colliding systems, and that experimental observables reflect the distribution of all possible outcomes of that ensemble. Angular cross sections, for example, are directly obtained from the angular distribution of the deflected particles, but not from any individual, isolated event. On the contrary, a vast number of the semi-classical transport models are deterministic in nature. These models predict a single exit channel in principle. This poses little trouble when the underlying distribution of outcomes is sharp and narrow. Ensemble averages from transport calculations also prove to converge very well to one-body observables with only weak dependence on channels, such as those concerning collective flows [35, 36]. However, the configurations in multifragmentation are obviously heavily dependent on the exit channels, and, in fact, on the intermediate channels as well. It requires the transport models to be able to explore a wide range of dynamical trajectories. The inclusion of fluctuations creates branching points in the evolution of the system allowing for jumps among different states including those susceptible to instabilities.

In general, there are two major types of transport models for simulating heavy-ion collisions. One type of approaches are essentially molecular dynamics of nucleons represented by single-particle wave-packets, augmented by a phenomenological two-body collision term of the wave-packets [37–58]. The propagation and scattering of localized wave-packets help preserve

the many-body correlations, and the stochastic treatment of the two-body scattering introduces fluctuations. The other type of approaches aim at directly solving the Boltzmann-Uehling-Uhlenbeck (BUU) equation, with the system characterized by a one-body phase space distribution function [23, 24, 59–75]. Solving the BUU equation yields the deterministic time evolution of the one-body distribution function leading to a single exit channel. In recognition of the importance of fluctuations, many efforts have been made to extend the Boltzmann framework, such as the derivation of the Boltzmann-Langevin equation by Ayik and Gregoire [76, 77], the Stochastic Mean Field (SMF) model by Colonna *et al.* [23], and recently the Boltzmann-Langevin-One-Body (BLOB) dynamics by Napolitani and Colonna [24]. Meanwhile, the inclusion of few-body scatterings in the pBUU model by Danielewicz [78] also describes the production of light clusters with mass $A < 4$.

2.2 Formulation

In this section, we will explain the formulation of the Brownian motion model and discuss the details of the implementation of the simulation code.

2.2.1 The Boltzmann framework

In semi-classical transport theories [15], the nuclear system is often characterized by the one-body phase space distribution function $f(\mathbf{r}, \mathbf{p}, t)$. The time evolution of the distribution function f is approximated with the Boltzmann equation,

$$\frac{\partial f}{\partial t} + \{f, \mathcal{H}\} = I_{coll}. \quad (2.1)$$

The self-consistent Hamiltonian \mathcal{H} encompasses all information about the nuclear mean field interaction as well as Coulomb interaction, while the residual two-body interaction, mainly nucleon-nucleon scattering, enters through the collision integral I_{coll} . The Boltzmann equation provides us with a simple deterministic model to study heavy-ion collisions theoretically. Numerical simulations under the Boltzmann framework can be carried out by means of the test-particle method [15, 79].

2.2.2 The mean-field dynamics

Neglecting the collision integral in the Boltzmann equation (2.1), we recover the so-called Vlasov equation,

$$\frac{\partial f}{\partial t} + \{f, \mathcal{H}\} = \frac{\partial f}{\partial t} + \frac{\mathbf{p}}{m} \cdot \nabla_{\mathbf{r}} f - \nabla_{\mathbf{r}} U \cdot \nabla_{\mathbf{p}} f = 0, \quad (2.2)$$

where $\mathcal{H} = \mathcal{T} + \mathcal{V}$ and the mean field $U = \delta\mathcal{V}/\delta\rho$.

The Vlasov equation retains only one-body information. The interaction between any individual particle and the rest of the system is approximated by a mean-field interaction. In practical calculations, the phenomenological mean-field interactions are usually employed,

$$U_{n/p}(\rho(\mathbf{r}), \delta(\mathbf{r})) = A \left(\frac{\rho(\mathbf{r})}{\rho_0} \right) + B \left(\frac{\rho(\mathbf{r})}{\rho_0} \right)^D + \frac{C}{\rho_0^{2/3}} \nabla^2 \left(\frac{\rho(\mathbf{r})}{\rho_0} \right) \pm 2S_{\text{iso}} \left(\frac{\rho(\mathbf{r})}{\rho_0} \right) \delta(\mathbf{r}), \quad (2.3)$$

where $\delta = (\rho_n - \rho_p)/\rho$ is the isospin asymmetry and parameters A , B , C , D , and S_{iso} , summarized in Table I, are fitted to reproduce nuclear matter properties at normal density $\rho_0 = 0.16 \text{ fm}^{-3}$: the binding energy of 16 MeV/nucleon, the incompressibility of 240 MeV and the symmetry energy of 30.3 MeV at normal density ρ_0 [3, 79]. Spin dependence and momentum dependence is ignored for simplicity in this parametrization.

A [MeV]	B [MeV]	C [MeV]	D	S_{iso} [MeV]
-209.2	156.4	-6	1.35	18

Table 2.1: Parameters for the mean-field interaction.

The Coulomb potential $U_{\text{Coul}}(\rho_{\text{ch}}(\mathbf{r}))$ can be determined from the Poisson's equation for electrostatics,

$$\nabla^2 U_{\text{Coul}} = -\frac{1}{\epsilon_0} \rho_{\text{ch}}(\mathbf{r}). \quad (2.4)$$

In the current model, we consider two species of particles only: neutrons and protons. The numerical scheme of solving the Vlasov equation is adapted from the lattice Hamiltonian method with test particles proposed by Lenk and Pandharipande [79]. The coordinate space is discretized into a cubic lattice with the lattice spacing $l = 1$ fm. Each test particle has a triangular-shaped form factor and contributes to the nearest eight lattice sites.

2.2.3 The dissipation and fluctuation dynamics

In heavy-ion collisions, nucleon-nucleon scattering acts like a dissipative force, driving the system towards thermal equilibrium. In accordance with the fluctuation-dissipation theorem, the dissipation of the beam energy heats up the system and is thus inevitably accompanied by thermal fluctuations. The thermal fluctuations may manifest themselves in terms of fluctuations in phase space density, which are expected to be linked with multifragmentation observed in intermediate-energy heavy-ion collisions. In this subsection, we aim to develop a framework that offers a consistent and simultaneous description of the dissipation and fluctuation dynamics.

The collision integral tied to two-body scattering reads

$$I_{coll} = \frac{g}{h^3} \int d^3 p_b \int d\Omega \frac{d\sigma_{ab}}{d\Omega} v_{ab} [(1 - f_a)(1 - f_b)f_{a'}f_{b'} - f_a f_b (1 - f_{a'})(1 - f_{b'})], \quad (2.5)$$

where the degeneracy factor is $g = 4$ for nucleons (when no distinction is made between neutrons and protons; see the discussion later), and v_{ab} is the relative velocity between nucleons a and b , and $d\sigma/d\Omega$ the nucleon-nucleon cross section. The indices a' and b' denote the final states of the colliding pair.

As the scattering energy increases, nucleon-nucleon scattering peaks more sharply forward. One can reduce the collision integral I_{coll} (2.5) into a Fokker-Planck form by making an expansion over the scattering angle θ (see Appendix A for more details) [80],

$$I_{coll} \rightarrow - \sum_i \frac{\partial}{\partial p_a^i} \left\{ f_a \cdot \frac{1}{2} [\tilde{R}_a^i + (1 - f_a) R_a^i] \right\} + \sum_{i,j} \frac{\partial^2}{\partial p_a^i \partial p_a^j} (f_a D_a^{ij}), \quad (2.6)$$

where

$$R_a^i = -\frac{g}{h^3} \int d^3 p_b f_b F_{ab} q_{ab}^i, \quad (2.7)$$

$$\tilde{R}_a^i = -\frac{g}{h^3} \int d^3 p_b f_b (1 - f_b) F_{ab} q_{ab}^i, \quad (2.8)$$

$$D_a^{ij} = \frac{g}{4h^3} \int d^3 p_b f_b (1 - f_b) F_{ab} (q_{ab}^2 \delta^{ij} - q_{ab}^i q_{ab}^j), \quad (2.9)$$

with $\mathbf{q}_{ab} = \mathbf{p}_a - \mathbf{p}_b$ and

$$F_{ab} = (\pi v_{ab}/2) \int_0^1 \theta^2 (d\sigma_{ab}/d\Omega) d\cos\theta. \quad (2.10)$$

The *beyond-mean-field* dynamics, depicted traditionally as two-body scattering processes, is transformed, by the Fokker-Planck Eq. (2.6), into diffusion processes of nucleons in the viscous nuclear system. The vector coefficients \mathbf{R} and $\tilde{\mathbf{R}}$, usually known as the drag coefficients, are connected to the viscosity of the system. The tensor coefficient \mathbf{D} is referred to as the diffusion tensor, which describes the anisotropic diffusion of particles.

Note that the cross section $d\sigma_{ab}/d\Omega$ enters the equation through the function F_{ab} , and hence has an effect on all coefficients in the equation. Admittedly, only the integrated effects of the cross section can be accounted for, so the overall magnitudes of the coefficients do not depend sensitively on the detailed angular dependence of the cross section. The anisotropic diffusion is predominantly governed by the anisotropy of the momentum distribution of particles in the medium, as can be seen in the definition of the diffusion tensor in Eq. (2.9). One, for sure, can carry out the expansion to higher orders. The resulted differential equation beyond second order, however, is not tractable with the aid of diffusion or Langevin dynamics. Furthermore, similar expansions such as the Kramers-Moyal expansion of the Boltzmann integral operator in terms of differential operators beyond the second order have known to be ill-behaved [81]. Therefore, we stick to the second-order Fokker-Planck equation and choose to put its validity to tests.

Consider an ensemble of systems with identical initial conditions. In the presence of fluctuations, the evolution of the ensemble will diverge. The Fokker-Planck equation provides a mathematical description of the distribution and ensemble-averaged behavior of these identically prepared systems. Indeed, the Fokker-Planck approach has been employed to study

the motion of an ensemble of Brownian particles, classical or quantal, in a medium at constant temperature, as the stationary solution of the Fokker-Planck equation yields the equilibrium distribution representing the correct statistics [82].

Inspired by the ideas of Brownian motion in a heat bath, we intend to encapsulate the beyond-mean-field dynamics altogether into the Brownian motion of nucleons in the typically non-equilibrium nuclear medium, through the Fokker-Planck Eq. (2.6). While the Fokker-Planck equation is deterministic, one may simulate the different dynamical trajectories of the system by use of the corresponding Langevin equation. The differential form of the nonlinear Langevin equation for nucleons undergoing Brownian motion reads,

$$d\mathbf{p}_a = \frac{1}{2} [\tilde{\mathbf{R}} + (1 - f_a) \mathbf{R}] dt + \boldsymbol{\sigma} d\mathbf{B}_t, \quad (2.11)$$

where \mathbf{R} and $\tilde{\mathbf{R}}$ carry the same definitions and meanings as in equations (6) and (7), $\boldsymbol{\sigma}$ is a 3×3 positive definite matrix such that

$$D^{ij} = \frac{1}{2} \sum_k \sigma_{ik} \sigma_{jk}. \quad (2.12)$$

\mathbf{B}_t denotes a Gaussian random process with properties

$$\langle d\mathbf{B}_t \rangle = \mathbf{0}, \quad (2.13)$$

$$\langle dB_t^i dB_t^j \rangle = dt \delta_{ij}. \quad (2.14)$$

This equation describes the momentum transfer, or the “kick”, experienced by a nucleon due to its interaction with the medium within a time interval Δt . The first term is dissipative and connected to the viscosity of the nuclear medium, while the second term is stochastic and gives rise to the fluctuations in the dynamics. In the limit of thermodynamical

equilibrium, coefficients in the Langevin equation are related by the equilibrium temperature, in a manner akin to the classical Einstein relation, as is shown in Appendix B.

For the time being, we do not distinguish between nn , pp , and np scatterings by employing a spin-isospin averaged nucleon-nucleon cross section. We further restrict our attention to elastic scatterings by targeting collisions at energies near or below pion production threshold. Extensions to incorporate elastic and inelastic collisions between different species can be made in the future at little cost by adjusting the degeneracy factor g and adopting the suitable differential cross sections $d\sigma_{ab}/d\Omega$. More care needs to be taken for the change of species though in the case of inelastic scatterings.

The Langevin equation meets our goal of treating the dissipation and fluctuations in the dynamics both consistently and simultaneously. We evolve the system by application of the Langevin equation to every nucleon in the system in addition to the mean-field dynamics. Details of the numerical implementations will be discussed in a subsequent subsection.

2.2.4 Initialization with the Thomas-Fermi equations

For nucleons inside a stable nucleus, two-body scatterings are strongly suppressed by the Pauli blocking. Hence, for any given mean-field potential, the initial configuration of nucleons in phase space, ideally, should coincide with the stationary solution to the Vlasov equation. This solution

amounts to that to the coupled Thomas-Fermi equations [79],

$$U_n(\rho(r), \delta(r)) + \frac{\hbar^2}{2m_n} k_F^2(\rho_n(r)) = \mu_n, \quad (2.15)$$

$$U_p(\rho(r), \delta(r)) + U_{\text{Coul}} + \frac{\hbar^2}{2m_p} k_F^2(\rho_p(r)) = \mu_p, \quad (2.16)$$

where $U_X(\rho, \delta)$ is the self-consistent mean-field potential as in Eq. (2.3), μ_X is known as the chemical potential and k_F is the Fermi momentum. The subscript X denotes the particle species.

Owning to the surface term in the mean field, the Thomas-Fermi equations are second-order ordinary differential equations. They are to be solved with the boundary conditions $\rho_{n/p}(r \rightarrow \infty) = 0$ and $(d\rho_{n/p}/dr)|_{r=0} = 0$. One may solve them numerically by employing Ansatzes for $\rho_{n/p}(r)$ and adjusting $\mu_{n/p}$ iteratively [66].

In this work, we propose a different method to solve the coupled Thomas-Fermi equations. We rewrite the equations by multiplying both sides by density ρ_X ,

$$h_X(\rho_n(r), \rho_p(r)) \rho_X(r) = \mu_X \rho_X(r) \quad (2.17)$$

with the single-particle hamiltonian $h_X = U_X + \hbar^2 k_F^2 / 2m_X + U_{\text{Coul}} \delta_{X,p}$. Eq. (2.17) has the same structure as the Hartree-Fock equation, prompting us to tackle it as an eigenvalue problem. Using a discretized position basis, we can obtain a matrix representation for h_X and a vector representation for ρ_X ,

$$h_{ij}^{(X)} = \langle r_i | \hat{h}_X | r_j \rangle = h_X(\rho_{n/p}(r_i), \rho_{n/p}(r_j)), \quad (2.18)$$

$$\rho_i^{(X)} = \langle r_i | \rho_X \rangle = \rho_X(r_i). \quad (2.19)$$

Note that h_X is not diagonal, because the derivatives involved are computed in terms of finite differences in the basis. In Eq. (2.17), ρ_X plays

the role of the eigenvector of h_X and μ_X the eigenvalue. We use a self-consistent iterative method [83] to find eigenvectors and eigenvalues for h_n and h_p . The pair of eigenvectors $\{\rho_n, \rho_p\}$ in the position basis corresponding to the smallest eigenvalues, i.e., lowest chemical potentials $\{\mu_n, \mu_p\}$, is chosen to generate the fields $h_{n/p}(\rho_n, \rho_p)$ in the next iteration and picked as the actual density profiles in the end.

We demonstrate this method by computing the density profiles for a medium-sized nucleus ^{58}Ni and a large-sized nucleus ^{197}Au using the mean-field potential with a $K = 240$ MeV mentioned above. The computed radial density profiles are shown in Fig. 2.1. We note that density profiles with the Thomas-Fermi approximation lacks the ripples associated with shell effects in typical Hartree-Fock calculations. The tails of the density profiles exhibit rapid fall-offs, which is also typical of Thomas-Fermi calculations [83]. In practice, the unphysical fall-off of the tails get mitigated by numerical sampling of test particles and coarse graining, as is seen in the initial distributions at $t = 0$ fm/c in Fig. 2.2.

2.2.5 Brownian motions of nucleon wave-packets

In this model, the beyond-mean-field residual-interactions, between individual nucleons and the nuclear medium they are locally immersed in, are presumed to be dissipative and random, and governed by the proposed Langevin Eq. (2.11). We refer to these momentum and energy exchanges between particles and medium as *Brownian motions*. In what follows, we will describe at length the perspective on these Brownian motions and their numerical implementation. Given the mesoscopic nature of nuclear systems, physics and practical details are entangled.

Partition of test particles into nucleon wave-packets

While ensuring a sufficiently smooth coverage of the phase space in the simulation of mean-field dynamics, the large quantity of test particles used, typically $N_{test} = 10^2 - 10^3$ test particles per nucleon, have adverse effects on the fluctuation dynamics. The scatterings of test particles supposedly representing the same nucleon are uncorrelated, which would inevitably wash out most of the fluctuations in the dynamics. This, to a large extent, explains why BUU-type approaches typically have vanishingly small fluctuations compared with QMD-type approaches, whose degrees of freedom are nucleons. Different attempts have been made over the years to restore the nucleonic degrees of freedom in two-body scatterings in the BUU framework [24, 35]. The main idea of them is to agglomerate test particles adjacent in phase space into so-called nucleon wave-packets and to move them collectively as a whole.

We adopt a similar approach to enhance the effects of fluctuations. In each time step, we partition the test particles into nucleon wave-packets and execute Brownian motion with these nucleon wave-packets as the degrees of freedom. The pre-partition is accomplished through the k-means clustering algorithm [84] with a metric in phase space parametrized in the following form,

$$d^2 = \frac{(\mathbf{r}_i - \mathbf{r}_j)^2}{d_r^2} + \frac{(\mathbf{p}_i - \mathbf{p}_j)^2}{d_p^2} \quad (2.20)$$

where subscripts i and j denote two points in phase space. The parameters d_r and d_p address the compactness in the coordinate and the momentum spaces respectively. We run the k-means clustering algorithm to partition both the neutron test particles and the proton ones separately. The algorithm is set to terminate after several iterations, and the values $d_r = 1.2$

fm and $d_p = 130.5$ MeV/c are used. It is found in practice that the final results are not sensitive to either the early termination of the clustering algorithm or the values of the metric parameters.

After the pre-partition, the system is divided into N neutron subspaces and Z proton subspaces. The pre-partition is simple but somewhat arbitrary, and thus only the centroids are to be used. We identify these centroids as the *scattering centers* for the nucleons.

For each centroid $(\mathbf{r}_i, \mathbf{p}_i)$ for which the local nucleon density is above 0.1 fm^{-3} , we consider a spherical region centered at \mathbf{r}_i of radius $R \sim 2$ fm. This value corresponds roughly to the sum $\sqrt{\sigma_{NN}/\pi} + \sqrt{\langle r_{ch}^2 \rangle}$, where the nucleon-nucleon cross section $\sigma_{NN} \simeq 40$ mb and the root-mean-square proton charge radius $\sqrt{\langle r_{ch}^2 \rangle} \simeq 0.86$ fm. R can also be made density-dependent, with the empirical choice of $R(\rho) = [1.99 - 0.18\rho^{-\frac{4}{3}}(\rho - \rho_0)]\text{fm}$. The latter empirical formula is what actually used in the code. Inside the spherical region, we search for test particles close to the centroid $(\mathbf{r}_i, \mathbf{p}_i)$ using the following phase-space metric:

$$d^2 = \frac{(\mathbf{r}_i - \mathbf{r}')^2}{\sigma_r^2} + \frac{(\mathbf{p}_i - \mathbf{p}')^2}{\sigma_p^2} \quad (2.21)$$

with $\sigma_r = R$ and $\sigma_p = \hbar/2R$. This metric emphasizes the compactness in momentum space, while connected to the Heisenberg uncertainty principle. The Langevin Eq. (2.11) is originally intended for point-like particles, and hence wave-packets well-localized in momentum space are preferred. The N_{test} test particles of the same species closest to the centroid form the wave-packet to undergo Brownian motion. The rest of the particles constitute the medium, with which the wave-packet interacts.

Evaluations of the Langevin equation's coefficients on a lattice

The coefficients \mathbf{R} , $\tilde{\mathbf{R}}$ and \mathbf{D} involve integrals folded over the momentum space, which require the knowledge of occupation at different momenta. To this end, we construct a three-dimensional cubic lattice over the entire momentum space inside each spherical scattering region and we evaluate the occupation at different sites.

The lattice spacing L_p needs to be chosen with care to faithfully reflect the actual spread and spacing of the underlying test particles. We use the standard deviation σ_p^{wp} of the momentum of test particles belonging to the nucleon wave-packet as a measure to constrain lattice spacing. We normally choose the spacing $L_p = \max\{1.2\sigma_p^{wp}, \hbar/(2R)\}$, where R is the radius of the spherical scattering region under consideration. With such constraints, the values of the spacing L_p typically fall between 100 MeV/c and 140 MeV/c, which ensures a sensible coarse graining in the momentum space.

Occupation $f(\mathbf{p})$ at each momentum lattice site is evaluated in the same fashion as spatial densities are on a spatial lattice in mean-field dynamics simulations. Test particles have a triangular-shaped form factor, contributing to the eight nearest lattice sites only. Integrals of \mathbf{R} , $\tilde{\mathbf{R}}$ and \mathbf{D} are computed as summations over all sites of the three-dimensional momentum lattice.

Momentum transfer from the nuclear medium to the nucleon wave-packet

With a reasonable time step size $\Delta t \sim 0.25 - 0.5$ fm/c, the first term of the Langevin Eq. (2.11) can be readily calculated. The stochastic term involves a matrix $\boldsymbol{\sigma}$, which needs to be extracted as the square root of

the diffusion matrix \mathbf{D} . Note that, by the definition in equation (8), \mathbf{D} is a real symmetric positive semi-definite matrix. It follows that \mathbf{D} can be diagonalized as $\mathbf{D} = \mathbf{O}\Lambda\mathbf{O}^\top$, where Λ is a diagonal matrix and \mathbf{O} an orthogonal matrix. We then represent $\boldsymbol{\sigma}$, cf. Eq. (A.12), as

$$\boldsymbol{\sigma} = \mathbf{O}\Lambda^{\frac{1}{2}}\mathbf{O}^\top, \quad (2.22)$$

where $\Lambda^{\frac{1}{2}}$ is diagonal whose diagonal elements are the unique square roots of the corresponding diagonal elements in Λ . It can be easily verified that $\boldsymbol{\sigma}$ constructed according to (2.22) satisfies (8).

With a time step of size Δt , the differential notation $d\mathbf{B}_t$ is interpreted as a 3-dimensional random vector, whose components are independent Gaussian random numbers. The underlying Gaussian distribution has a mean equal to zero and a variance equal to Δt .

In summary, the momentum transfer $\Delta\mathbf{p}$ within a time step Δt in a spherical scattering region is simulated as

$$\Delta\mathbf{p}_a = \frac{1}{2}[\tilde{\mathbf{R}} + (1 - f_a)\mathbf{R}]\Delta t + \boldsymbol{\sigma} \mathbf{g}(0, \Delta t) \quad (2.23)$$

with $\mathbf{g}(0, \Delta t)$ being a random vector comprised of 3 independent Gaussian random numbers sampled with mean = 0 and variance = Δt .

Recoil for conservation of momentum and energy

After a nucleon wave-packet is shifted in the nuclear medium inside a spherical scattering region, the recoil of the nuclear medium needs to be accounted for in order to preserve the conservation of total momentum and total energy. The interaction between the nucleon wave-packet and the nuclear medium is reciprocal. Indeed, by exchanging the subscripts a and b in the Langevin Eq. (2.11), one obtains an expression for how the

nucleon wave-packet induces recoil of particles in the medium. Thus, the recoil can be treated in principle precisely.

On the other hand, owing to the facts that the number of particles involved in the medium is large and that the recoils are coupled in a non-trivial manner, we instead adopt a collective and approximate treatment of the recoil effects: the center of momentum of the nuclear medium is shifted to conserve total momentum, and all particles in the medium are scaled with respect to the new center of momentum to conserve total energy.

Additionally, it is worth noting that the nuclear medium almost always contains more than one nucleon. The collective shift-and-scale adjustment, in effect, introduces many-body correlations in the nuclear medium.

Pauli-blocking procedure

Within the scattering region, after the kick of the nucleon wave-packet and the adjustment for recoil in the nuclear medium, we compute again the occupation over the entire lattice in momentum space. The Brownian motion is finalized only if none of the occupation at any lattice site exceeds 1. Otherwise, we deem the Brownian motion unphysical and revert all changes. This Pauli blocking procedure proves to be effective. For single ground state nuclei, over 97% of the attempted Brownian motions are *blocked* in the current model prescription, and stability of the nuclei are demonstrated in Fig. 2.2.

Fig. 2.2 shows the time evolution of the radial density profiles for a single ^{58}Ni and a single ^{197}Au up to 200 fm/c in steps of 40 fm/c, simulated by the our Brownian code under the same controlled conditions specified in Ref. [3]. Ideally, the density distribution should remain unchanged over

time for single nuclei. In our case, the density profiles show only small scale fluctuations over the entire course of simulation. It indicates, in particular, that numerical solutions of the Thomas-Fermi Eq. (2.15) approximate the true solutions of the Vlasov Eq. (2.2) reasonably well. Further, majority of the spurious large momentum transfers are effectively blocked by the Pauli-blocking procedure.

Summary of implementation of Brownian motions

In each time step, the occupied phase space is partitioned into $N + Z$ subspaces of roughly equal volume. Scattering regions are constructed spherically around the spatial centroids of each subspace. These regions are to be examined successively in a random order. Within each scattering region, a separation of the nucleon wave-packet from the nuclear medium is made. The Langevin equation is evaluated on a 3-dimensional lattice in momentum space, and the resulted momentum transfer is applied to the nucleon wave-packet. In observance of the conservation laws, the recoil effects are taken into account through an adjustment of the momentum distribution of particles in the medium. A Pauli-blocking procedure is applied in the end to preserve the Pauli exclusion principle.

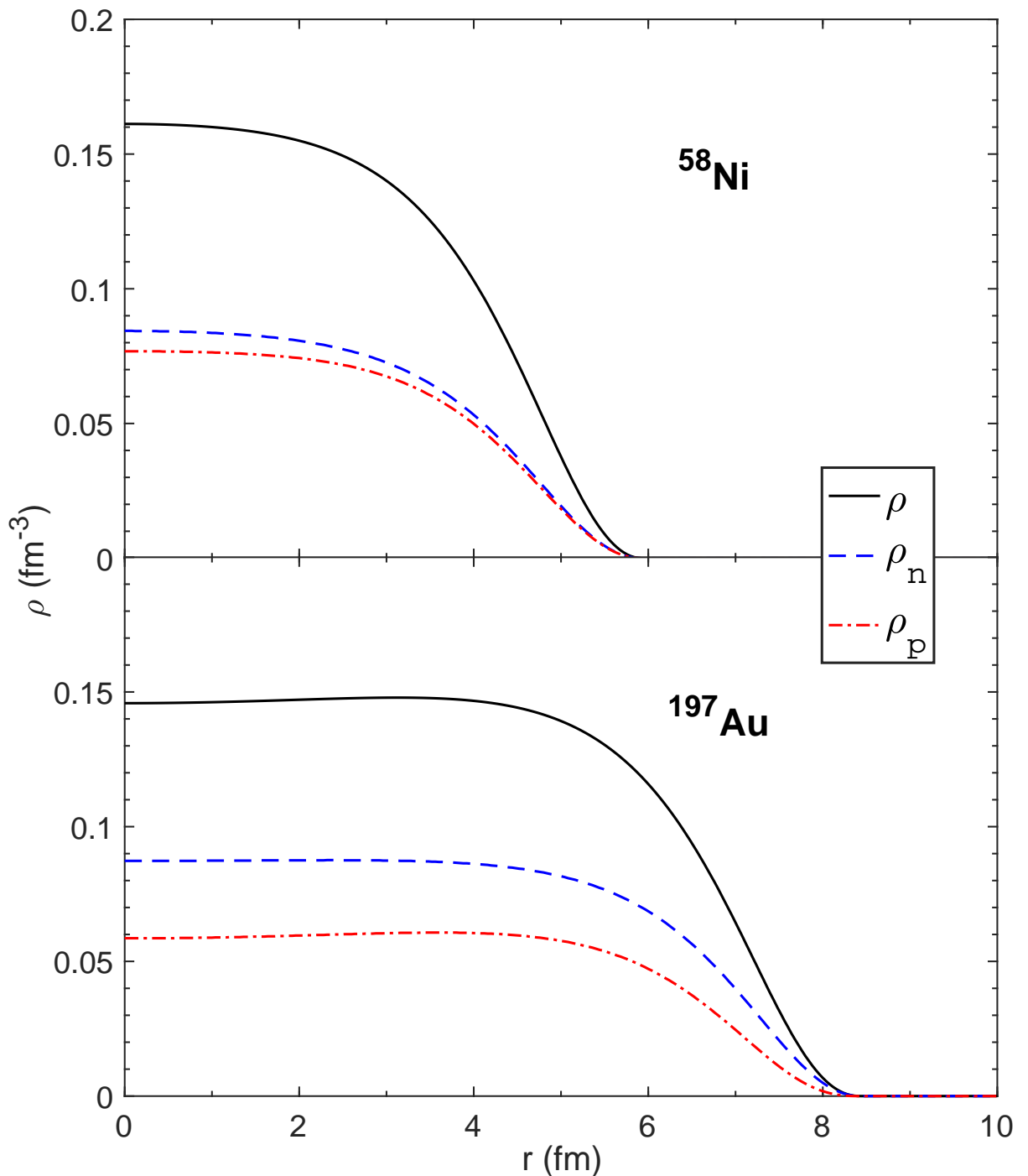


Figure 2.1: (Color online) Density profiles of stable nuclei ^{58}Ni and ^{197}Au obtained from solutions of the Thomas-Fermi equations.

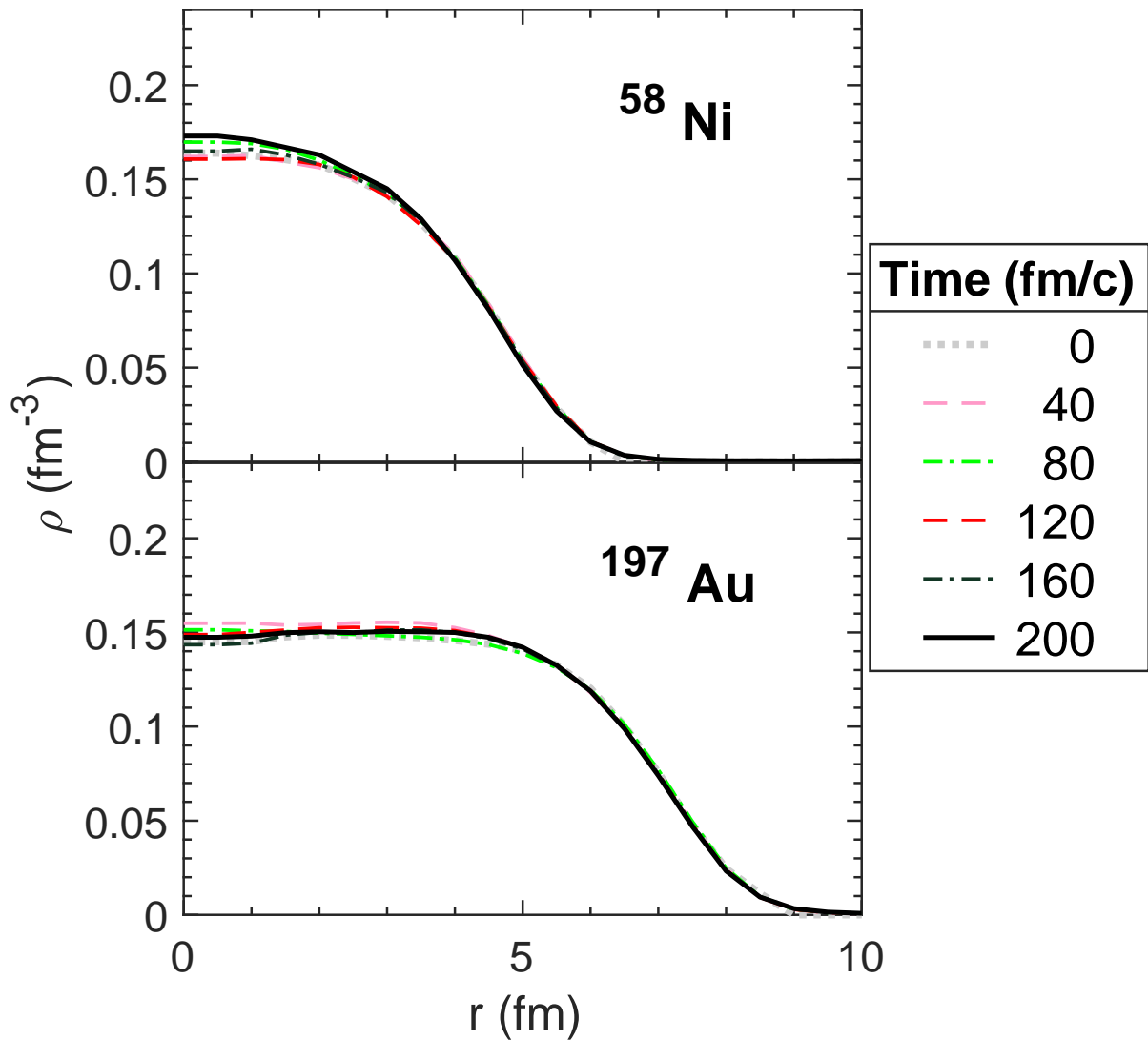


Figure 2.2: (Color online) Time evolution of radial density profiles for single nuclei ^{58}Ni and ^{197}Au in steps of 40 fm/c.

Chapter 3

Applications to heavy-ion collisions at intermediate energies

3.1 Benchmarks

In this section, we first demonstrate practical applicability of our model to heavy-ion collisions by simulating the Au-Au collisions at both 100 MeV/nucleon and 400 MeV/nucleon, at an impact parameter of $b = 7$ fm. We study the nucleon rapidity distribution and the average in-plane flow $\langle p_x/A \rangle$ and compare our simulation results with those from other transport codes in the code comparison project of Ref. [3]. After confirming that our model can yield reasonable results for one-body observables, we proceed to investigate its ability to describe multi-fragmentation processes. To this end, we study the time evolution of the systems: $^{112}\text{Sn} + ^{112}\text{Sn}$ and $^{124}\text{Sn} + ^{124}\text{Sn}$ at 50 MeV/nucleon at an impact parameter $b = 0.5$ fm. A preliminary comparison of results with the Stochastic Mean Field (SMF) and the Antisymmetrized Molecular Dynamics (AMD) models from Ref. [4] is also made.

3.1.1 One-body observables for Au + Au system

Fluctuations associated with Brownian motions enable our model to probe a broader range of intermediate and final channels. It is of interest to study whether the diversity of intermediate and final channels may affect the description of one-body observables. Our model is applied to simulate the Au + Au reactions at two incident energies, 100 MeV/nucleon and 400 MeV/nucleon. These specific reactions were also studied and compared in a transport code comparison project under controlled conditions [3]. The same impact parameter $b = 7$ fm as there is chosen. Identical mean-field interactions and nucleon-nucleon cross sections as there are employed.

Rapidity distribution

The rapidity distribution in the final state gives a Lorentz invariant measure of the degree of stopping of nucleons attained in heavy-ion collisions [3]. The more particles populate the mid-rapidity region in the center of mass frame, the stronger the stopping effects are.

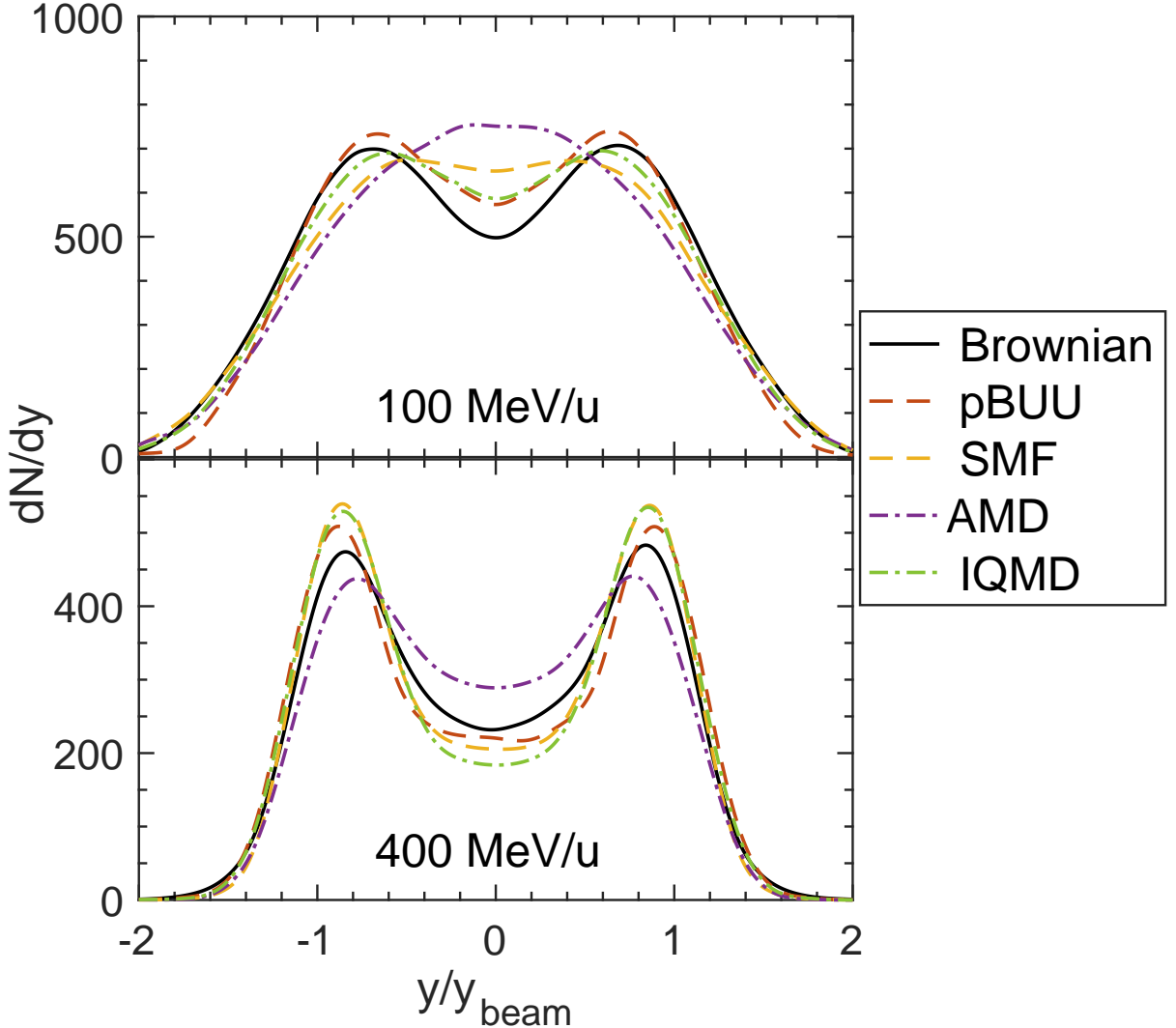


Figure 3.1: (Color online) Final rapidity distributions as a function of reduced rapidity for $^{197}\text{Au} + ^{197}\text{Au}$ at beam energies of 100 MeV/nucleon (upper panel) and 400 MeV/nucleon (lower panel) at an impact parameter $b = 7$ fm. Solid curves, dashed curves and the dashed-dot curve correspond to the Brownian model, BUU-type models, and QMD-type models [3], respectively.

In Fig. 3.1, we display the final rapidity distributions from our calculations accompanied by results of selected BUU and QMD calculations from Ref. [3]. At low incident energy 100 MeV/nucleon, there is a large amount of filling of the mid-rapidity region, indicating a relatively strong stopping. While all codes except for AMD exhibit a shallow double-humped struc-

ture, differences in details of the rapidity distributions are not negligible. This is probably tied to differences in treating Pauli principles in different codes and to delicate competition of mean-field interaction and many-body correlations at this incident energy [3]. At higher incident energy of 400 MeV/nucleon, fewer particles populate the mid-rapidity region compared to the outer regions and the double-peaked feature is more pronounced, due to a weaker stopping and shrinking Fermi momentum compared to incident momentum per nucleon. General consistency is found among most calculations, although nonrelativistic models such as the Brownian motion model and AMD predict mildly stronger stopping.

Average in-plane flow $\langle p_x/A \rangle$

Use of a finite impact parameter, $b = 7$ fm, in this study, breaks the macroscopic rotational symmetry around the beam axis in the system, and therefore anisotropy appears in the transverse collective momentum distribution. We focus on the average in-plane flow $\langle p_x/A \rangle$, simply known as the transverse flow, as a function of the reduced rapidity y/y_{beam} in the center of mass frame. When quantified, the transverse flow is commonly described in terms of an “S-shaped” curve. The slope at the origin, commonly known as the “slope parameter”, is of importance. Particles in the mid-rapidity region are expected to come from the compressed region during the collision, and thus the study of this flow parameter can shed light on the behavior of the nuclear equation of state beyond normal density.

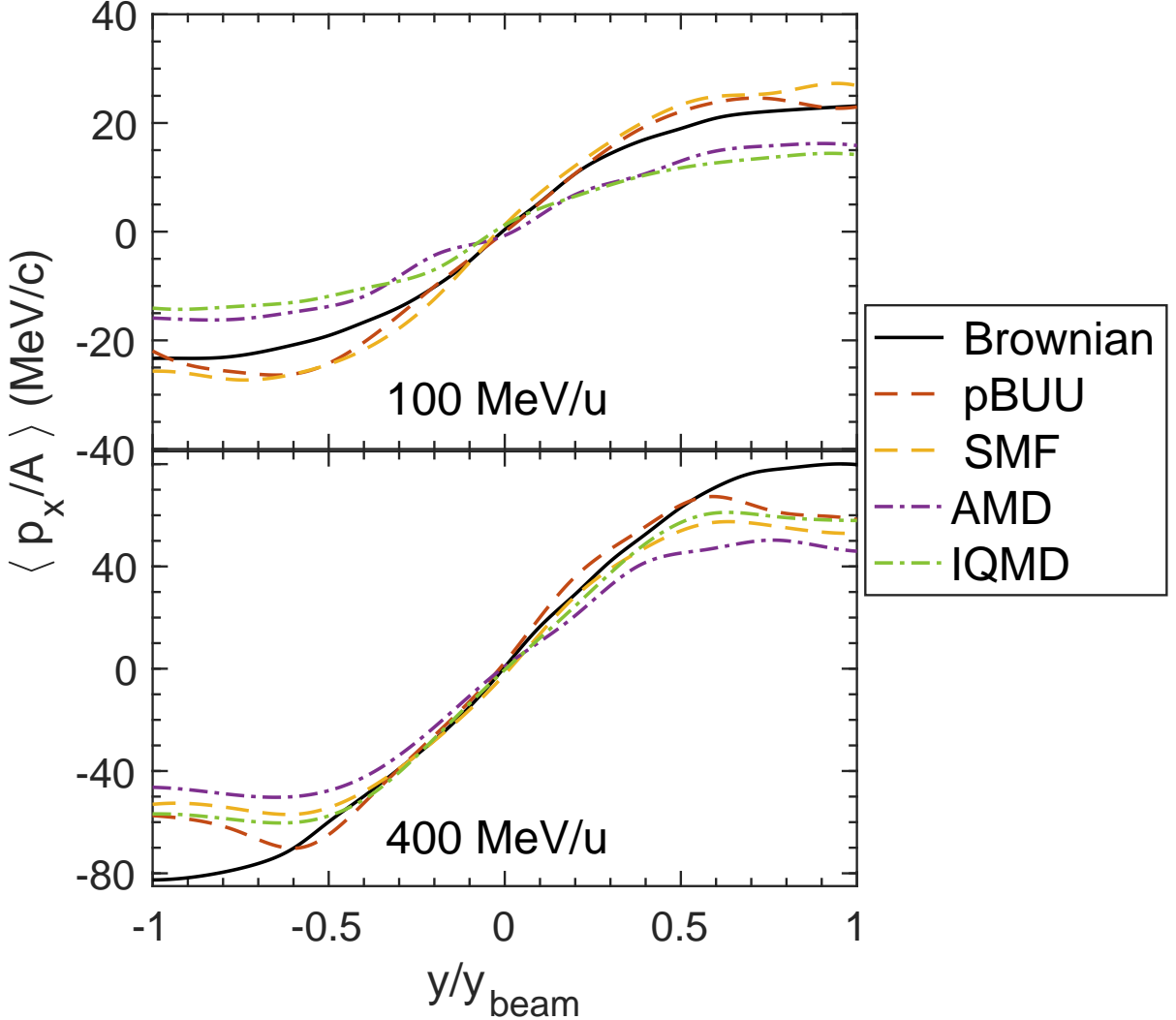


Figure 3.2: (Color online) Final average in-plane flow as a function of reduced rapidity for $^{197}\text{Au} + ^{197}\text{Au}$ collisions at beam energies of 100 MeV/nucleon (upper panel) and 400 MeV/nucleon (lower panel) and an impact parameter $b = 7$ fm. Solid curves, dashed curves and the dashed-dot curve represent the Brownian model, BUU-type models, and QMD-type models [3], respectively.

In Fig. 3.2 we show the average in-plane flow for our calculations together with results from selected transport models from Ref. [3]. In all calculations, the expected S-shaped curves are produced at both energies. The positive slopes at the origin indicate that the effects of nucleon-nucleon scattering dominate over those of the mean field. At 100 MeV/nucleon,

the BUU-type models clearly produce greater inflections than the QMD-type models. The prediction from the Brownian motion model lies between them. At 400 MeV/nucleon, it appears that all five transport models yield very consistent results in the mid-rapidity region.

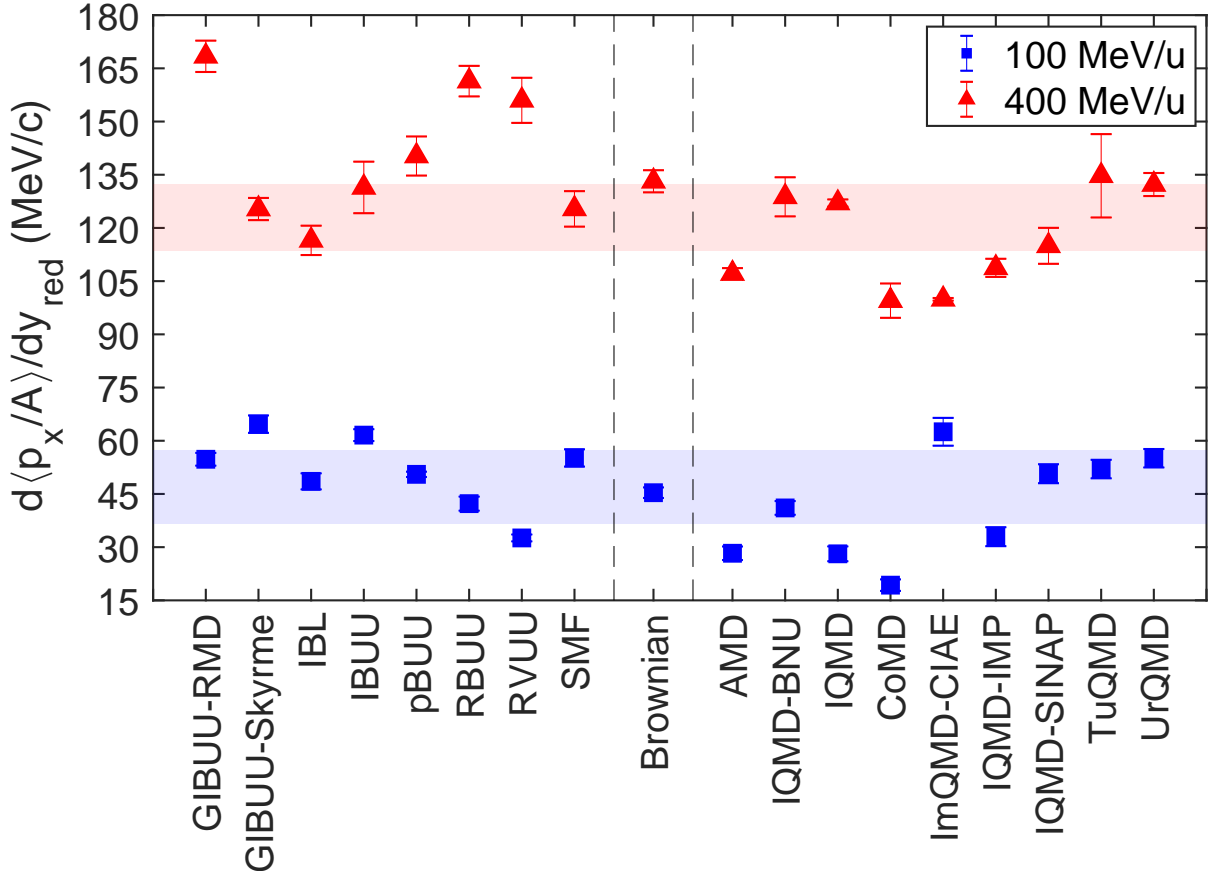


Figure 3.3: (Color online) Flow slope parameter for different transport models [3] for $^{197}\text{Au} + ^{197}\text{Au}$ collisions at beam energies of 100 MeV/nucleon (blue squares) and 400 MeV/nucleon (red triangles) at an impact parameter $b = 7$ fm. The error bars represent the fitting uncertainties. These become invisible when they are smaller than the symbols. The colored bands correspond to roughly 52% confidence intervals from the statistics of calculations from both the BUU-type and the QMD-type models. (See text for a more detailed explanation.)

The slope parameters at mid-rapidity can be extracted through a linear fit in a small interval centered at the origin. The values of the slope param-

eters at two energies for different transport simulations [3] are summarized in Fig. 3.3. The error bars take into account the fitting uncertainties only. On top of the simulation results, we also added shaded bands to indicate regions in which calculations are considered to be *statistically* consistent with majority of the BUU-type and QMD-type models. To obtain the statistically consistent regions, we first computed the $\sqrt{2}\sigma$ -intervals centered at the mean values for the BUU sample and the QMD sample independently. σ stands for the standard deviation of the sample. The statistically consistent regions were taken to be the overlap of the $\sqrt{2}\sigma$ -intervals from the two samples. If we further assume that the BUU sample and the QMD sample follow an identical Gaussian distribution, the consistent regions can also be interpreted as roughly 52% confidence intervals. Note that throughout the statistical analysis, results from the Brownian motion model were deliberately excluded to avoid any possible bias. Nevertheless, the slope parameters extracted from the Brownian simulations are found to be statistically consistent with majority of the other calculations.

The reassuring consistency of results between the Brownian motion model and other current transport models provides evidence that the one-body Brownian motion picture can successfully capture the effects of two-body scattering and mean field in heavy-ion collisions.

Last but not least, in analyzing results from the Brownian motion model, we averaged the rapidity and the in-plane flow over 32 independent events, and the averaged results exhibit good parities as functions of the reduced rapidity. It needs to be pointed out that the fluctuation dynamics described by the Langevin Eq. (2.11) does not automatically preserve forward-backward reflection symmetry, and that parity symmetry breaking

or other types of symmetry breaking can be observed in individual events. Since the “directions” of the symmetry breakings are essentially random, symmetry can be restored by ensemble-averaging over independent runs. In fact, these symmetry breakings, resulted from the broadening of dynamical trajectories, can be crucial for the formation of fragments to be discussed in the next subsection. For instance, an uneven break-up of two nuclei in symmetric central collisions will be likely associated with an asymmetry in the rapidity distribution.

3.1.2 Fragmentation dynamics with Sn + Sn at 50 MeV/nucleon

In this subsection, we will demonstrate how the ability of our model to probe a plethora of intermediate and final states is connected with the formation of intermediate mass fragments (IMF) in central heavy-ion collisions. The systems we study are $^{112}\text{Sn} + ^{112}\text{Sn}$ and $^{124}\text{Sn} + ^{124}\text{Sn}$ at 50 MeV/nucleon at an impact parameter $b = 0.5$ fm. These systems have already been studied by Colonna *et al.* using both SMF and AMD [4]. We will make a preliminary comparison between our simulation and those in SMF and AMD. A density-dependent and energy-dependent nucleon-nucleon cross section is used,

$$\sigma_{NN}(E_{\text{lab}}, \rho) = \sigma_{NN}^{\text{free}}(E_{\text{lab}}) \exp \left[-\alpha \frac{\rho/\rho_0}{1 + E_{\text{lab}}/E_0} \right] \quad (3.1)$$

with $\alpha = 0.3$, $\rho_0 = 0.16 \text{ fm}^{-3}$, $E_0 = 150 \text{ MeV}$ and a maximum cuff-off at 150 mb. $\sigma_{NN}^{\text{free}}(E_{\text{lab}})$ is taken as the cross section parametrization by Li and Machleidt at zero density [85]. The evolution of the systems is followed up to 280 fm/c after initial contact.

Fig. 3.5 shows the density contour plots from projecting nucleons on the reaction plane for the $^{112}\text{Sn} + ^{112}\text{Sn}$ system at different stages of the re-

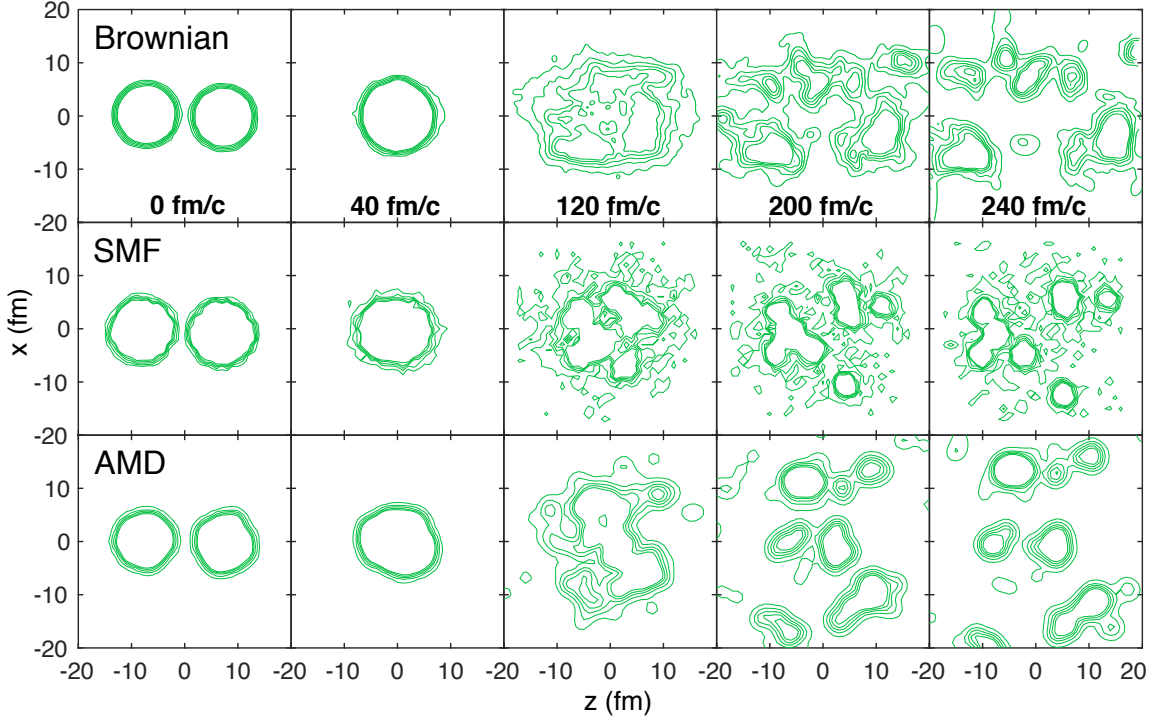


Figure 3.5: (Color online) Density contours for nucleons projected onto the reaction plane in the reaction $^{112}\text{Sn} + ^{112}\text{Sn}$ at 50 MeV/nucleon at an impact parameter of $b = 0.5$ fm, at different times during the reaction. Results calculated with the Brownian motion model are displayed in the first row of the panels. The bottom two rows show results from SMF and AMD calculations [4]. The densities for the projected contours start at 0.07 fm^{-2} and consecutively increase by 0.1 fm^{-2} .

action calculated with different transport models. All three models give a qualitatively consistent description of the compression-expansion dynamics, and cluster structures are formed in the expansion phase. During the approach and compression up to 40 fm/c, calculations from the three models with fluctuations and many-body correlation effects do not appear to be distinguishable from what would be expected from conventional transport models without fluctuations. The suppression in the role of fluctuations is linked to the limited volume of phase space available for the system to populate, since it is far from thermalized in the early stage. At 120 fm/c, we can already observe, in all simulations, that the expanding systems

turn inhomogeneous. These inhomogeneities, which would not have existed without fluctuations, provide seeds for fragmentation, and there are cluster structures forming in the core. As the system continues to expand, the lumps of matter move away from one another and escape from the central region. For all three models, sizable fragments can be identified after 200 fm/c, and changes between 200 fm/c and 240 fm/c are sporadic and moderate. As a result, we assume that the configurations have frozen out by 240 fm/c, and we terminate the simulations at 280 fm/c.

The three models differ quite substantially in details of the predictions for the expansion phase. In the Brownian motion model calculations, the degree of stopping is comparatively low and the system tends to expand more along the beam direction. On the other hand, in AMD, the system expands quickly with a focus around the x -direction, which indicates a very strong stopping that is also seen in the Au-Au simulations. The relatively isotropic and slow expansion in SMF can probably be explained by the spinodal decomposition of a nearly homogeneous source at low density [86]. We also count the number of nucleons in the “gas” phase ($\rho < \frac{1}{6}\rho_0$) predicted by our model and compare the number to results of SMF and AMD [87]. It is found that our model yields more gas-phase nucleons than AMD, but only slightly fewer than SMF.

Regarding the fragmentation mechanism in our model, in-medium Brownian motions introduce branching points in the dynamical trajectories and allow for “jumps” among a greater range of intermediate and final configurations. These jumps, stemming from nucleon-nucleon scatterings, are abrupt and discontinuous in time. The Langevin Eq. (2.11), with its stochastic term introducing discontinuities in time, serves the purpose. By

solving the Langevin equations, we attempt to simulate the abrupt jumps from one n-body configuration to another. As the deviations from the ensemble-averaged trajectory predicted by the Boltzmann Eq. (2.1) accrue from the jumps, exotic configurations including those with fragmentation eventually become accessible. In the quantum-mechanical picture, configurations are represented by superpositions of Slater determinants. While mean-field evolution is coherent in principle, the residual incoherent many-body correlations, such as two-body scattering, result in decoherence and transitions between different Slater determinants. Among the stochastic approximations of the quantum many-body problems are the AMD model [37, 38, 88] and the Stochastic Time-Dependent Hartree-Fock (STDHF) theory [32]. In treating the jumps between different configurations as a stochastic process, the Brownian motion model is conceptually consistent with these quantal approaches.

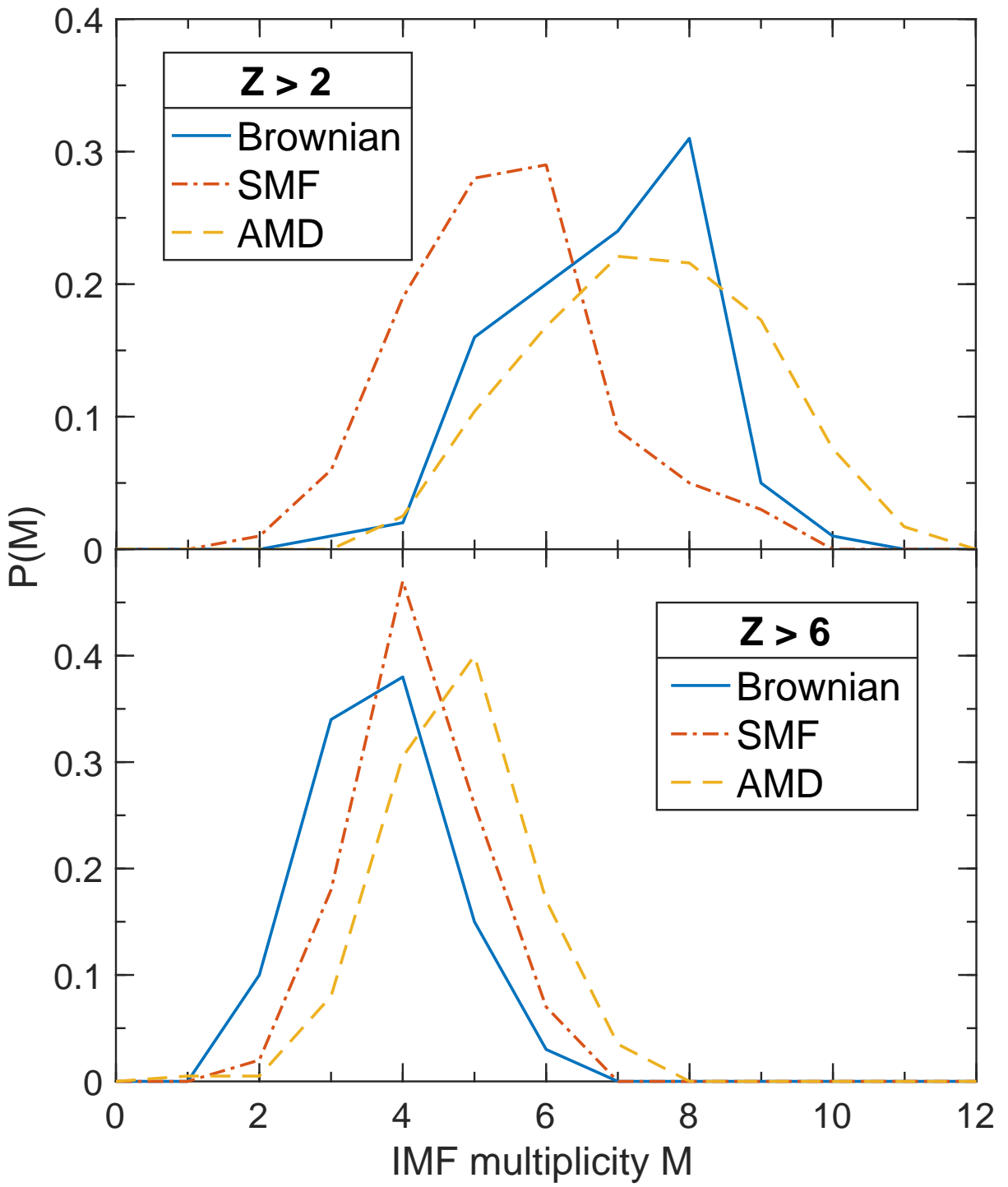


Figure 3.6: (Color online) Distribution of IMF multiplicity obtained from different models for the reaction $^{124}\text{Sn} + ^{124}\text{Sn}$ at 50 MeV/nucleon at an impact parameter $b = 0.5$ fm. The upper panel shows the multiplicity distribution of IMFs with charge $Z > 2$ and the lower panel with $Z > 6$ [4].

A comparison of the IMF multiplicity between the Brownian motion

and the other two transport models for $^{124}\text{Sn} + ^{124}\text{Sn}$ is shown in Fig. 3.6. In our case, fragments are identified with a simple coalescence algorithm with a cut-off density $\rho_c = 0.02 \text{ fm}^{-3}$ [35]. The distribution is obtained from 100 independent simulations.

For IMFs with charge $Z > 2$, our multiplicity distribution looks compatible with that from AMD. Both distributions maximize around multiplicity = 7 or 8 and share a similar spread. For larger IMFs with charge $Z > 6$, our calculations yield a slightly lower multiplicity, while still predicting essentially the same spread as the others. Since our model, as well as SMF, predicts more free nucleon emission than AMD, fewer nucleons are available in the “liquid” phase ($\rho > \frac{1}{6}\rho_0$) for the assembly of IMFs. Moreover, due to the large number of free nucleons and light fragments in our simulations, the effective surface-to-volume ratio is also higher, which might lead to spurious evaporation of test particles and hinder the formation of fragments. Nonetheless, the Brownian motion model breaks through the limitations of traditional Boltzmann transport framework and proves to have great potential for the description of multifragmentation.

3.1.3 Summary and discussion

In the last two sections, we have reformulated the beyond-mean-field dynamics in heavy-ion collisions in terms of Brownian motions of nucleons in the viscous, out-of-equilibrium nuclear medium, as opposed to the typical two-body scatterings. The Brownian motions represent, in effect, the momentum and energy exchange between a nucleon and the nuclear medium it is immersed in. They are governed by a set of Langevin equations consisting of a friction-like term and a stochastic term. This approach describes

the dissipation and fluctuation dynamics consistently and simultaneously. Furthermore, each simulation generates a unique dynamical trajectory, enabling us to probe different exit channels and obtain the distribution of possible outcomes of the ensemble.

The details of the numerical simulations, including a new method to initialize stable nuclei from the Thomas-Fermi approximation, have been presented. We have applied our model to the time evolution of isolated stable nuclei. The stabilities of the simulations and the nuclei are well established.

To demonstrate that our model's ability to describe one-body observables is on par with that of other transport models, we have studied the final rapidity distribution and average in-plane flow in the reaction $^{197}\text{Au} + ^{197}\text{Au}$ at two incident energies and showed that our results are comparable with those obtained from either QMD-type models or BUU-type models [3].

We have also investigated formation of fragments in heavy-ion collisions with our model and confirmed the crucial role fluctuations play in seeding multifragmentation. We have repeated the calculations of Sn + Sn at $E = 50 \text{ MeV/nucleon}$, previously done with the SMF and the AMD models [4]. As seen from the time evolution of density contours for nucleons projected on the reaction plane, and all three models depict a fragmented system with similar general features. Regarding the distribution of IMF multiplicity, We find that the yield of light IMFs with $Z > 2$ in the Brownian motion model is comparable to that in AMD, but our yield of large IMFs with $Z > 6$ is slightly lower than that in SMF or AMD.

So far, we have successfully demonstrated the abilities and potential of

the Brownian motion model to describe various scenarios in heavy-ion collisions at intermediate energies. Its ability to traverse different dynamical trajectories makes it particularly suitable for the study of multifragmentation, which is beyond the reach of many traditional transport models. It is also superior to many models with stochastic extensions in that it treats dissipation and fluctuation on an equal footing. More explicit introductions of many-body correlations possibly with connections to quantal expectation values are under consideration. In the future, it is of great interest to confront the optimized Brownian motion model to experimental data. We have also in mind the goal of studying the fragmentation mechanism. For example, we have looked at whether and when the central region of a fragmented system enters the mechanically unstable region and the findings seem to favor the spinodal decomposition mechanism. A more careful inspection is planned.

As a final note, while the Fokker-Planck/Langevin approach has been motivated here by the Boltzmann equation, one can think about circumventing the latter in the future and deriving the coefficients for the equation directly from microscopic theory, upon separating slow coarse-grained nucleon motion from fast inter-nucleon motion [89].

Chapter 4

Investigating “hierarchy effect” in multifragmentation at Fermi energies with the Brownian motion model

The INDRA collaboration performed a series of experiments for different colliding systems at Fermi energies and studied the fragmentation of the quasiprojectiles [5]. For many of the systems studied, the experimental observations seemed to suggest the presence of a “hierarchy effect” between the charge and the parallel velocity of the quasiprojectile-like fragments (PLF): “the ranking in charge induces in average a ranking in the average parallel velocity, the heaviest fragment is the fastest and is focused in the forward direction relative to the QP recoil velocity” [5]. The hierarchy effect suggests that memories of the entrance channel play an important role in collisions at intermediate energies. This essentially rules out the statistical decay approach under the equilibrium assumption and calls for a dynamical treatment of the collision and the multifragmentation processes.

We will revisit the hierarchy effect by simulating the collision of Ta+Au

at 39.6 MeV/u with the Brownian motion model and compare our results with the experimental findings.

4.1 Simulation setup: physical inputs and selection of impact parameter b

The transport model used is the Brownian motion model, as described in Chapter 2, with essentially identical physical inputs. The mean-field potential used is of the same form as Eqn. (2.3) with parameters fitted to reproduce the binding energy $E/A = -16$ MeV/nucleon, the incompressibility $K = 200$ MeV and the symmetry energy $E_{\text{sym}} = 30.3$ MeV at normal density ρ_0 . The nucleon-nucleon cross section employed is energy-dependent and with empirical in-medium modifications,

$$\sigma_{\text{NN}}(E_{\text{lab}}, \rho) = \sigma_{\text{NN}}^{\text{free}}(E_{\text{lab}}) \exp \left[-\alpha \frac{\rho/\rho_0}{(1 + E_{\text{lab}}/E_0)^\beta} \right] \quad (4.1)$$

with $\alpha = 0.3$, $\rho_0 = 0.16 \text{ fm}^{-3}$, $E_0 = 137 \text{ MeV}$, $\beta = 1.4$ and a maximum cuff-off at 150 mb, similar to Eqn. (3.1). $\sigma_{\text{NN}}^{\text{free}}(E_{\text{lab}})$ is a parametrization of the free energy-dependent nucleon-nucleon cross section [85].

Another important input for running the simulations is the selection of the impact parameter b . The impact parameter is not an experimental observable and therefore can only be deduced from the relevant centrality observable. In the experiment, the level of violence of the collisions is measured by $E_{t12}/E_{\text{c.m.}}$, the ratio of the total transverse energies of light charge particles with $Z \leq 2$ to the center of mass energy [5]. The experimental data for the Ta+Au system at 39.6 MeV/nucleon shows that for majority of events, with PLF multiplicity M_{IMF} ranging from 2 to 4 and with the charge of the heaviest fragment Z_1 between 10 and 55, the distributions of

$E_{t12}/E_{c.m.}$ are densest in the range between 10% and 20% [5]. A sensible goal of choosing the impact parameters for the simulations is to mimic the distributions of $E_{t12}/E_{c.m.}$ to our best ability.

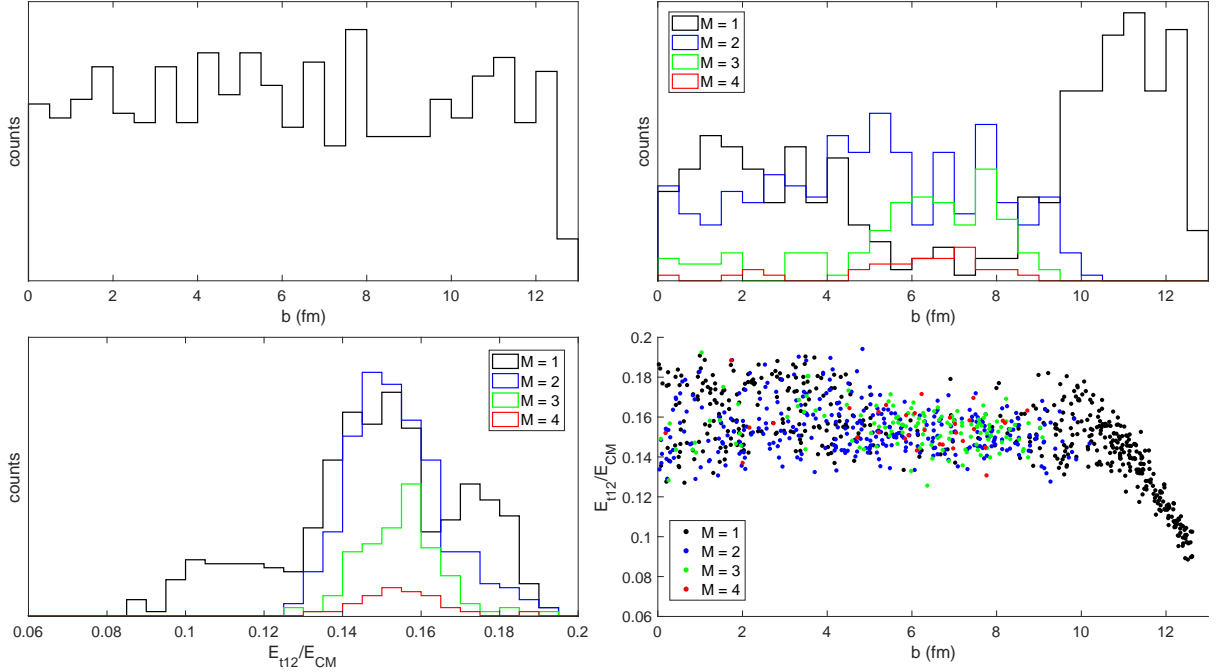


Figure 4.1: Centrality analysis of the events in the simulation. (a) shows the distribution of the actual impact parameter b sampled in the simulation; (b) shows the histograms of b for each event group of definite PLF multiplicity M_{IMF} ; (c) shows the distributions of centrality estimator $E_{t12}/E_{c.m.}$ for each event group specified by M_{IMF} ; (d) displays the relationship between $E_{t12}/E_{c.m.}$ and b within the events that are color-coded by their corresponding M_{IMF} .

The distribution of impact parameter we settled for in the end is a uniform distribution from 0 to $b_{\max} \approx 12.7$ fm. The actual distribution sampled in the simulation is shown in panel (a) of Fig. 4.1. The total number of events simulated is about 1500. In panel (b) of Fig. 4.1, we sorted the events by their corresponding PLF multiplicity M_{IMF} . Note that events with $M_{IMF} > 4$ are extremely rare and are thus omitted in this and the following panels. Most of the fragmentation events of the

quasiprojectile in the simulation took place with an impact parameter under 10 fm. Note, in particular, there is also a surge of fragmentation events, with $M_{\text{IMF}} \geq 2$, and a depletion of non-fragmentation events, $M_{\text{IMF}} = 1$, between 4 and 9 fm. Exit channels corresponding to fragmentation seem to be activated most likely under semi-central or semi-peripheral conditions. The centrality estimator $E_{t12}/E_{\text{c.m.}}$ sorted by M_{IMF} is summarized in panel (c) of Fig. 4.1. For M_{IMF} between 2 and 4, the bulk part of the events have their estimators $E_{t12}/E_{\text{c.m.}}$ to be in the range between 12% and 18%, which is in a reasonable agreement with what was reported in the experimental data [5]. Hence, this choice of uniform sampling of the impact parameter b can be justified. In panel (d) of Fig. 4.1, we tested the sensitivity of the centrality estimator $E_{t12}/E_{\text{c.m.}}$ to the impact parameter b in the simulation. From the perspective of the simulation, we did not find a strong correlation between $E_{t12}/E_{\text{c.m.}}$ and b when b is under 10 fm. This echoes with the observation in (b) that most of the fragmentation are limited to events with b under 10 fm. Normally, one would expect a larger $E_{t12}/E_{\text{c.m.}}$ with a smaller b , as there are more participant nucleons in the reaction zone getting deflected into transverse directions in more central events. However, when fragmentation is present, the initial center of mass energy can transfer not only into the transverse kinetic energy of free nucleons, but also into energy necessary to break up the colliding systems and to form clusters. It is the fragmentation involved that muddy up the expected trend between $E_{t12}/E_{\text{c.m.}}$ and b . When b is greater than 10 fm and practically no fragmentation occurs, the expected trend is recovered.

4.2 Comparison with experimental data

In this section, we will be first comparing the charge Z , the parallel velocity V_z and certain angular $\theta_{F/QP}$ (defined in details in the subsequent text) distributions of the PLFs between the experimental data and the simulation results, in the form of histograms. The two subsections will dive into more details of the charge and parallel velocity distributions by comparisons of the extracted means and standard deviations and discuss the observation and existence of the “hierarchy effect”.

Before confronting the experimental data right away, it is of importance to point out some of the differences of the fragments predicted by the model and to justify the comparison. The fragments produced in the simulations should be treated as primary fragments, which may undergo secondary statistical decay before reaching detectors. The simulation of statistical decay of primary fragments is out of the scope of the underlying transport code and is thus not taken into account. Still, we would like to discuss some qualitative and semi-quantitative comparisons between the primary fragments from transport theory and the actual fragments analyzed in the experimental data. One should be reminded that we aim to demonstrate the so-called “hierarchy effect”, due to the entrance channel effects in the distribution and properties of the PLFs. These entrance channel effects are not expected to emerge from modifications from the statistical decay of primary fragments, but rather as a result of the collision dynamics. Hence, for the purpose of studying entrance channel effects in multifragmentation, it is justifiable to look plainly at primary framgments in most cases.

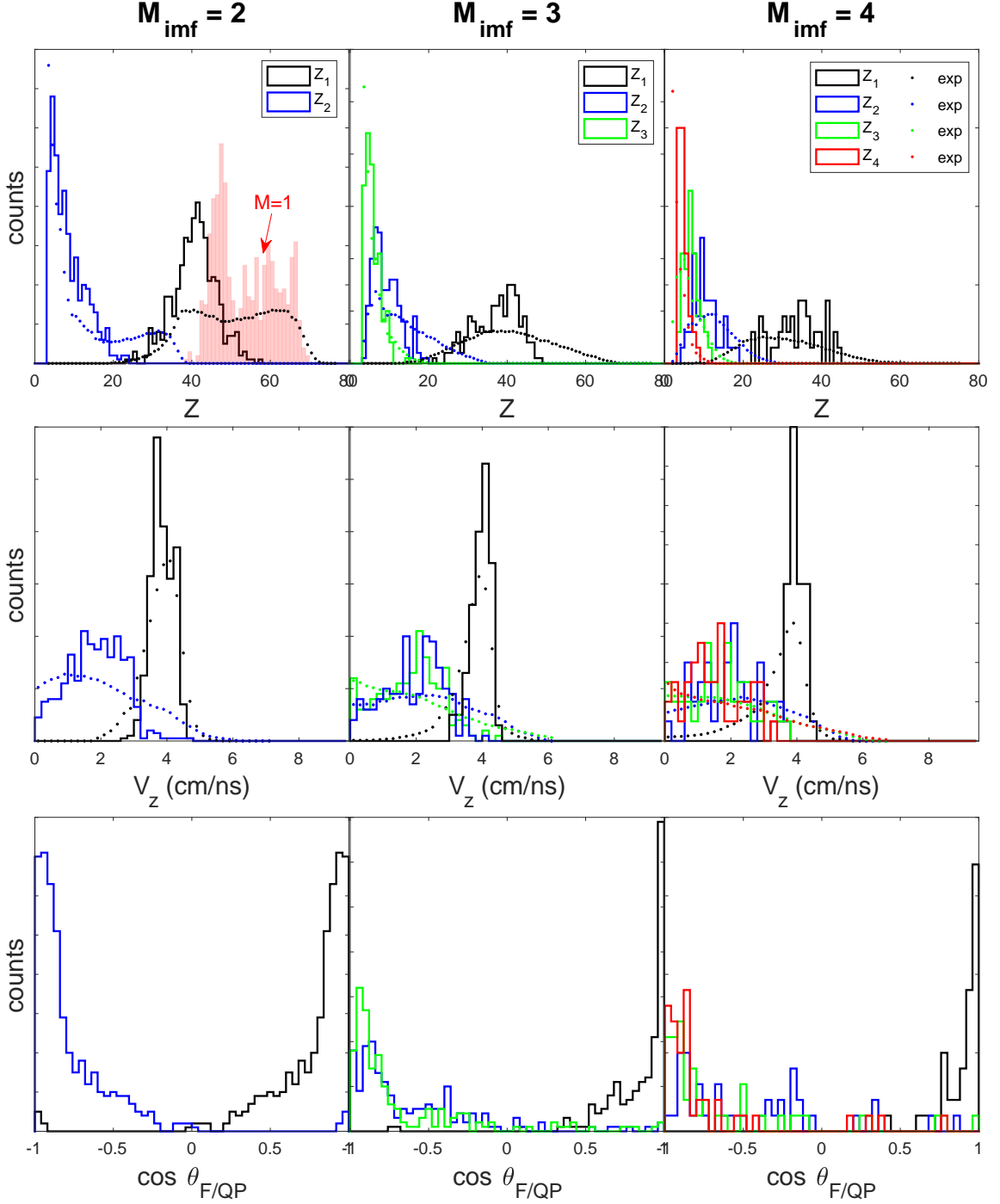


Figure 4.2: Charge Z (uppermost panels), parallel velocity V_z (middle panels) and angular $\theta_{F/QP}$ distributions for the Ta+Au system at 39.6 MeV/nucl. The columns correspond to events of different PLF multiplicity M_{imf} . Fragments are color-coded and sorted by their charge, with Z_1 being the heaviest and $Z_{M_{\text{IMF}}}$ being the lightest. Simulation results are shown as histograms, and data of charge and velocity distributions extracted from Ref. [5] are shown as solid dots. The theoretical charge distribution of events with $M_{\text{imf}} = 1$ is displayed as a semi-opaque shaded area in the background of the leftmost panel in the first row. (See the text for more discussion.)

For the comparison, we will focus on the charge Z distribution, the distribution of the velocity component V_z in the direction of the beam, and the angular distribution of the PLFs for events with M_{imf} between 2 and 4. The angle $\theta_{F_i/QP}$ chosen for the angular distribution is the angle between the velocity of the i^{th} fragment in the frame of the quasiprojectile (QP) and the quasiprojectile velocity \mathbf{V}_{QP} in the center of mass frame. To be more specific, $\cos(\theta_{F_i/QP})$ is defined as

$$\cos(\theta_{F_i/QP}) = \frac{(\mathbf{V}_i - \mathbf{V}_{QP}) \cdot \mathbf{V}_{QP}}{|\mathbf{V}_i - \mathbf{V}_{QP}| |\mathbf{V}_{QP}|}, \quad (4.2)$$

where \mathbf{V}_i is the velocity of the i^{th} largest fragment in the center of mass frame and \mathbf{V}_{QP} is the velocity of the constructed quasiprojectile,

$$\mathbf{V}_{QP} = \frac{\sum_{i=1}^{M_{\text{imf}}} Z_i \mathbf{V}_i}{\sum_{i=1}^{M_{\text{imf}}} Z_i}. \quad (4.3)$$

In both the experimental and theoretical analysis, the PLFs were selected as fragments with charge $Z > 2$ and a positive velocity $V_z > 0$ in the center of mass frame. The events were sorted in terms of their PLF multiplicity. Within each type of events, the PLFs are sorted by their charge with Z_1 being the fragment with the greatest charge and $Z_{M_{\text{imf}}}$ being the one with smallest charge.

In the first two rows of Fig. 4.2, we show both the experimental data and the simulation results for the charge Z distribution and the velocity V_z distribution. The theoretical distributions are normalized to have the same total counts of events as the experimental counterparts.

The data and the simulation agree coarsely on a semi-quantitative level. The positions of peaks and the spread of the experimental distributions are roughly reproduced by the distributions of the simulated primary fragments. An exact match is not expected, as the comparison is done between

the primary fragments predicted in theory and the actual fragments picked up in experiments. The distributions in experimental data tend to be wider than those predicted by the theory. Statistical decay is likely to help broaden the narrower theoretical distributions in both charge Z and velocity V_z . For the charge distribution corresponding to events with $M_{\text{IMF}} = 2$, there appear two peaks in the data for both of the PLFs, Z_1 and Z_2 , while the model predicts a single peak only. The theoretical peak of Z_1 -fragments roughly corresponds to the lower charge peak in the data, while the higher charge peak in the data is missing. This is again believed to be because of the lack of “after-burners” treatment for the primary fragments, especially those produced in events with $M_{\text{IMF}} = 1$ in the simulations. We put the charge distribution of the projectile-like remnants for $M_{\text{IMF}} = 1$ events in the simulations in the background of the charge distribution for $M_{\text{IMF}} = 2$. It is observed that the $M_{\text{IMF}} = 1$ remnants in the simulations have largely filled up the missing peaks and areas around the higher charge peak in data for Z_1 . Thus, it can be conjectured that taking into account the statistical decay of the remnants in low multiplicity events with $M_{\text{IMF}} \leq 2$ will be likely to help recover the missing peak in the case of $M_{\text{IMF}} = 2$ as well as to contribute to fragments with charge $Z > 50$ in high multiplicity events with $M_{\text{IMF}} > 2$.

The experimental claims regarding the velocity and the angular distributions of the Z_1 -fragments, in relation to other fragments, can be confirmed. For all multiplicities, it is observed in both experiment and simulations that the largest fragment has a larger velocity component along the beam axis z compared to the other fragments, i.e.,

$$\langle V_z^{Z_1} \rangle > \langle V_z^{Z_i} \rangle \quad (4.4)$$

for $2 \leq i \leq M_{\text{IMF}}$. Similarly for the angular distributions, regardless of the multiplicity, the largest fragment tends to peak forward when the quasi-projectiles break up, i.e.,

$$\langle \cos(\theta_{F_1/QP}) \rangle > 1, \quad (4.5)$$

$$\langle \cos(\theta_{F_i/QP}) \rangle < 1, \quad (4.6)$$

for $2 \leq i \leq M_{\text{IMF}}$. Both of the observations suggest that the largest fragment, being fastest and forward-peaked, retains most of the momentum of the projectile, which serves as evidence for the presence of entrance channel effects for the fragmentation of the system Ta + Au at 39.6 MeV/nucleon, in agreement with the experimental observation of the “hierarchy effects” [5].

It remains to be investigated whether a similar positive correlation between charge and velocity exists for the fragments $Z_2 - Z_{M_{\text{IMF}}}$, which is not immediately clear and evident from the histograms. In what follows, we will compare the means and the standard deviations extracted from the distributions in Fig. 4.2, which provide us with succinct abstractions of the underlying distributions. Extra care should be taken though when the distributions have more peaks than one, as the mean is no longer indicative of the positions of the peaks.

4.2.1 Charge distribution

In Fig. 4.3, we show the means and standard deviations extracted from the theory and the data for events with M_{IMF} between 2 and 4. As is mentioned before, the charge distribution of the Z_1 -fragment in the data for $M_{\text{IMF}} = 2$ has two peaks, so the mean extracted in that case does not cor-

respond to any of the peak in the data but rather lies somewhere between two peaks. The mean extracted from the simulation for Z_1 for $M_{\text{IMF}} = 2$ mostly corresponds to the lower charge peak in experiment and is hence to the left of the experimental mean. For $M_{\text{IMF}} = 2$ and 3, the experimental means are reproduced by the theoretical simulations reasonably well, and the deviations do not exceed 2 protons in most cases. The theoretical standard deviations tend to be narrower than their experimental counterparts, which suggest that the theory still fails to probe the entire variety of exit channels accessible in the actual collisions. We reiterate here that parts of those missing exit channels might be recoverable by feeding the simulated primary fragments to secondary statistical decay.

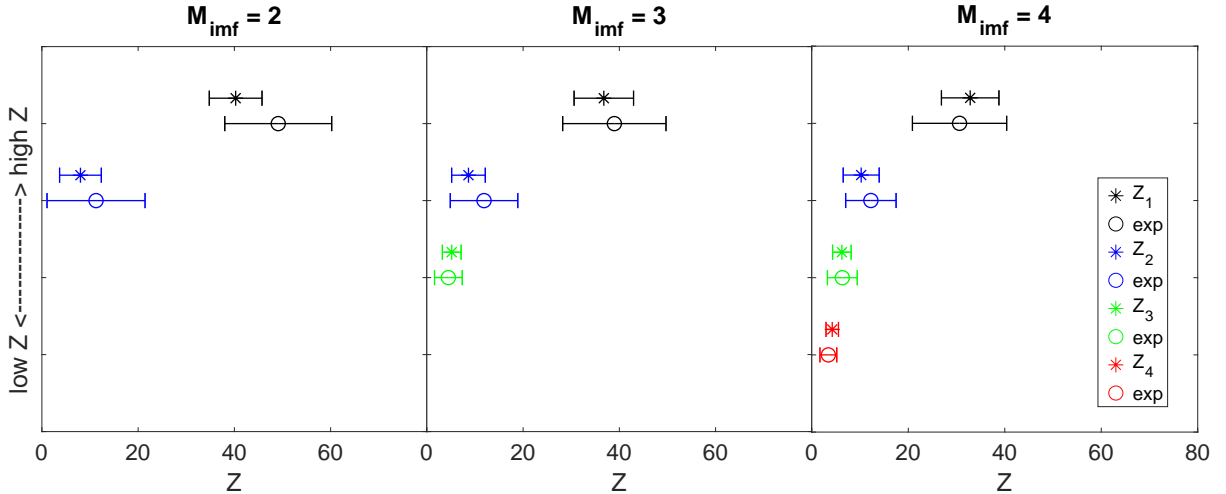


Figure 4.3: Means and standard deviations of the charge distributions sorted by the PLF multiplicity (from $M_{\text{IMF}} = 2$ on the leftmost to $M_{\text{IMF}} = 4$ on the rightmost). Within each panel, the fragments are ranked by their charge (with the greatest near the top and the lightest near the bottom) and color-coded accordingly. The asterisks represent theoretical means and the open circles represent experimental means, both accompanied by horizontal “error bars” of the size of the corresponding standard deviation.

In Fig. 4.4, we categorize the simulated events further by their impact parameter b in the range from 0 to 10 fm. Each row of Fig. 4.4 corresponds

to a 2-fm range of impact parameter. However, note that, since it is impossible to differentiate the experimental events by b or any other centrality measure with what is available in Ref. [5], each column has the identical experimental means and standard deviations in all panels. The standard deviations for the simulations are comparatively narrow, as they take into account the variations among events within the narrow 2-fm impact parameter range, and thus they should not be directly compared with the experimental standard deviations, which cover the entire spectrum of centrality. As the impact parameter b increases, i.e., as the collisions get more peripheral, the average charge of Z_1 shifts towards greater charge value with greater resemblance to the original projectile. It is thus expected that the entrance channel effects for Z_1 grow as b grows. One should also notice that, even in the most central range of impact parameters [0, 2] fm, it is still possible to distinguish the largest fragment with Z_1 from all the other fragments with smaller charge. This goes to show that the system does not form a compound nucleus at thermal equilibrium even in the most central collisions. The Z_1 -fragment can largely be regarded as a remnant of the projectile. Other fragments with smaller charge are much more less distinguishable among themselves, which suggests that they possibly have a similar origin that is different from the largest fragment, especially for the more peripheral events. A relatively good agreement for the mean charges between the theory and the experiment is obtained for the range of impact parameter between 4 and 8 fm for $M_{\text{imf}} = 3$ and 4. That interval of impact parameter also overlaps largely with the interval of b , [4, 9] fm, with a surge of fragmentation events in the simulation.

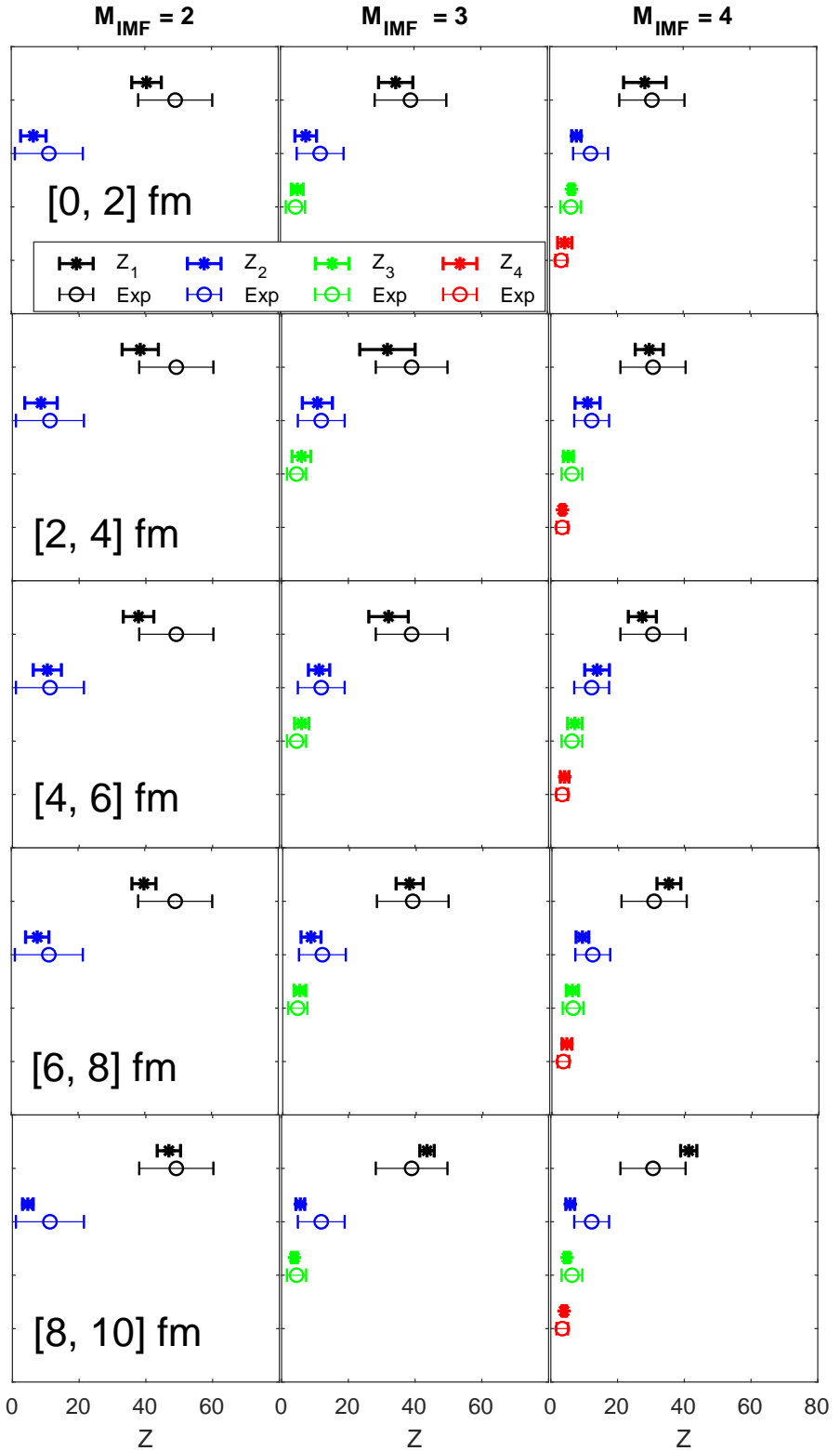


Figure 4.4: Means and standard deviations of the charge distributions sorted by the multiplicity M_{IMF} in ascending order from left to right and by the impact parameter b in ascending order from top to bottom. The distributions within each panel are further ranked by their corresponding charge Z and color-coded. Theoretical means are represented by asterisks, and experimental ones are by open circles. Standard deviations are represented as “error bars”.

4.2.2 Velocity distribution

We display both the theoretically and the experimentally extracted means and standard deviations of the velocity V_z distributions, sorted by M_{inf} as before, in Fig. 4.5. Just like in the case of charge Z , the theoretical standard deviations are narrower than the experimental ones, which again suffers from the fact that only primary fragments are produced in the simulations. The agreement of the extracted means between theory and experiment is acceptable, especially when one considers that we did not adjust or temper with any parameters in the model to force a fit to the data. For the largest fragment with Z_1 , the theory tend to predict a faster velocity V_z along the beam axis. The over-prediction gets even more serious when the multiplicity M_{inf} gets larger. V_z of the other fragments with smaller charge are accordingly underpredicted in the simulations, following from the conservation laws. This indicates that the collisions simulated tend to have a weaker stopping than the actual collisions in the experiment. Possible culprits for the weaker stopping include our choice of range of impact parameters and our naive parametrization of the nucleon-nucleon cross sections in Eq. (4.1).

Putting the issue of somewhat weaker stopping aside, we observe similar trends and properties for the velocity distributions across the simulations and the data. In particular, the Z_1 -fragment has the greatest V_z , which distinctively differentiates it from other fragments with smaller charge as well as smaller V_z . Such a divide between the Z_1 fragment and the other fragments has already been seen in the previous discussion about charge distribution.

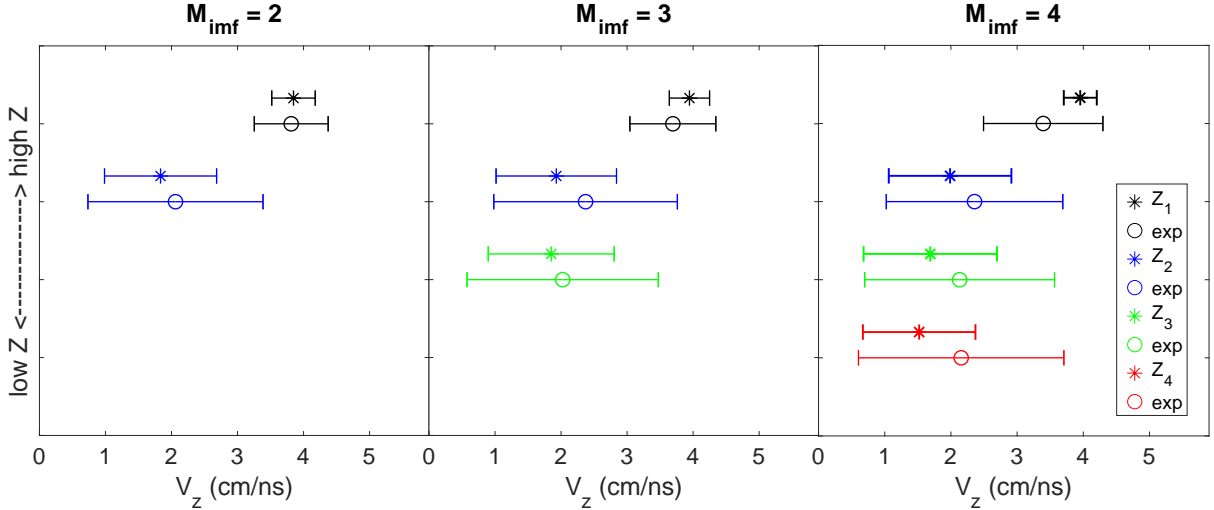
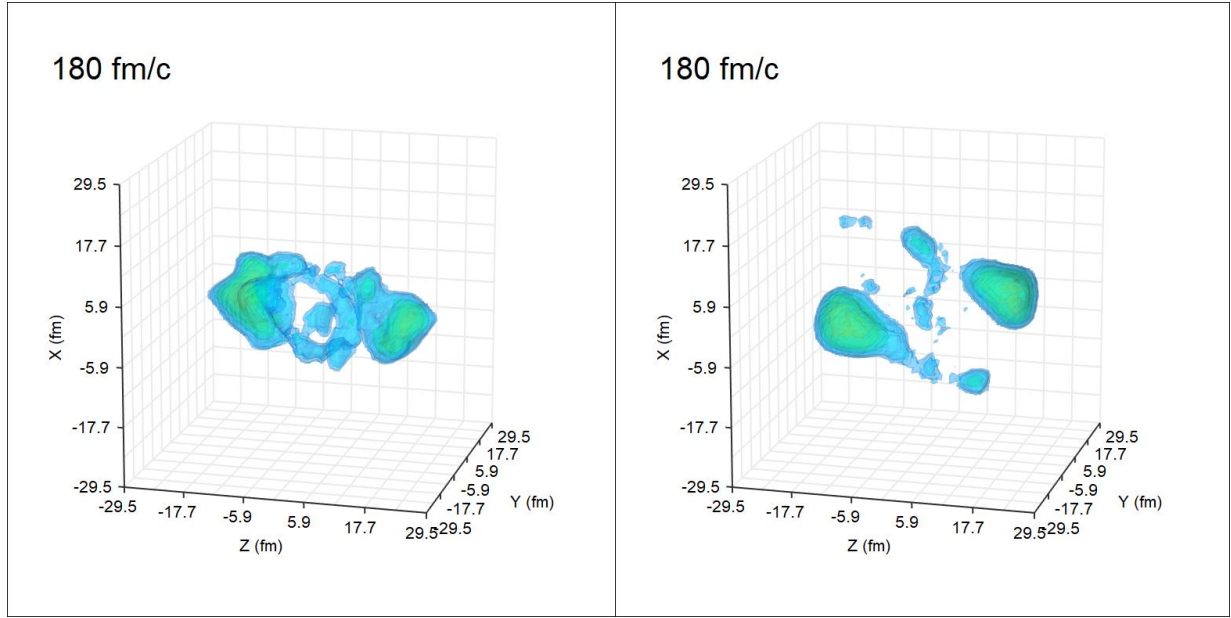


Figure 4.5: Means and standard deviations of the distribution of parallel velocity V_z , organized in a way similar to Fig. 4.3.

We would like to attribute these divides in the form of charge and velocity to the fact that these fragments have two distinct sources: the projectile-like remnant and the mid-rapidity remnant. The projectile-like remnant retains obviously most of the entrance channel memories. The mid-rapidity source is conjectured to be linked to the formation of a neck in the experimental paper [5]. In the simulations, though, we have not been able to gather enough information and evidence to support the transient existence of a neck. In Fig. 4.6, we show two events in the simulation, with one corresponding to a central event and the other to a semi-peripheral event. In the more central event (a), the projectile and the target were strongly deformed, with a lot of mass accumulating in the central zone. The nucleons in the central zone were substantially decelerated and formed clusters as they expanded and escaped from the central zone. In the semi-peripheral event (b), the projectile and the target passed through each other much more swiftly, leaving behind a thinning tail. The depletion of matter in the central region also occurred much more rapidly. Both

the thinning tails and the matter in the central zone belong to the mid-rapidity region. Neither scenario in (a) or (b) would fit exactly the “neck” formation conjecture. It could be that the neck is just far too transient and fragile to be picked out or that many competing fragmentation mechanisms were involved. Note also that the two pictures presented here by no means exhaust all scenarios that occurred in the simulation.

A rather weak hierarchy effect, i.e., a positive correlation between charge Z and velocity V_z , can be seen in both the simulations and the experimental data for all the fragments for all multiplicities in Fig. 4.5. This hierarchy effect, albeit weak, serves as a manifestation of the entrance channel effects in play nonetheless.



(a) Simulation with $b \approx 3$ fm.

(b) Simulation with $b \approx 9$ fm.

Figure 4.6: Density plots of two simulated events at 180 fm/c. Event (a) is central, while event (b) is semi-peripheral. The density contours are ranked by $0.1 \rho_0$, $0.2 \rho_0$, $0.4 \rho_0$, $0.6 \rho_0$ and $0.8 \rho_0$ from the outermost to the innermost. Neither case provides any direct proof of the neck formation.

In Fig. 4.7, we further divide the events based on their impact parameters. The theoretical standard deviations are narrow because of the small range of impact parameters in each group of events. Other than events corresponding to $M_{\text{inf}} = 4$ and $b \in [0, 2]$ fm, which suffers probably from a small sample size, all other event groups exhibit the “hierarchy effect” similar to those in the experimental data. Such ranking effects seem to be strongest for semi-central events with impact parameter b ranging from 2 to 6 fm, particularly for highly fragmented events. The strong ranking effects observed in the more central events are manifestations of the en-

trance channel effects and can potentially be attributed to the decay of a strongly deformed and out-of-equilibrium source, such as the fracture of a “neck” connecting the projectile and te target as proposed in the experimental paper [5]. For greater impact parameters with $b > 8$ fm, the divide between the Z_1 fragment and the others is more prominent, and the velocity gradient of the smaller fragments also appear much weaker. As the collisions get more peripheral, the smaller fragments become more homogeneous in terms of both charge and velocity. One may infer that fragments in peripheral collisions are more likely to come from a nearly equilibrated source possibly originating from the small and constrained reaction zone at mid-rapidity.

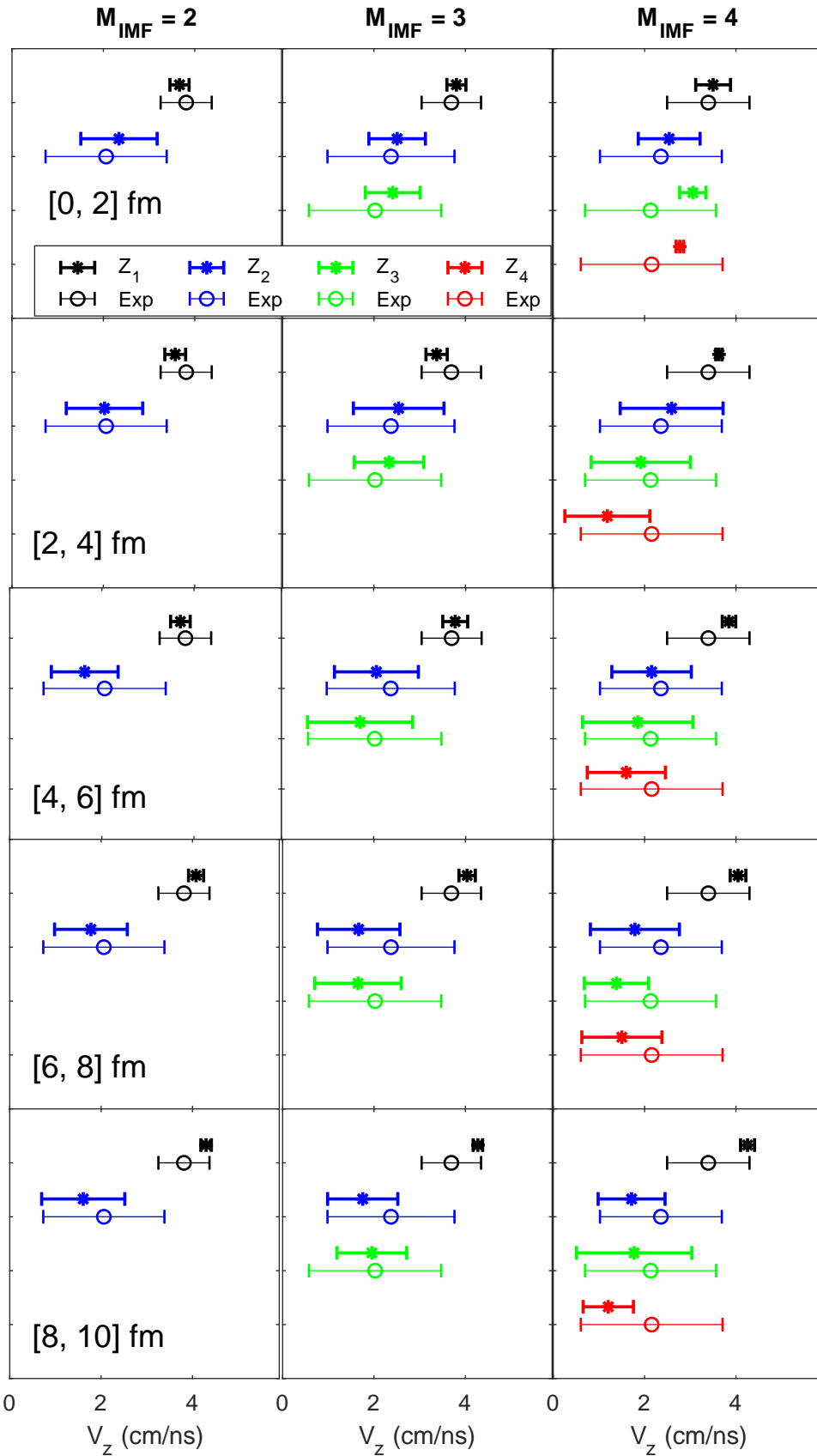


Figure 4.7: Means and standard deviations of the distribution of parallel velocity V_z , sorted by the impact parameter b in the simulation and organized in a way similar to Fig. 4.4.

4.3 Absence of the “hierarchy effect” for U + C

As is described in Ref. [5], no “hierarchy effect” was reported for the U + C system at the lab energy $E = 24$ MeV/nucleon, especially when the multiplicity M_{IMF} is low.

We investigated the same collision system within our model. The first thing we noticed in the simulations is that, regardless of the impact parameter, the two incoming nuclei tend to fuse together to form a compound nucleus with minor deformations and non-negligible rotational motion. The initial kinetic energy appears to be dissipated by emission of free nucleons and in the form of internal and rotational energy of the compound nucleus formed. Within the time scale we considered, up to 300 fm/c, we observe no fragmentation of the compound nucleus and thus, we are unable to produce the charge and velocity distribution of the PLFs, as we did for the case of Ta + Au at 39.6 MeV/nucleon. Nonetheless, we speculate that the compound nuclei predicted by our simulations are susceptible to statistical decay, given enough time and accuracy of the description of the energy and structure of the compound nucleus, both of which are lacking in our semi-classical transport approach.

The absence of the correlation between the ranking of charge Z and velocity component V_z for the U + C system in experiments is more characteristics of the fission of an equilibrated source. This is, in fact, in agreement with the theoretical prediction of a single primary source.

The strikingly different behaviors between the Ta + Au system and the U + C in the simulations can be understood as results of their different dominant decay channels: for Ta + Au, where the projectile and target

are comparable, fragmentation dominates; for $U + C$, the fission channels dominate, due to the high fissility of U . Fission or other sorts of decay of an equilibrated system typically require a much longer time scale and a rather sophisticated description of the system and is thus beyond the scope of our model.

4.4 Summary

In this chapter, we investigated the behaviors of heavy-ion collisions at Fermi energies and, in particular, the entrance channel effect reported experimentally [5] for the PLFs. We simulated the primary fragments in the $Ta + Au$ system at 39.6 MeV/nucleon. Despite the fact that we did not produce exactly the final fragments that were picked up in the experiments for a lack of secondary statistical decay treatment, we find that the overall properties and trends of the experimental fragment distributions also survive in the distributions of the simulated primary fragments. In particular, we are able to confirm the so-called “hierarchy effect” in the simulation, in sharp contrast to what might be expected from decay from an equilibrated source. The fact that the PLF with the greatest charge also travels fastest can be attributed to the retention of the projectile memory. For certain semi-central collisions, we also observe a strong correlation between the charge ranking and the velocity ranking even for the smaller fragments, which might be seen as circumstantial supporting evidence for the “neck formation” conjectured by the experimental efforts [5].

We also briefly looked at the $U + C$ system at 24 MeV/nucleon, for which the experiment collaboration reported no “hierarchy effect”. Our

simulations of U + C does not predict any sort of fragmentation or fission, but rather a rotating compound source. This, however, is not entirely at odds with the experimental observation, as fission or statistical decay of a nearly equilibrated source is indeed consistent with the lack of “hierarchy effect” observed.

Finally, this project, to our best knowledge, for the first time, attempt to address the “hierarchy effect” from a dynamical standpoint with the use of a stochastic transport theory. Our simulations confirm the “hierarchy effect” as an important entrance channel effect for collisions at Fermi energies, when the multifragmentation mechanism dominates. In this study, we did not adjust either the mean-field potentials or the NN -cross sections. It will be interesting, however, to test whether there is any sensitivity of this effect to these inputs of nuclear interactions in the future. For a more thorough and detailed comparison with data in the future, it will also be of great importance and necessity to combine the use of transport simulations and that of statistical decay models.

Chapter 5

Nonequilibrium Green's function approach for many-body quantum systems

5.1 Introduction

Quantum mechanics has taken root in a bulk part of contemporary nuclear theory, from the Hartree-Fock method [90–92] to chiral effective field theory [93–95] in nuclear structure, from the distorted-wave Born approximation [96, 97] and to the coupled-channel techniques [98–100] in low-energy nuclear reactions, just to name a few. The development of time-dependent quantum approaches is not on par with their static counterparts, with the most notable one being the time-dependent Hartree-Fock (TDHF) theory [26, 27, 101–104]. However, the bare form of the TDHF theory is a mean field theory neglecting many-body correlations, which does not provide sufficient stopping and thermalization to describe intermediate or high energy heavy-ion collisions [105]. The community of intermediate-energy heavy-ion collisions continues to rely predominantly on semi-classical transport models based on the Boltzmann-Uehling-Uhlenbeck (BUU) equation, where

quantum effects such as Pauli-blocking [106, 107], the uncertainty principle, through the use of wavepackets [108, 109], and antisymmetrization [110, 111], can be partially incorporated. While a vast majority of the semi-classical transport models have demonstrated their applicability and strengths through comparison with experimental data [66, 112–114], questions concerning the validity of the quasi-particle picture and the effects of quantum correlations linger. Moreover, as already pointed out in Ref. [115], the semi-classical methods, detached from the rapidly developing quantum techniques employed in other fields of nuclear physics, are difficult to improve systematically. Even attempts to take into account the missing classical many-body correlations through the incorporation of fluctuations [18, 23, 116, 117] will not be able to recover all effects of quantum correlations, as they are of fundamentally different nature. A fully quantum-mechanical transport model for heavy-ion collisions is called for.

Solving the many-body Schrödinger equation exactly is almost always a forbiddingly daunting task. Fortunately, more often than not, one is interested in one-body observables, for which a complete many-body wavefunction is not necessary. One can hopefully obtain enough information from one-body reductions, such as one-body density matrix or one-body Green’s function, by integrating out the irrelevant degrees of freedom. In obtaining a closed equation of motion, the TDHF theory approximates the two-body density matrix by products of one-body density matrix and consequently neglects all two-body correlations [26, 83]. In contrast, in the non-equilibrium Green’s function (NGF) theory, two-body correlations are encapsulated in the self-energy and a systematic order-by-order approximation of the self-energy is possible [115, 118]. As a result, the NGF theory

is more versatile and promising than the TDHF theory in the description of intermediate-energy heavy-ion collisions, where effects of two-body correlations are usually non-negligible.

An NGF code for the description of nuclear collisions in one dimension was developed by Rios *et al.*, and the mean field dynamics within NGF was discussed in Ref. [115]. The current paper serves as an extension to the previous work. Before we present the extensions and discuss the new results, let us briefly go over some relevant concepts and definitions in the NGF theory. (See Refs. [115, 118] for more details.) Within the NGF theory, fermionic many-body systems can be characterized in terms of the single-particle Green's functions

$$G^<(x_1, t_1; x_2, t_2) = i\langle \phi^\dagger(x_2, t_2) \phi(x_1, t_1) \rangle, \quad (5.1)$$

$$G^>(x_1, t_1; x_2, t_2) = -i\langle \phi(x_1, t_1) \phi^\dagger(x_2, t_2) \rangle. \quad (5.2)$$

Here ϕ and ϕ^\dagger are annihilation and creation operators in the Heisenberg picture, and the expectation value is taken with respect to the total wavefunction also in the Heisenberg picture. When $t_1 = t_2$, the same-time lesser Green's function $G^<$ is equivalent to the one-body density matrix up to a constant imaginary factor i . Thus, the lesser and greater Green's functions are often associated with the particle density and the hole density, respectively. One may also define Green's functions as functions of momentum and time arguments, by replacing the annihilation and creation operators in coordinate space by those in momentum space. Green's functions in coordinate space and Green's functions in momentum space can be converted into one another through Fourier transformation.

The equations of motion for the lesser and greater Green's functions

are the so-called Kadanoff-Baym equations [119],

$$\left[i\hbar \frac{\partial}{\partial t_1} + \frac{\hbar^2}{2m} \frac{\partial^2}{\partial \mathbf{x}_1^2} \right] G^{\leqslant}(\mathbf{1}, \mathbf{2}) = \int d\mathbf{x}_3 \Sigma_{\text{HF}}(\mathbf{1}, \mathbf{3}) G^{\leqslant}(\mathbf{3}, \mathbf{2}) \\ + \int_{t_0}^{t_1} d\mathbf{3} \Sigma^{+}(\mathbf{1}, \mathbf{3}) G^{\leqslant}(\mathbf{3}, \mathbf{2}) \\ + \int_{t_0}^{t_2} d\mathbf{3} \Sigma^{\leqslant}(\mathbf{1}, \mathbf{3}) G^{-}(\mathbf{3}, \mathbf{2}), \quad (5.3)$$

$$\left[-i\hbar \frac{\partial}{\partial t_2} + \frac{\hbar^2}{2m} \frac{\partial^2}{\partial \mathbf{x}_2^2} \right] G^{\leqslant}(\mathbf{1}, \mathbf{2}) = \int d\mathbf{x}_3 G^{\leqslant}(\mathbf{1}, \mathbf{3}) \Sigma_{\text{HF}}(\mathbf{3}, \mathbf{2}) \\ + \int_{t_0}^{t_1} d\mathbf{3} G^{+}(\mathbf{1}, \mathbf{3}) \Sigma^{\leqslant}(\mathbf{3}, \mathbf{2}) \\ + \int_{t_0}^{t_2} d\mathbf{3} G^{\leqslant}(\mathbf{1}, \mathbf{3}) \Sigma^{-}(\mathbf{3}, \mathbf{2}), \quad (5.4)$$

where we have used shorthand notations such as $\mathbf{1}$ to represent (\mathbf{x}_1, t_1) . The different $\Sigma(\mathbf{1}, \mathbf{2})$ are the so-called self-energy, and provide an approximate description of correlations in the system. They can be expanded diagrammatically, and will be discussed further in the next section. The retarded (+) and advanced (-) functions are defined through

$$F^{\pm}(\mathbf{1}, \mathbf{2}) = F^{\delta}(\mathbf{1}, \mathbf{2}) \pm \theta[\pm(t_1 - t_2)] [F^{>}(\mathbf{1}, \mathbf{2}) - F^{<}(\mathbf{1}, \mathbf{2})], \quad (5.5)$$

where F^{δ} represents a singular part at $t_1 = t_2$. It has been shown that one can derive the BUU equation from the Kadanoff-Baym equation by approximating the interacting Green's functions with the free Green's functions in a uniform system [118], which demonstrates a strong link between the NGF approach and the semi-classical models based on the BUU equation. On the other hand, in contrast to classical transport theories, the correlation integrals, integrating over the entire history, lead to memory effects.

To advance the application of these techniques to nuclear physics, we draw on rigorous NGF results and combine them with phenomenology

taking into account the context of numerical limitations and the expectations regarding physical characteristics of the nuclear systems. The aim of this paper is to show the applicability of NGF in a variety of settings that are relevant for nuclear theory, in preparation for the application to simulations of nuclear collisions. The organization is as follows. In Sec. 5.2, we will discuss the introduction of isospin degrees of freedom and the incorporation of short-range two-body interactions. In Sec. 5.3, we will describe the preparation of finite correlated nuclear systems within the NGF approach. Sec. 5.4 examines the isovector oscillation of slabs in one dimension and Sec. 5.5 demonstrates how to boost a finite system to move at a constant velocity. In the end, we will give a summary and remark on the prospects in Sec. 5.6.

5.2 Extending the non-equilibrium Green's function approach for nuclear systems

To describe realistic nuclear systems at moderate energies, an obvious but nonetheless crucial extension to the previous NGF model [115] is to introduce isospin dependence in the Green's functions. This can be readily achieved by introducing two versions of the Green's functions, of the self-energies, and of other relevant quantities, one for the neutron subsystem and the other for the proton subsystem. The separation is rather straightforward in practice, but comes with the cost of doubling the memory requirement for the computation and doubling the number of Kadanoff-Baym equations to be solved simultaneously. The mapping from 1D neutron or proton densities to 3D densities continues [115] to

follow the relation from the Hugenholtz-van Hove theorem: $\rho_{n/p}^{3D} = \xi \rho_{n/p}^{1D}$ with $\xi \approx 0.1217 \text{ fm}^{-2}$. In what follows, the subscripts n and p , indicating the particle species, will be dropped for the sake of brevity whenever no confusion arises.

The bulk part of mean-field interaction U independent of isospin follows closely from that in Ref. [115],

$$U(\rho) = \frac{3}{4}t_0\rho + \frac{2+\sigma}{16}t_3\rho^{1+d}, \quad (5.6)$$

with the parametres $t_0 = -2150.1 \text{ MeV fm}^3$, $t_3 = 14562 \text{ MeV fm}^{3(1+d)}$ and $d = 0.257$ fitted to reproduce properties of symmetric nuclear matter at saturation density. With the mean-field U dependent on the total baryon density, the evolutions of the neutron Green's functions and the proton Green's functions are coupled right from the very beginning. Upon differentiating the isospin degrees of freedom, we also introduce a dependence on isospin imbalance, $\delta = (\rho_n - \rho_p)/\rho$, into the nuclear equation of state where the form valid up to the second order in the imbalance is $\frac{E}{A}(\rho, \delta) = \frac{E}{A}(\rho, 0) + S(\rho) \delta^2$, with $S(\rho) = S_{\text{kin}}(\rho) + S_{\text{int}}(\rho)$. The first term $S_{\text{kin}}(\rho)$ stems from the difference in kinetic energies of the neutrons and protons for finite imbalance, while the true isospin dependence of the nuclear forces is reflected in the second term taken here in the form

$$S_{\text{int}}(\rho) = S_0 \left(\frac{\rho}{\rho_0} \right)^\sigma, \quad (5.7)$$

where the values $S_0 = 20.1 \text{ MeV}$, $\rho_0 = 0.16 \text{ fm}^{-3}$ and $\sigma = 0.35$ are currently used in the model. The isospin-dependent component of the mean field potential $U_{n/p}^{\text{sym}}(\rho, \delta)$ is given by

$$U_{n/p}^{\text{sym}}(\rho, \delta) = \partial[\rho S_{\text{int}}(\rho) \delta^2] / \partial \rho_{n/p}. \quad (5.8)$$

The Hartree-Fock self-energy Σ_{HF} is approximated as a sum of an isospin-independent component and an isospin dependent component,

$$\Sigma_{\text{HF}}(\mathbf{1}, \mathbf{2}) = \delta(\mathbf{1} - \mathbf{2})\{U[\rho(\mathbf{1})] + U_{n/p}^{\text{sym}}[\rho(\mathbf{1}), \delta(\mathbf{1})]\}. \quad (5.9)$$

The introduction of explicit isospin degrees of freedom to the system and of the isospin dependence to the mean field paves the way for future study on the nuclear symmetry energy as well as other isospin-dependent effects [120].

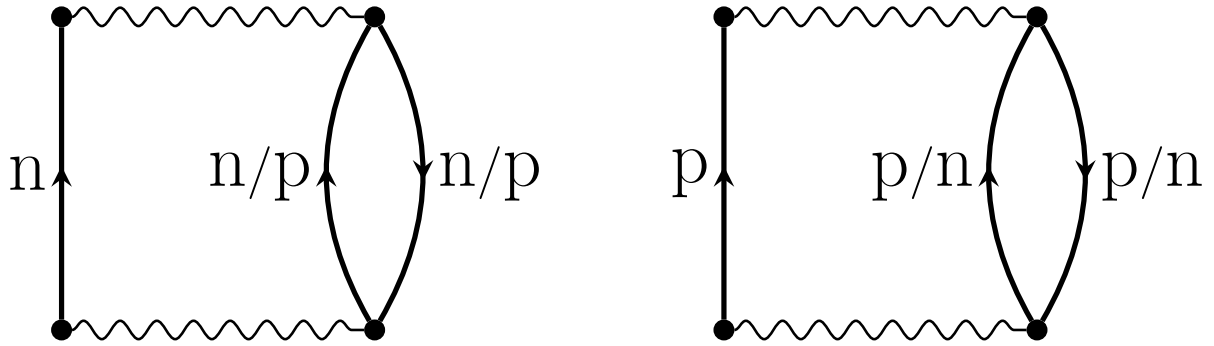


Figure 5.1: Second-order direct Born diagrams for neutron and proton self-energies $\Sigma_{n/p}$. Note that the particle species in the loop can be the same as or the opposite of the species of the propagator in the line to the left of the diagram. In the present work, the interaction transfers no isospin within the Born diagram, making the scattering independent of isospin.

One of the advantages of the non-equilibrium Green's function approach, over the more conventional TDHF theory, lies in its ability to incorporate two-body interactions into the residual self-energies Σ^{\leq} in the correlation integrals. The incorporation of two-body interactions induces quantum correlations in the system, which have been lacking in both mean field approaches and semi-classical approaches at the explicit level. In the current approach, we have included in the self-energies the correlation contribution represented with the diagrams in Fig. 5.1 by invoking the second-

order Born approximation. Effectively, this direct diagram describes the scattering within nn , pp and np pairs with different lines representing Green's functions of the suitable species. The corresponding self-energies Σ^{\leqslant} read

$$\begin{aligned}\Sigma^{\leqslant}(p, t; p', t') = & \int \frac{dp_1}{2\pi\hbar} \frac{dp_2}{2\pi\hbar} V(p - p_1) V(p' - p_2) \\ & \times G^{\leqslant}(p_1, t; p_2, t') \Pi^{\leqslant}(p - p_1, t; p' - p_2, t'),\end{aligned}\quad (5.10)$$

where

$$\Pi^{\leqslant}(p, t; p', t') = 2 \int \frac{dp_1}{2\pi\hbar} \frac{dp_2}{2\pi\hbar} G^{\leqslant}(p_1, t; p_2, t') G^{\geqslant}(p_2 - p', t'; p_1 - p, t),\quad (5.11)$$

where $V(q)$ is the two-body potential with q being the relative momentum and the factor of 2 accounts for spin degeneracy.

While some previous attempts were made to include residual two-body interactions [121–123], the choice of the two-body potential $V(q)$ in those attempts might not have been optimal for the one-dimensional nuclear systems under consideration. Instead, to reflect the short-range nature of the residual nucleon-nucleon interactions and to mimic the effects of nucleon-nucleon scattering in the kinetic limit, we adopted a new form for the two-body potential:

$$V(q) = V_0 |q| \exp \left[- \left(\frac{\eta q}{2\hbar} \right)^2 \right],\quad (5.12)$$

where the values $V_0 = 205.491$ MeV and $\eta = 0.57$ fm have been chosen to establish a correspondence between the one-dimensional collision rates and the three-dimensional collision rates in symmetric nuclear matter in the semi-classical limit. Note that this potential yields no difference in the scattering between np and nn or pp pairs.

The residual interactions introduce an extra contribution termed E_{corr} to the total energy and thus effectively alter the equation of state. This issue arises, as we have fitted the nuclear matter in the mean-field approximation to the nuclear matter equation of states in the first place, before introducing two-body interactions. Furthermore, in principle, the interactions entering the Hartree-Fock self-energy Σ_{HF} and the residual self-energy Σ^{\leq} should be the same, which is beyond the naive separation of mean field dynamics and many-body dynamics employed in the current picture. Getting around the first issue, to get back to the previous satisfactory equation of state, we add an auxiliary parameterized contribution to the mean-field energy

$$\frac{E_{\text{aux}}}{A}(\rho, \delta) = A_1 \left(\frac{\rho}{\rho_0} \right)^{\tau_1} \exp \left(- b_1 \frac{\rho}{\rho_0} \right) + A_2 \left(\frac{\rho}{\rho_0} \right)^{\tau_2} \exp \left(- b_2 \frac{\rho}{\rho_0} \right) \delta^2, \quad (5.13)$$

and adjust parameters to reproduce the nuclear matter equation of state from the mean-field approximation in Eq. (5.9) as closely as possible. The parameter values are summarized in Table 5.1 and the results for the equation of state are illustrated in Fig. 5.2. The calculations are carried out for a uniform system enclosed in a box of size L , with $\Delta x = 0.57 \text{ fm}$ and periodic boundary condition.

A_1 [MeV]	τ_1 [MeV]	b_1	A_2 [MeV]	τ_2 [MeV]	b_2
39.33	1.157	1.192	-14.66	1.533	0.70

Table 5.1: Parameters for the auxiliary field in Eq. (5.13).

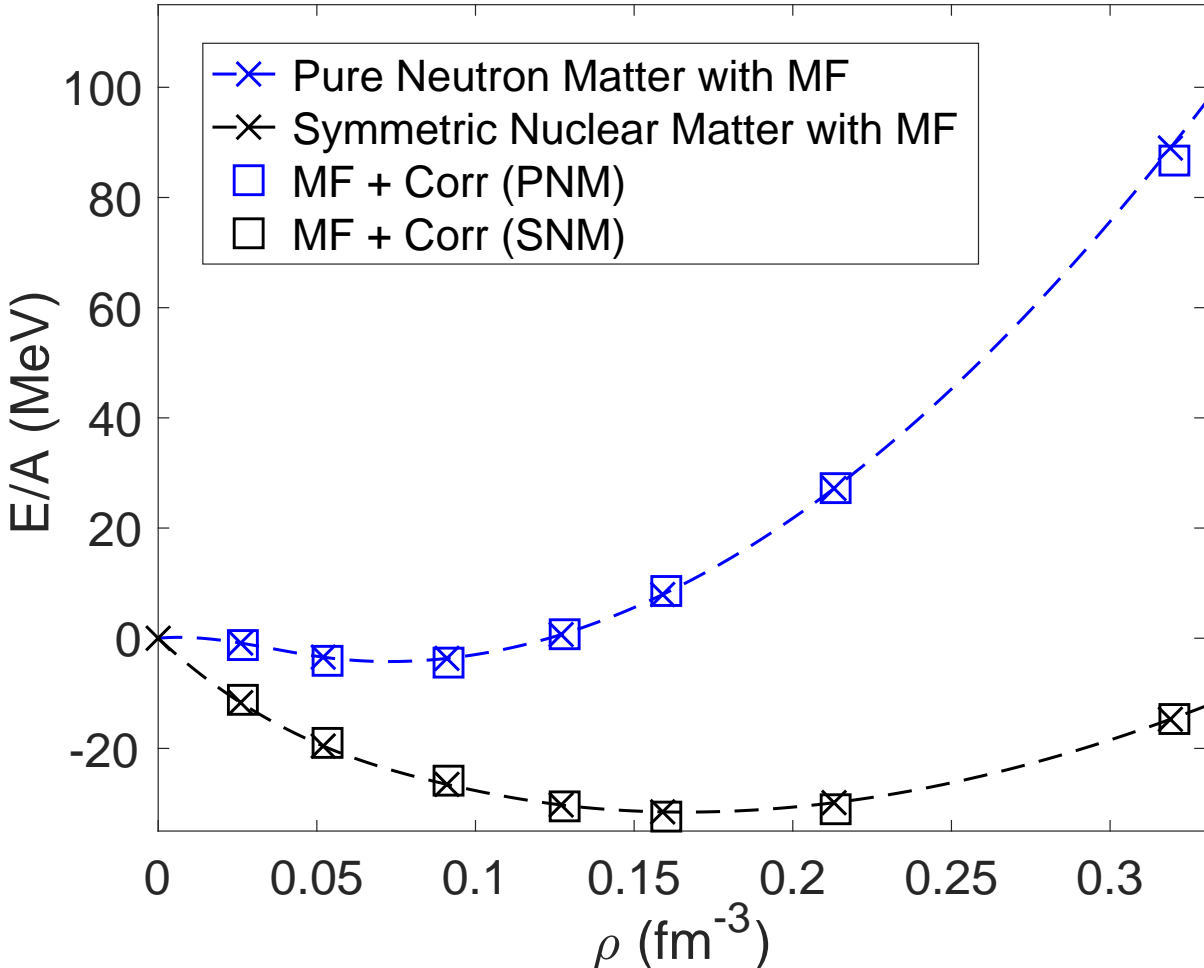


Figure 5.2: One-dimensional nuclear equation of state in the NGF approach. Crosses represent the results obtained within pure mean-field approximation. Dashed lines represent a cubic spline fit through the crosses. Open boxes show results obtained within complete calculations with correlations, where the pure mean-field results were matched by adjusting the parameters in the auxiliary field in Eq. (5.13).

To give context to the above results, it should be pointed out that the discretization interval Δx introduces a cut-off for particle momenta in the system, $p_{\max} = h/(2\Delta x)$. That cut-off limits the integration over

the momenta in the correlation self-energies, represented in Fig. 5.1, in addition to what the range parameter η does. Also the size L of the periodic box determines the spacing for the mesh in momentum, $\Delta p = h/L$, and this impacts both kinetic and correlation contributions to the energy. With this the auxiliary energy should have a dependence on Δx and L , $\frac{E_{\text{aux}}}{A} = \frac{E_{\text{aux}}}{A}(\rho, \delta, \Delta x, L)$. We treat Δx as a parameter of our dynamical model, resigned to the fact that to get to analogous dynamic results we might need to adjust some other parameters, such as V_0 or η in (5.12), when changing Δx . Here we choose $\Delta x = \eta$. As to the dependence on L , we have carried out a number of calculations at different values of L ranging from about 5 fm to 25 fm and different nucleon numbers corresponding to a wide range of density values of interest to us up to $2\rho_0$. In these calculations we see variation less than 1 MeV in E/A for uniform matter at fixed ρ , δ and Δx .

5.3 Preparing finite correlated nuclear systems

Following the extensions to accommodate the isospin degrees of freedom and two-body residual interactions and the study of the equation of state for infinite nuclear matter, we turn to the preparation of finite nuclear systems in one dimension. Obtaining a good approximation of the ground state is the starting point for performing simulations of nuclear collisions.

Within the full-fledged NGF approach, we continue to use adiabatic switching techniques [115, 121–124] to evolve the system towards an approximate ground state. At $t = 0$, the system is initialized in an uncorrelated harmonic oscillator ground state occupying the lowest $N/2$ neu-

tron shells and $Z/2$ proton shells. The remaining spin degeneracy $g = 2$ limits us to even-even nuclear systems. With the help of a switching function $f(t)$ varying smoothly from 0 to 1 over the switching period $[0, T_s]$, the total Hamiltonian $H(t)$ switches smoothly and slowly from the harmonic oscillator field H_{HO} to the nuclear field H_{nuc} according to $H(t) = [1 - f(t)] H_{\text{HO}} + f(t) H_{\text{nuc}}$. The nuclear Hamiltonian H_{nuc} contains both the mean-field component and the two-body interaction component. Since the second order diagrams in Fig. 5.1 contain effectively interactions at two times, some extra care needs to be taken when adiabatically turning on the residual self-energy Σ^{\leq} which gets transformed according to:

$$\Sigma^{\leq}(t, t') \rightarrow f(t) \Sigma^{\leq}(t, t') f(t'). \quad (5.14)$$

During the adiabatic switching process, the system evolves towards the nuclear ground state. The quality of the approximation to the ground state depends crucially on the switching time T_s , with a longer switching time yielding a better approximation. However, the entire preparation history enters the correlation integrals in Eq. (5.3) in every single time step in the subsequent evolution. Too long a switching time can stall the numerical calculations quickly as the burden of history to be remembered grows.

The effects of a cooling friction during switching have been studied previously [122, 125?]. Imposing an additional friction-like potential $U_{n/p}^{\text{fric}}$ in the switching period can to a certain extent relax the need of an excessively long switching time. The operational form that we employ for the potential is

$$U_{n/p}^{\text{fric}}(x, t) = f_0 \frac{\hbar}{\Delta t} \frac{\partial \rho_{n/p}(x, t)}{\partial t} \frac{t}{T_s} \exp \left[-\frac{t}{T_s} \right], \quad (5.15)$$

where f_0 is the strength of the friction and Δt is the time step size in the numerical simulations. While major desired dependencies have been factored out in Eq. (5.15), the strength parameter f_0 remains fragile, with optimal values varying from system to system and from conditions to conditions. In addition, even for optimal value any improvement in the switching with the inclusion of the cooling friction can be marginal. In practice, extending the switching time still easily outperforms any delicately designed switching functions or cooling frictions, when a high-quality ground state is in need. For the time being, we simply implement the cooling friction parametrized in Eq. (5.15) in the code with a relatively small strength $f_0 = 4 - 6 \text{ fm}^4/\text{c}$, without claiming the optimality of the choice.

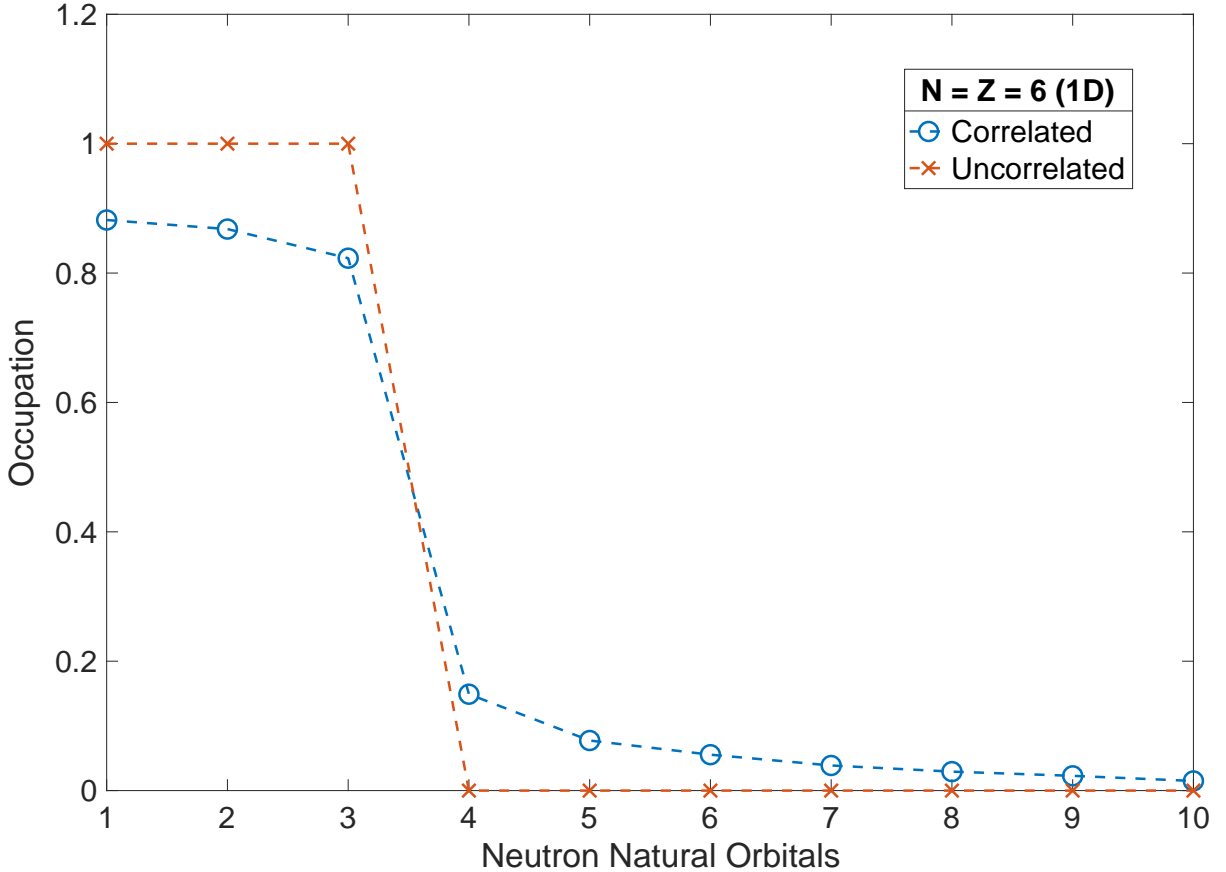


Figure 5.3: Occupation of the neutron natural orbitals. The open circles represent those of the correlated final state after the adiabatic evolution, and the crosses correspond to the uncorrelated initial state. The lines serve to guide the eye.

We now study the adiabatic evolution of a symmetric system with $N = Z = 6$. Initially, the system is comprised of 3 neutron shells and 3 proton shells in an external harmonic oscillator potential. The initial wave function can be written as an antisymmetrized product of the harmonic-oscillator single-particle states, and it is therefore an uncorrelated state. In Fig. 5.3, we denote the occupation of the neutron natural orbitals, found by diagonalizing the one-body neutron density matrix, with red crosses. In the uncorrelated system, the natural orbitals coincide with the eigenstates of the single-particle harmonic oscillator hamiltonian h_{HO} , and the lowest three are fully occupied as expected. The case for protons is exactly the same due to the isospin symmetry present in the system and thus is not shown here. If the mean field were the only interactions switched-on in the system during the adiabatic evolution, the dynamics would be identical to that in the TDHF theory. Indeed, the NGF approach with mean-field approximation has been studied previously [115, 121]. The final state would simply be uncorrelated, albeit as a product of complicated single-particle states. In the momentum basis $\{\phi_k \sim e^{ikx}\}$, however, even such an uncorrelated state becomes a complicated superposition of uncorrelated momentum states with all sorts of particle-hole excitations. While in terms of the complicated states the density matrix can be diagonal, the density matrix acquires off-diagonal elements in the momentum representation.

The second-order Born diagram in Fig. 5.1 allows for swapping of orbital pairs in an uncorrelated state due to the interaction and for mixing of that swapped state with the original, thus introducing a correlation impacting reinteraction. Depletion in the probability of staying in the same uncorrelated state is compensated with a probability of populating other

uncorrelated states. In a system with weak nonuniformity, the density matrix becomes nearly diagonal in the momentum representation. If the system is sparse or mixing is strongly suppressed by antisymmetrization, impact of a mixing persists over a long time. Eventually, a kinetic limit is reached where integrations in the residual self-energies can be carried out to arrive at energy-momentum conservation in a scattering process. The peculiarity of the conservation in the two-particle scattering in one dimension is that the orbitals only either retain or interchange momenta. For the species of the same type this leads to the persistence of the uncorrelated states, when composed out of near momentum eigenstates, and thus no apparent change compared to the mean-field dynamics. However, because of the self-consistency in the diagram in Fig. 5.1, the admixtures of states with swapped orbitals pile up over time, leading to correlations between more than two orbitals even when residual interactions act between two particles only. The scattering processes in the limit of energy-momentum conservation involve then more than two particles and more complicated changes occur in the uncorrelated states, potentially more similar to analogous processes in three dimensions than for the isolated two-particle scattering. Also, for a more nonuniform system the different orbitals may share the same momentum, so even if the momenta are retained or swapped the occupations of uncorrelated states may change. In Fig. 5.3 we observe a significant depletion of the occupation for the low-lying states and increased occupation for the higher, in spite of the one-dimensional peculiarity of the on-shell two-body scattering and of the two-body scattering rate being coarsely set to be the same as for the three dimensions. On the same note, even in three dimensions, when insisting

on a quasiparticle picture for a finite system with energy conservation for single-particle energies, the departure of occupations from 1 and 0 would never occur.

If a particle is removed from or placed in a natural orbital from a stationary system with weak correlations, the system largely remains in a stationary state. This can be quantified in terms of a spectral function with a unique single-particle energy, equal to the difference in the energies for the two stationary states. Inspired by Fermi liquid theory, this independent quasiparticle picture is pushed to the extreme in the semiclassical transport theory for nuclear reactions where specific energies are attributed to quasiparticles with definite momenta [66]. The spectral function naturally relates to NGF. One characteristic of increasing correlation strength is that identification of natural orbitals becomes a challenge. They may be always obtained by diagonalizing the density matrix but, as far as evolution of NGF in the relative time is concerned, the orbitals can be discussed only in a perturbative context. The spectral function is not diagonal in any orbitals anymore, but can be near-diagonal and/or diagonal elements of the spectral function can be considered.

Given the above, in the correlated system we look at diagonal elements of the spectral function in momentum representation. For particular species with particular spin projection, denoted with ν (also specifically used for neutrons in the shell-model notation), the spectral function $S_\nu(p, E)$ is related to the retarded Green's function $G_\nu^+(p, E)$ with

$$S_\nu(p, E) = -\frac{1}{\pi} \text{Im} G_\nu^+(p, E). \quad (5.16)$$

The retarded Green's function $G_\nu^+(p, E)$ admits a Lehmann representation,

$$G_\nu^+(p, E) = \sum_p \frac{|\langle \Psi_p^{(N+1)} | \phi_\nu^\dagger(p) | \Psi_0^{(N)} \rangle|^2}{E - (E_p^{(N+1)} - E_0^{(N)}) + i\eta} + \sum_h \frac{|\langle \Psi_h^{(N-1)} | \phi_\nu(p) | \Psi_0^{(N)} \rangle|^2}{E - (E_h^{(N-1)} - E_0^{(N)}) + i\eta}, \quad (5.17)$$

where $\eta \rightarrow 0^+$, ϕ and ϕ^\dagger are annihilation and creation operators in momentum representation respectively, $\Psi_p^{(N+1)}$ are eigenstates of the total Hamiltonian with $N+1$ neutrons and $\Psi_h^{(N-1)}$ are eigenstates with $N-1$ neutrons. The spectral function $S_\nu(p, E)$ picks out the poles of retarded Green's function, which are the excitation energies of adding or removing a neutron of momentum p with respect to the N -neutron ground state Ψ_0 . The strength of the excitation is regulated by the overlap function in the numerators in the retarded Green's function. On account of the completeness of the sets of states and commutation relation for the operators, the spectral function integrates over energy to 1. This allows one to interpret $S_\nu(p, E)$ as the probability density for a particle ν with momentum p to have an energy E [126].

In a noninteracting Fermi gas the spectral function peaks at the kinetic energy of a particle with momentum p , i.e. $S(p, E) = \delta[E - p^2/(2m)]$. For a self-bound slab in a box, in the semiclassical limit behind the transport for reactions, two such peaks are expected, one at lower energy for slab interior and one at higher for the exterior, with relative intensity of the peaks representing the relative share of the size of the box for the slab interior and exterior. In the Fermi liquid theory the spectral function of a correlated uniform system is often sought in the Lorentzian form: $S(p, E) \approx \frac{Z_p/(2\tau_p)}{(E-E_p)^2+[1/(2\tau_p)]^2} + S'(p, E)$, where E_p is the energy of the quasiparticle with momentum p , τ_p is the lifetime, Z_p is quasiparticle strength

and S' is contribution of incoherent background that ensures that the sum rule is satisfied [126].

In Fig. 5.4, we show the spectral functions for neutrons in a symmetric system with $N = Z = 6$ in an $L = 15 \text{ fm}$ box, at six of the discrete momenta, in the mean-field calculation and in the full calculation with two-body residual interaction. The spectral functions are obtained by evolving the system over $300 \text{ fm}/c$ and Fourier transforming the relative time difference $t_1 - t_2$ of the Green's functions. For reference, we provide in the figure the location where the kinetic energy for a given momentum is. Multiple spikes are present in both calculations. For three of the lower momenta, strength is present at about 55 MeV down from the free-space kinetic energy, about the depth of the potential well in nuclear systems. The spikes in the mean-field case are sharper, and, for the three lowest momenta, a few of the peaks in the two different cases overlap almost perfectly, suggesting that the mean field alone is already responsible for a significant part of the fragmentation of natural orbitals in momentum representation. Notably in the limit of perfectly static infinite-time evolution, the mean-field peaks would turn into δ -functions, meaning that any width observed for these peaks in Fig. 5.4 is due to our time domain methodology. Inclusion of residual interactions smoothes out and spreads the peaks and moves some well beyond any resolution impact of our methodology.

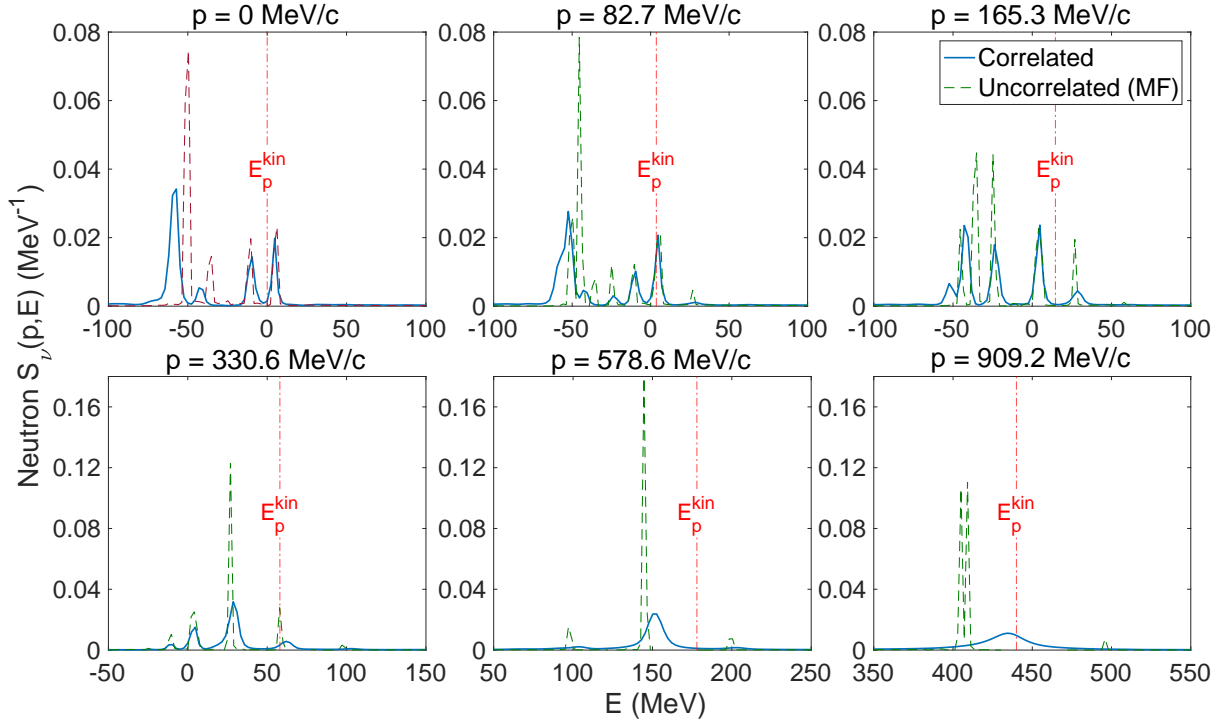


Figure 5.4: Neutron spectral functions vs energy for an $N = Z = 6$ self-bound system in an $L = 15$ fm box at discretized momenta. The red dashed-dot line indicates the kinetic energy of a free neutron with momentum p . See the text for discussion.

The structures observed in Fig. 5.4 are outside of the reach of semiclassical transport theory. Telling is the fact that to resolve the structures in the spectral function reasonably well, we had to evolve the system for over 300 fm/ c . Key stages of reactions to which transport is applied commonly last a twentieth of that time [66, 114], meaning that energy structure will generally be poorly resolved and conservation in binary collisions will not hold [127].

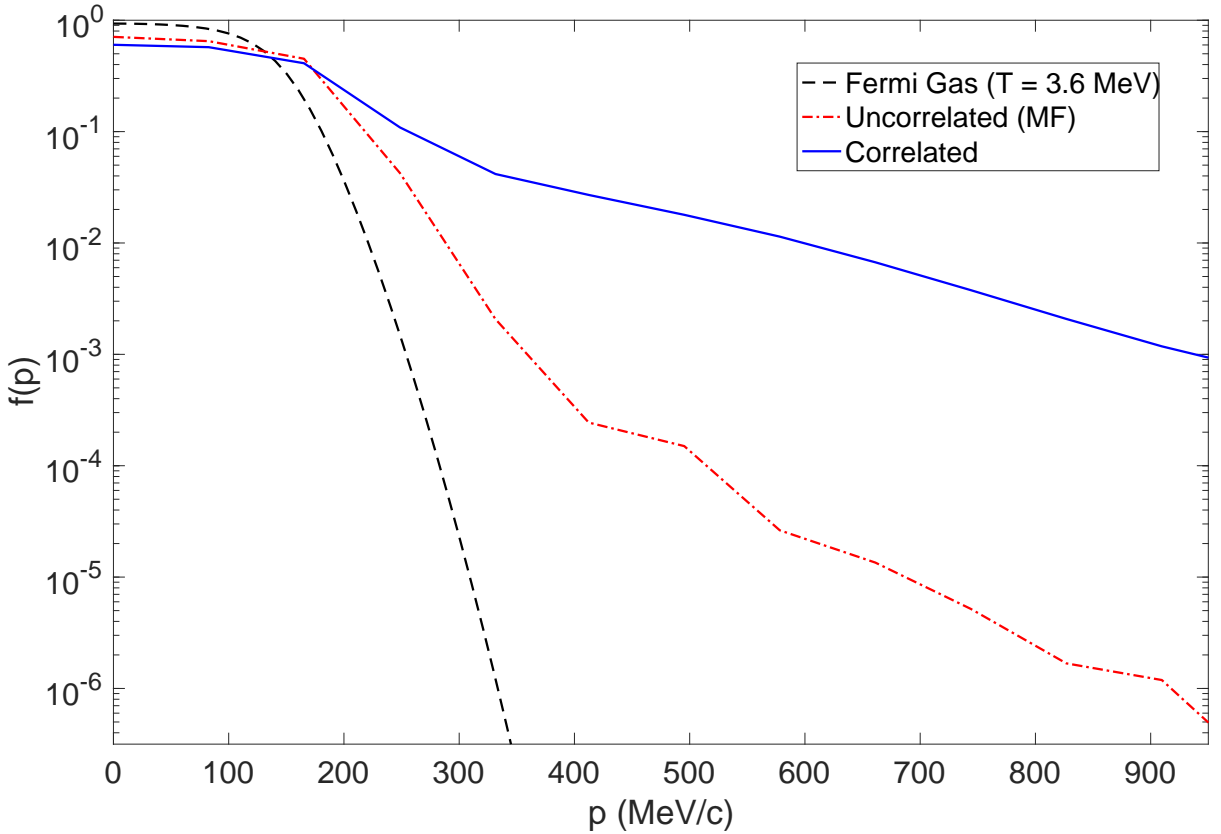


Figure 5.5: Momentum state occupation for neutrons in the same $N = Z = 6$ ground-state system as in the preceding two figures and for a Fermi gas. The dashed, dash-dotted and solid lines represent the Fermi gas at temperature $T = 3.6$ MeV, the mean field system and the correlated system, respectively.

In Fig. 5.5, we show the momentum distribution for neutrons in the same $N = Z = 6$ system we have been discussing and for a noninteracting Fermi gas at temperature $T = 3.6$ MeV. The high-momentum tails seen in the uncorrelated mean-field case and the case with short-range two-body interaction lack the features of a free Fermi gas at finite temperature, suggesting again that the underlying picture cannot be entirely captured in the Fermi liquid theory. In particular, the high-momentum ($> p_F^{1D} \approx 195$ MeV/c) tail accounts for about 25% of the neutrons in the correlated system, comparable to what is reported to be around 20% in nuclei in nature [128–130], while the corresponding proportion in the uncorrelated

system is just about 10%. A significant number of the high-momentum nucleons are present due to the short-range two-body interaction.

5.4 Exploring dissipation with isovector oscillation in a finite system

To describe heavy-ion collisions at the intermediate energies ranging from tens of to hundreds of MeV/u, it is important to include dissipation of the relative energy in the center of mass frame in the dynamics, which is lacking in the conventional TDHF theory. However, as discussed in the preceding section, effects of the short-range two-body interactions included in the correlation integrals in the NGF approach can be interpreted as scattering and rearranging population of orbitals. In fact, these integrals turn into collision integrals in the kinetic limit for the theory.

To explore the dissipative effects introduced by the short-range two-body interactions in the NGF approach, we simulate the isovector-like oscillation of neutrons and protons in a finite system. The simulations are performed in two different settings, one with only mean field dynamics, which is equivalent to the case in TDHF theory, and the other with both mean field dynamics and residual two-body interactions. For each setting, we prepare a symmetric nuclear system with $N = Z = 4$ in its ground state at the center of a box, employing the adiabatic switching technique discussed before. The time is reset to $t = 0$ fm/c after completion of the adiabatic evolution. At $t = 0$ fm/c, we then perturb the neutron slab and the proton slab, which have been overlapping with each other perfectly. Specifically, we apply opposite jolts to the neutron and proton slabs, that

take the form of Galilean boosts to the same-time lesser Green's functions $G_{n/p}^<$ at $t = 0$:

$$G_{n/p}^{\leqslant, \text{after}}(x, 0; x', 0) = \exp\left(\pm i \frac{Px}{\hbar}\right) \\ \times G_{n/p}^{\leqslant, \text{before}}(x, 0; x', 0) \exp\left(\mp i \frac{Px'}{\hbar}\right), \quad (5.18)$$

where P is the small momentum boost of the order of $55 \text{ MeV}/c$, equivalent to 1.6 MeV in kinetic energy per nucleon. After the jolts, the neutron and proton center of mass start to move away from one another, but as particles reach the edge of their optical potentials, they retreat and the centers of mass move back. Fig. 5.6 shows the evolution of the density profiles for neutrons and protons for the setting with mean field only. The position of the center of mass for the neutron slab \bar{X} can be seen, for both scenarios, in the top panel of Fig. 5.7. When the residual interaction is present, the isovector oscillation is much more strongly damped.

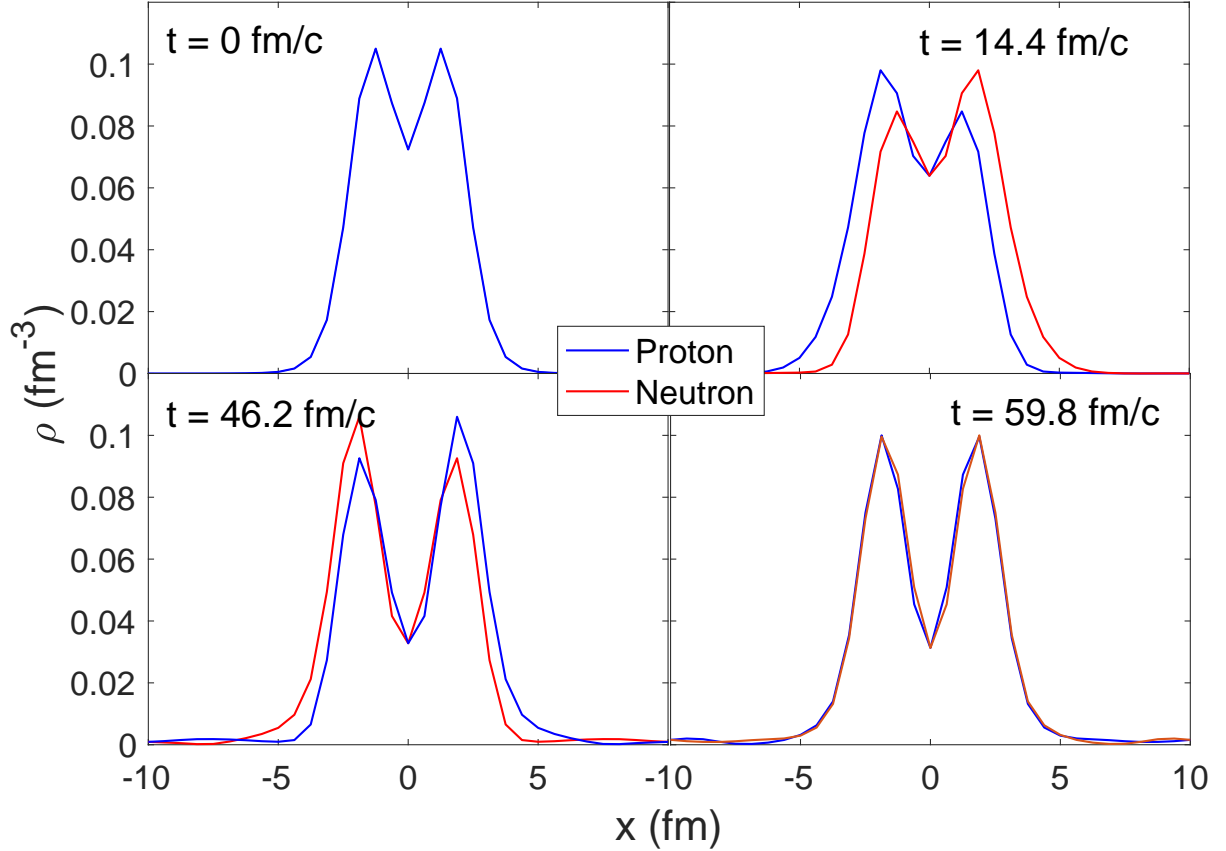


Figure 5.6: Isovector-like oscillation of the neutron slab and the proton slab with mean-field approximation. The red line represents the neutron density profile and the blue line represents the proton density profile.

On top of the isovector oscillation in Fig. 5.6, one may observe there deformations of the neutron slab and the proton slab with respect to their own center of mass. Since the slabs are not rigid, it is conceivable that one induces other forms of oscillation. The additional changes may progress at the same or multiple of the isovector frequency, or at a completely different frequency. For more insight we evaluate two more moments for a neutron slab and plot them as a function of time in the lower two panels of Fig. 5.7. Specifically, the center panel displays the second moment about the center of mass of the neutron slab, $\langle (X - \bar{X})^2 \rangle^{\frac{1}{2}}$, describing the breathing mode for the neutron slab and also for the whole system after the isovector mode

dies down. Finally, the bottom panel displays the third moment about the center of mass of the neutron slab, $\langle(X - \bar{X})^3\rangle_{\nu}^{\frac{1}{3}}$, representing skeweness of the slab around the center of mass.

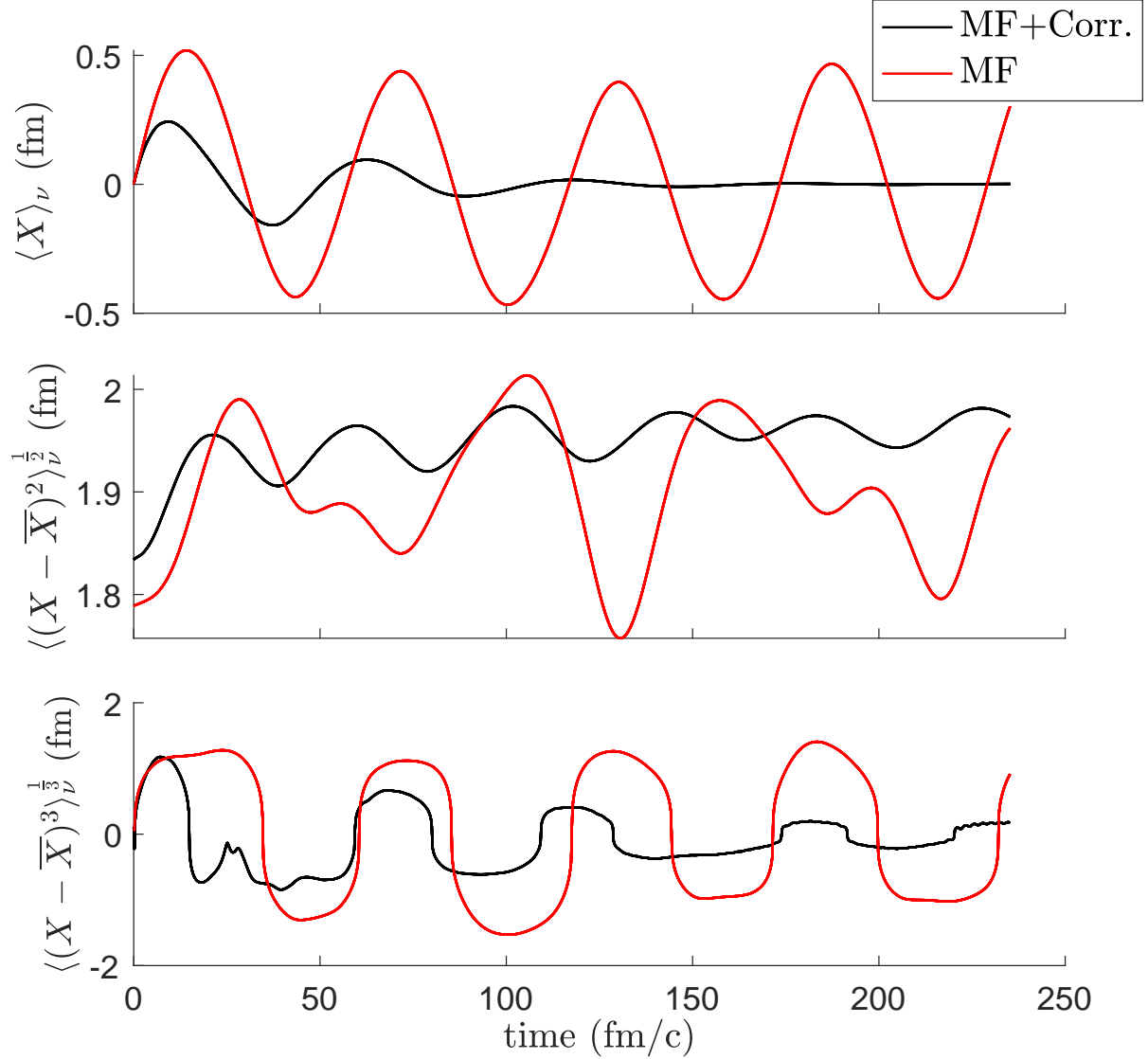


Figure 5.7: Evolution of the lowest three moments of the neutron slab. The red lines and the black lines correspond to calculations with mean field only and the full calculations, respectively.

The higher moments, quantifying behavior of the farther-out features of the density distribution, reach higher values in Fig. 5.7 than does the center of mass position. No matter what moment is considered the damping of its oscillations is much stronger for the dynamics with correlations than

without. In fact within the considered time interval hardly any damping is observed for the pure mean-field dynamics. While the oscillations in the center of mass are fairly sinusoidal, indicating the dominance of a single frequency, this is less so for the higher moments. The oscillations in the third moment are in phase with those in the first, but are definitely anharmonic, suggesting that initialization of the Green's functions, with the same boost parameter at low densities as at high, might be too naive. The second moments exhibit different periodicity than the odd moments, suggesting that an isoscalar breathing mode got excited and progresses at a different frequency than isovector. Both the third and second moment damp away at a slower rate than the first moment, when the correlations are present. In the case of the third moment, the difference in damping compared to the first moment is subtle and can be due to the fact that the correlations weaken at the low densities that get tested by the high moment. In the case of the second moment the damping is weak at longer time and we suspect that this is due to the peculiar nature of two-body scattering in the semiclassical limit in one dimension, where the orbitals either persist or interchange. The interchange will shuffle the momentum between neutron and proton slabs, damping the isovector mode, but do nothing to the isoscalar mode once the isovector mode dies out. The glitch in the third moment occurring at $25 - 30$ fm/c is likely due to ripples in the density tails, produced by the boost, coming from both sides and colliding at the boundary of the periodic box. Some early time transient behavior in the correlated dynamics is also due to the fact that the jolts are taken to be of a short duration compared to the relaxation of correlations.

5.5 Galilean Covariance

The Kadanoff-Baym equations transform covariantly under Galilean transformation of the reference frame. That means that Galilean transformed solutions from one frame should remain solutions of the equations in another frame. Obviously there is no guarantee that this remains true in a numerical solution. Discretization in space introduces a cut-off in momentum space that does not transform covariantly. Practical violations of the covariance may impair studies of moving matter whether in collective oscillations or in collisions. In the context of the latter, we need to prepare slabs in their ground state, boost them and direct against each other. Due to violation of covariance, the boost can potentially excite the slab and lead to its break-up ahead of any collision.

In this section, we explore impact of a boost on a slab in practice. In the calculation we use a box of size $L = 15\text{ fm}$ with periodic boundary conditions. We prepare a symmetric system with $N = Z = 2$ at the center of the box as usual. We then boost the slab to provide it with a momentum per nucleon P . When working with a periodic box, the momenta in representing the Green's functions are discretized with the spacing of $\Delta p = h/L$. We simplify the boost by taking $P = 2\Delta p$, or wavevector $k = 2(2\pi/L) \simeq 0.838\text{ fm}^{-1}$, corresponding to boost velocity $V = P/m = 0.176c$. With this the Green's functions can be shifted over momentum mesh without interpolations.

The correlation integrals in the Kadanoff-Baym equation involve the integration of the entire history of the system, rendering the dynamics non-Markovian, in sharp contrast to both semi-classical transport theories

and the TDHF theory. If the boost were applied to the end of the adiabatic evolution, we would be boosting the single-particle characteristics, but not two-particle correlations. We can afford it to a degree when exciting isovector oscillations, risking some heating of the system in addition to that occurring anyway due to dissipation of the collective oscillation. The local Galilean boost operator $\mathcal{T}(x, t; V)$, that transforms a Green's function from a frame of a still system with positions in terms of coordinate x to one in terms of $x' = x + Vt$, according to

$$G_{\text{moving}}^{\lessgtr}(x'_1, t_1; x'_2, t_2) = \mathcal{T}(x_1, t_1; V) G_{\text{still}}^{\lessgtr}(x_1, t_1; x_2, t_2) \times \mathcal{T}^*(x_2, t_2; V), \quad (5.19)$$

is

$$\mathcal{T}(x, t; V) = \exp \left[\frac{iP}{\hbar} (x + Vt/2) \right]. \quad (5.20)$$

In momentum representation this yields

$$G_{\text{moving}}^{\lessgtr}(p_1, t_1; p_2, t_2) = e^{-\frac{iVt_1}{\hbar}(p_1 - P/2)} G_{\text{still}}^{\lessgtr}(p_1 - P, t_1; p_2 - P, t_2) \times e^{\frac{iVt_2}{\hbar}(p_2 - P/2)}. \quad (5.21)$$

When starting investigation of a boosted slab at $t_0 = 0$, the transformation is applied to functions where one of the arguments coincides with t_0 and the other either coincides with or precedes t_0 .

After applying the boost transformation in momentum, we evolve the system according to the Kadanoff-Baym equations in the standard manner. The evolution of the density profile for a boosted slab is illustrated in Fig. 5.8. Specifically in panel (a) we show the initial profile with a dash-dot line. In the subsequent panels (b)-(d), we subsequently advance the evolution by 30 fm/c in each, displaying the latest profile with a solid line

and intermediate profiles, at $15 \text{ fm}/c$ intervals, with dashed lines. It is apparent that the slab moves at a uniform pace. Some small variations in the profile are seen, potentially related to spatial discretization, but these are not significant enough to be of concern in exploring slab collisions. With this, we demonstrate covariance of the NGF approach adequate enough for future studies of the collisions.

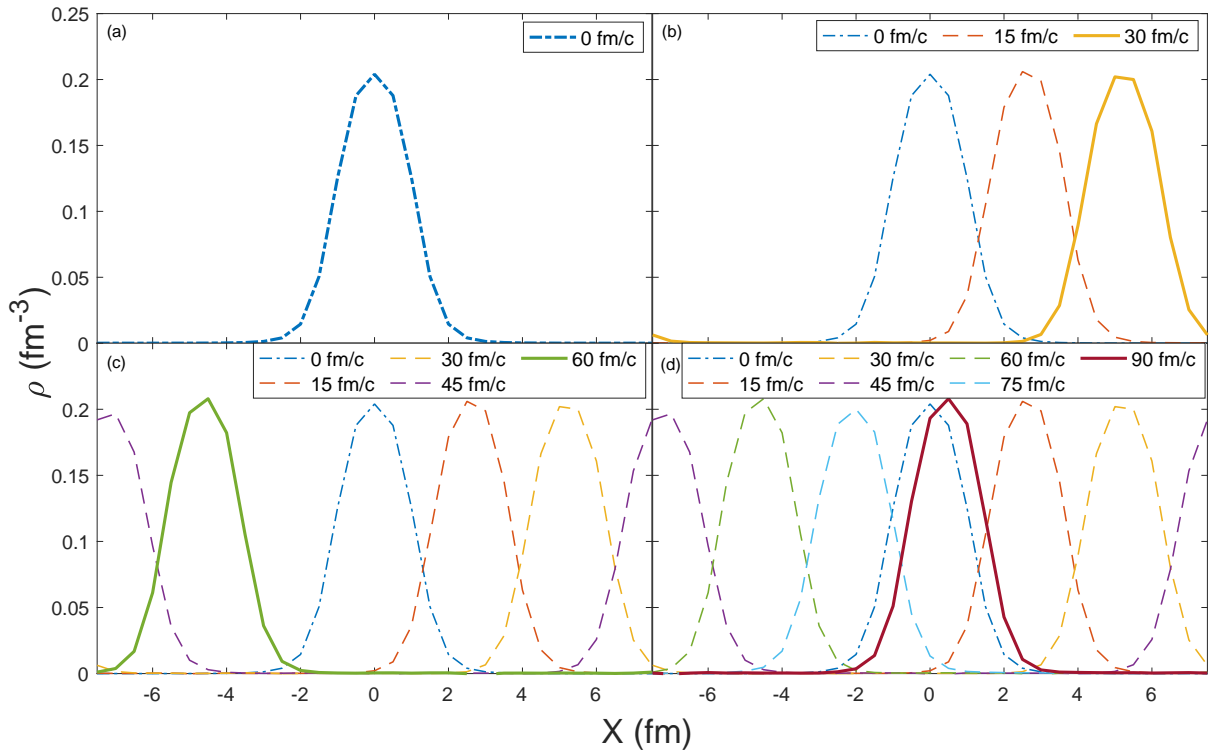


Figure 5.8: Evolution of density for a correlated $N = Z = 2$ slab boosted with velocity $V = 0.176 c$. The initial density is illustrated with a dash-dotted line in every panel. The panels (b)-(d) show evolution advanced subsequently over $30 \text{ fm}/c$, with the latest profile illustrated with a solid line. Intermediate profiles at every $15 \text{ fm}/c$ are illustrated with dashed lines.

5.6 Summary and future prospects

In this chapter, we have discussed the application of the NGF theory to the description of the dynamics of one-dimensional correlated nuclear sys-

tems in different scenarios. The preparation of finite nuclear systems is relevant for the initialization of projectile and target in simulating nuclear collisions. The dissipation arising from the short-range two-body interactions, demonstrated in the isovector-like slab oscillation, can give rise to the stopping effects in collisions. One should bear in mind that the dissipation in one dimension simulated in the current numerical model may not have captured the entirety of the actual dissipation in three dimensions. In a three-dimensional description, relative longitudinal momentum can be effectively redirected into the transverse directions, presumably enhancing the dissipation. In the current one-dimensional description, dissipation effects are still largely confined to the internal excitation of the systems in terms of exchanging momentum. The translation of a stable slab partially mimics the situation of two nuclei approaching each other before making contact, but we do acknowledge that boosting two stable slabs in the opposite directions requires more careful design and is thus out of the scope of this paper.

We shall also briefly touch on the limitations and possible future extensions of the current NGF model. The tremendous amount of CPU hours and memories needed to solve the Kadanoff-Baym equation numerically renders direct simulations in higher dimension computationally infeasible. In fact, even in the current model, we needed to look for techniques to reduce the computational cost and the calculations have only been possible on high-performance computer clusters. We have used OpenMP [131] to parallelize the code so that independent loop iterations can be carried out simultaneously on multiple cores. We also made the observation that, at any given moment t , in propagating the Green's functions $G^<(\cdot, t', \cdot, t)$

and $G^>(\cdot, t, \cdot, t')$ with $t \geq t'$, only the history correlated with the current is relevant, i.e., quantities with time arguments (t, t') or (t', t) . This allows for the use of arrays with just one dimension in time for t' , which can be overwritten during the propagation of t , in sharp contrast to the naive way of storing quantities in both of the temporal dimensions. The optimization made so far makes no compromise on the exactness of the numerical solutions in the stated framework. Further reduction in time or memory is possible under the assumption that elements far off the diagonal are negligible. In fact, in Ref. [115] it was demonstrated that far off-diagonal spatial elements of Green's functions may be dropped with impunity and one may hope to be able to introduce a finite memory time limiting extent in time. These could reduce the time and memory cost of computations.

Regarding extension of the scope, the current separate parametrizations of mean field and residual interactions represents some limitation. Progress towards consistency between the interactions could be reached by solving the T -matrix equation [118] with an interaction more representative of a bare interaction. With a separable approximation to the latter, the computational effort would not be much more serious than the current. At low energies, excitations of chaotic collective modes can compete with nucleon-nucleon collisions in equilibrating larger colliding systems. Accounting for such excitations can be achieved with a ring approximation to the self energy, again requiring quite similar computational effort to the current. Beyond the short-range correlations, extensions can be conjectured to the current NGF model to treat pairing correlations upon differentiation of the spin degrees of freedom. Paring effects have been incorporated into collisions in a three-dimensional TDHF code through the

initialization of Bardeen-Cooper-Schrieffer (BCS) ground states [104], with the caveat that the paring amplitudes are kept fixed during the evolution. A more proper way to treat paring correlations in time-dependent processes is to solve the TDHF-Bogoliubov (TDHFB) equation [27, 102, 103]. It is unclear how paring can enter the current picture of the NFG theory. Still, following the footprints of the TDHFB theory, one may try including a time-diagonal paring-Green's functions of the form $\langle \phi(x_1, t) \phi(x_2, t) \rangle$, analogous to the abnormal density or the pairing tensor $\kappa(t)$ in the TDHFB theory. A paring term Δ shall enter the Hamiltonian when the Kadanoff-Baym equations for the normal Green's functions are solved. An additional equation for the time-diagonal paring-Green's functions void of the short-range interactions, mimicking that for the paring tensor [103], also needs to be solved simultaneously. Within such a naive conjecture, violation of total particle number and total energy might arise though.

In the end, we conclude that this work extends the application of the NFG theory in nuclear physics beyond the mean field approximation and lays the ground for the future study of nuclear collisions, taking us one step closer to a fully quantum-mechanical and realistic transport model. A multitude of extensions and optimization can also be considered and implemented for the improvement of this model.

Chapter 6

Conclusion

In this thesis, we presented two time-dependent transport models for HIC, which represent the two major directions for future developments of transport theory. The one-body Langevin transport model incorporates fluctuations to take into account the effects of many-body correlations and attempts to address fragmentation in HIC at intermediate energies; the NGF transport model treats nuclear collisions in a fully quantum-mechanical and self-consistent manner, capable of describing both the mean-field dynamics and the short-range two-body correlations.

In Chapter 2, we described how we had arrived at a purely one-body transport model based on Langevin dynamics starting from the conventional BUU equation. The formulation of the new model was discussed at length and the technicalities in the numerical implementation, including a self-consistent method to solve the Thomas-Fermi equation for the initialization of stable nuclei, were carefully documented.

In Chapter 3, we presented a series of benchmark results to demonstrate the reliability and compatibility of the one-body Langevin transport model. We first simulated the Au + Au collisions at two incident energies, 100 MeV/nucl and 400 MeV/nucl, at an impact parameter of 7 fm.

We compared the rapidity distributions dN/dy , the average in-plane flow $\langle p_x/A \rangle$ and the flow parameter $d\langle p_x/A \rangle/dy_{\text{red}}$ and found good agreement with other existing transport codes at both incident energies under the same controlled conditions. We also investigated the nearly central collision Sn + Sn at 50 MeV/nucl, where our model was again shown to be robust in describing the fragmentation dynamics involved. Results were compared with two other mature models, SMF and AMD. Despite the drastic differences in their treatment of stochastic dynamics, all models yield similar distributions for the primary IMF multiplicity.

In Chapter 4, we investigated the so-called “hierarchy effect” in the correlation between charge and velocity of PLFs reported in experiment. The collision of focus was Ta+Au at 39.6 MeV/nucl. By analyzing the properties of the primary PLFs generated in the simulation with the Brownian motion model, we confirmed that the PLF with the greatest charge tends to have the greatest velocity component and be forward-peaked, and the existence of a weak positive correlation between charge and velocity. These observation contrast the idea of IMF being emitted from an equilibrated source, and can only be interpreted with a dynamical transport model, such as the one presented in this thesis. We also simulated U+C at 24 MeV/nucl and could not predict any relevant fragmentation phenomenon, due to the model’s inability of describing statistical decay. This, however, does not contradict the *lack* of “hierarch effect” reported for the same system in experiment.

In Chapter 5, we first presented a quantum-mechanical transport model based on NGF, and, in particular, showed how short-range two-body correlations were naturally included in the full-fledged Kadanoff-Baym equa-

tion. The EoS $E/A(\rho)$ of correlated nuclear matter in one dimension was calculated. We demonstrated the correlation effects by comparing natural orbital occupancy n , spectral functions $S(p, E)$ as well as the momentum distribution $f(p)$ of nuclear systems in 1D, with or without two-body correlation. The dissipative effects brought by two-body correlation was evidenced by simulation of the damping of spatial multipole moments $\langle(X - \bar{X})^n\rangle^{\frac{1}{n}}$ of 1D nuclear systems. In the end, we also verified that the simulation preserved the Galilean covariance, which paved the way for future study of collision of 1D slabs.

Lastly, the work in this thesis represents just a very narrow niche of the development of transport theories in the broad study of HIC physics, and certain aspects of the transport models discussed here may come across as ad hoc and/or primitive. It is, nonetheless, hoped that this record of work could shed some light on the muddy issues of the incorporation of fluctuations and quantum effects into transport models, and be a potential source of inspiration for any future development.

Appendix A

Fokker-Planck equation and Langevin equation

In this appendix, we provide a summary of the derivation of the Fokker-Planck equation detailed in Ref. [80] and discuss the corresponding Langevin equations of different forms.

Consider the following Boltzmann collision integral for arbitrary statistics,

$$I_{\text{coll}} = \frac{g}{h^3} \int d^3 p_b \int d\Omega \frac{d\sigma_{ab}}{d\Omega} v_{ab} [\tilde{f}_a \tilde{f}_b f_{a'} f_{b'} - f_a f_b \tilde{f}_{a'} \tilde{f}_{b'}]. \quad (\text{A.1})$$

f_x is to be regarded as the shorthand notation for the one-body phase distribution function $f(\mathbf{p}_x)$. $\tilde{f} = 1 + \lambda f$ with $\lambda = -1, 0, 1$ corresponding to Fermi-Dirac, Boltzmann, and Bose-Einstein statistics. g is the degeneracy factor.

For a pair of particles with momenta \mathbf{p}_a and \mathbf{p}_b , v_{ab} is the relative velocity, and $d\sigma_{ab}/d\Omega$ is the differential cross section, where the scattering angle Ω is defined in the center-of-mass frame of the pair. Final momenta are denoted by *primed* subscripts.

In the center-of-mass frame, the initial state of the colliding pair is characterized by the relative momentum $\mathbf{q}_{ab} = \mathbf{p}_a - \mathbf{p}_b$ and the total momentum

$\mathbf{P}_{ab} = \mathbf{p}_a + \mathbf{p}_b$. When only elastic collisions are under consideration, \mathbf{P}_{ab} remains constant and $q_{a'b'} = q_{ab}$. It follows that the final relative momentum $\mathbf{q}_{a'b'}$ is completely determined by the scattering angle $\Omega = (\theta, \phi)$.

For a ϕ -independent and forward-peaked cross section, we can first make the following expansion over the polar angle θ at a fixed azimuthal angle ϕ , and then truncate it up to the leading order term upon integration over ϕ ,

$$\begin{aligned} \tilde{f}_a \tilde{f}_b f_{a'} f_{b'} - f_a f_b \tilde{f}_{a'} \tilde{f}_{b'} &= \tilde{f}_a \tilde{f}_b \left[\sum_{n=0}^{\infty} \frac{\theta^n}{n!} \frac{\partial^n}{\partial \theta^n} (f_a f_b) \right] \Big|_{\theta=0} \\ &\quad - f_a f_b \left[\sum_{n=0}^{\infty} \frac{\theta^n}{n!} \frac{\partial^n}{\partial \theta^n} (\tilde{f}_a \tilde{f}_b) \right] \Big|_{\theta=0}. \end{aligned} \quad (\text{A.2})$$

The zero-order term vanishes conveniently. Since

$$\mathbf{q}_{a'b'} = q_{ab}(\sin \theta \cos \phi, \sin \theta \sin \phi, \cos \theta), \quad (\text{A.3})$$

the usual chain rule gives

$$\frac{\partial}{\partial \theta} = \sum_i \frac{\partial q_{a'b'}^i}{\partial \theta} \Big|_{\theta=0} \frac{\partial}{\partial q_{a'b'}^i}, \quad (\text{A.4})$$

where $\partial \mathbf{q}_{a'b'}/\partial \theta|_{\theta=0} = q_{ab}(\cos \phi, \sin \phi, 0)$. The integration of $\partial \mathbf{q}_{a'b'}/\partial \theta|_{\theta=0}$ over ϕ is zero, so the leading order term in Eq. (A.2) is of second order.

It is easy to show that

$$\int_0^{2\pi} d\phi \frac{\partial^2}{\partial \theta^2} \Big|_{\theta=0} = \pi \left(-2 \sum_i q^i \frac{\partial}{\partial q^i} + q^2 \sum_{ij} \Delta^{ij} \frac{\partial^2}{\partial q^i \partial q^j} \right), \quad (\text{A.5})$$

where the subscript ab for q is suppressed for brevity and $\Delta^{ij} = \delta^{ij} - q^i q^j / q^2$ is a projection operator onto the plane perpendicular to \mathbf{q}_{ab} .

Upon inserting the truncated expansion integrated over ϕ into the Boltzmann collision integral Eq. (A.1) and noting that $\partial/\partial q_{ab}^i = \frac{1}{2}(\partial/\partial p_a^i - \partial/\partial p_b^i)$, one will arrive at the following Fokker-Planck equation,

$$\frac{\partial f_a}{\partial t} = -\nabla_{\mathbf{p}_a} \cdot \left[\frac{1}{2} \left(\tilde{\mathbf{R}}_a + \tilde{f}_a \mathbf{R}_a \right) f_a \right] + \nabla_{\mathbf{p}_a}^2 \left(\mathbf{D}_a f_a \right), \quad (\text{A.6})$$

where

$$R_a^i = -\frac{g}{h^3} \int d^3 p_b f_b F_{ab} q_{ab}^i, \quad (\text{A.7})$$

$$\tilde{R}_a^i = -\frac{g}{h^3} \int d^3 p_b f_b \tilde{f}_b F_{ab} q_{ab}^i, \quad (\text{A.8})$$

$$D_a^{ij} = \frac{g}{4h^3} \int d^3 p_b f_b \tilde{f}_b F_{ab} (q_{ab}^2 \delta^{ij} - q_{ab}^i q_{ab}^j), \quad (\text{A.9})$$

and

$$F_{ab} = (\pi v_{ab}/2) \int_0^1 \theta^2 (d\sigma_{ab}/d\Omega) d\cos\theta. \quad (\text{A.10})$$

By assuming that the evolution of particle momentum \mathbf{p} is a Gaussian random process and that the evolution of the momentum distribution $f(\mathbf{p}, t)$ follows the Fokker-Planck Eq. (A.6), one can write down the corresponding single-particle Langevin equation of the *Itô* form[132, 133],

$$d\mathbf{p} = \frac{1}{2} \left(\tilde{\mathbf{R}} + \tilde{f} \mathbf{R} \right) dt + \boldsymbol{\sigma} dB_t, \quad (\text{A.11})$$

where $\boldsymbol{\sigma}$ is a 3×3 positive definite matrix such that

$$D^{ij} = \frac{1}{2} \sum_k \sigma_{ik} \sigma_{jk}. \quad (\text{A.12})$$

\mathbf{B}_t denotes a Guassian random process with properties

$$\langle dB_t \rangle = \mathbf{0}, \quad (\text{A.13})$$

$$\langle dB_t^i dB_t^j \rangle = dt \delta_{ij}. \quad (\text{A.14})$$

Here and in what follows, some subscripts may be dropped whenever no confusion arises.

When the cross section $d\sigma_{ab}/d\Omega$ is taken to be independent of q_{ab} , one can verify that $\nabla_{\mathbf{p}_a} \cdot \mathbf{D} = \frac{1}{2} \tilde{\mathbf{R}}$. Hence, the Fokker-Planck Eq. (A.6) has then an equivalent simplified form,

$$\frac{\partial f}{\partial t} = -\nabla_{\mathbf{p}} \cdot \left(\frac{1}{2} \tilde{f} \mathbf{R} f \right) + \nabla_{\mathbf{p}} \cdot (\mathbf{D} \nabla_{\mathbf{p}} f). \quad (\text{A.15})$$

This form of the Fokker-Planck Eq. (A.15) has the corresponding Langevin equation of the *Stranovich* form[132, 133],

$$d\mathbf{p} = \frac{1}{2}\tilde{f}\mathbf{R}dt + \boldsymbol{\sigma} \circ d\mathbf{B}_t. \quad (\text{A.16})$$

Note that the two forms of Langevin equations are equivalent. For the purposes of numerical integrations, in the Itô form, successive increments are evaluated at the *beginnings* of each time step, while they are evaluated at the *mid-points* of each time step in the Stranovich form. Readers may refer to Ref. [132, 133] for a more detailed discussion of the two forms of Langevin equations.

Appendix B

Generalized Einstein relation in thermal equilibrium

Consider a system of particles of arbitrary statistics characterized by a momentum distribution function $f(\mathbf{p}, t)$, whose evolution follows the aforementioned Fokker-Planck equation,

$$\frac{\partial f}{\partial t} = -\nabla_{\mathbf{p}} \cdot \left[\frac{1}{2}(1 + \lambda f)\mathbf{R}f \right] + \nabla_{\mathbf{p}} \cdot (\mathbf{D} \nabla_{\mathbf{p}} f), \quad (\text{B.1})$$

where $\lambda = -1, 0, +1$ correspond to fermions, classical particles and bosons, respectively. The thermal equilibrium momentum distribution function $f_{\text{eq}}(\mathbf{p}; T)$ at constant temperature T is stationary, and hence should be solutions to Eq. (B.1) in the absence of external fields.

The two terms on the right hand side of Eq. (B.1) can be identified with divergences of the dissipative momentum current $\mathbf{J}_{\text{diss}} = \mathbf{F}_{\text{fric}}f = \frac{1}{2}(1 + \lambda f)\mathbf{R}f$ and the diffusive momentum current $\mathbf{J}_{\text{diff}} = -\mathbf{D}\nabla f$. In thermal equilibrium, at any arbitrary location \mathbf{p} in momentum space, the

net momentum current must vanish: $\mathbf{J}_{\text{diss}}^{(\text{eq})}(\mathbf{p}) + \mathbf{J}_{\text{diff}}^{(\text{eq})}(\mathbf{p}) = \mathbf{0}$, i.e.,

$$\begin{aligned}\mathbf{J}_{\text{diss}}^{(\text{eq})} + \mathbf{J}_{\text{diff}}^{(\text{eq})} &= \frac{1}{2}(1 + \lambda f_{\text{eq}})\mathbf{R}_{\text{eq}}f_{\text{eq}} - \mathbf{D}_{\text{eq}}\nabla f_{\text{eq}} \\ &= \frac{1}{2}(1 + \lambda f_{\text{eq}})\mathbf{R}_{\text{eq}}f_{\text{eq}} \\ &\quad + \mathbf{D}_{\text{eq}}f_{\text{eq}}(1 + \lambda f_{\text{eq}})\frac{\mathbf{p}}{mk_{\text{B}}T} \\ &= \mathbf{0},\end{aligned}\tag{B.2}$$

which yields the *generalized Einstein relation* in thermal equilibrium,

$$\frac{\mathbf{D}_{\text{eq}}\mathbf{p}}{mk_{\text{B}}T} = -\frac{1}{2}\mathbf{R}_{\text{eq}}.\tag{B.3}$$

Note that the drift coefficient \mathbf{R}_{eq} and the diffusion tensor \mathbf{D}_{eq} are evaluated with the same equilibrium distribution f_{eq} at constant temperature T , and that this generalized Einstein relation holds true for all types of statistics. The relation can also be broken down into a component-wise form,

$$\frac{\sum_j D_{\text{eq}}^{ij} p^j}{-R_{\text{eq}}^i} = \frac{mk_{\text{B}}T}{2},\tag{B.4}$$

for $i = 1, 2$, and 3 .

Direct numerical integrations of the coefficients by definitions in Eq. (A.7) – (A.9) have also been performed to confirm the generalized Einstein relation in the thermal equilibrium limit.

Bibliography

- [1] J. Hong, *Bulk nuclear properties from dynamical description of heavy-ion collisions* (Michigan State University, 2016).
- [2] M. Colonna, Prog. Part. Nucl. Phys. (2020).
- [3] J. Xu, L.-W. Chen, M. B. Tsang, *et al.*, Phys. Rev. C **93**, 044609 (2016).
- [4] M. Colonna, A. Ono, and J. Rizzo, Phys. Rev. C **82**, 054613 (2010).
- [5] J. Colin, D. Cussol, J. Normand, N. Bellaize, R. Bougault, *et al.* (INDRA Collaboration), Phys. Rev. C **67**, 064603 (2003).
- [6] A. W. Steiner, M. Prakash, J. M. Lattimer, and P. J. Ellis, Phys. Rep. **411**, 325 (2005).
- [7] C. Y. Tsang, M. B. Tsang, P. Danielewicz, F. J. Fattoyev, and W. G. Lynch, Phys. Lett. B **796**, 1 (2019).
- [8] A. D. Panagiotou, M. W. Curtin, H. Toki, D. K. Scott, and P. J. Siemens, Phys. Rev. Lett. **52**, 496 (1984).
- [9] J. Pochodzalla, T. Möhlenkamp, T. Rubehn, A. Schüttauf, A. Wörner, E. Zude, M. Begemann-Blaich, T. Blaich, H. Emling, A. Ferrero, *et al.*, Phys. Rev. Lett. **75**, 1040 (1995).

- [10] S. D. Gupta, A. Z. Mekjian, and M. B. Tsang, in *Adv. Phys.* (Springer, 2001) pp. 89–166.
- [11] P. Chomaz, M. Colonna, and J. Randrup, *Phys. Rep.* **389**, 263 (2004).
- [12] P. Danielewicz, H. Lin, J. R. Stone, and Y. Iwata, arXiv preprint arXiv:1910.10500 (2019).
- [13] G. D. Westfall, J. Gosset, P. J. Johansen, A. M. Poskanzer, W. G. Meyer, H. H. Gutbrod, A. Sandoval, and R. Stock, *Phys. Rev. Lett.* **37**, 1202 (1976).
- [14] J. Cugnon, T. Mizutani, and J. Vademeulen, *Nucl. Phys. A* **352**, 505 (1981).
- [15] G. Bertsch and S. D. Gupta, *Phys. Rep.* **160**, 189 (1988).
- [16] R. Trockel, K. D. Hildenbrand, U. Lynen, W. Müller, H. J. Rabe, H. Sann, H. Stelzer, W. Trautmann, R. Wada, E. Eckert, *et al.*, *Phys. Rev. C* **39**, 729 (1989).
- [17] Y. D. Kim, M. B. Tsang, C. K. Gelbke, W. G. Lynch, N. Carlin, Z. Chen, R. Fox, W. G. Gong, T. Murakami, T. K. Nayak, *et al.*, *Phys. Rev. Lett.* **63**, 494 (1989).
- [18] E. Suraud, S. Ayik, J. Stryjewski, and M. Belkacem, *Nucl. Phys. A* **519**, 171 (1990).
- [19] P. Chomaz, G. F. Burgio, and J. Randrup, *Phys. Lett. B* **254**, 340 (1991).

- [20] G. F. Burgio, P. Chomaz, and J. Randrup, Nucl. Phys. A **529**, 157 (1991).
- [21] F. Chapelle, G. F. Burgio, P. Chomaz, and J. Randrup, Nucl. Phys. A **540**, 227 (1992).
- [22] W. Bauer, G. F. Bertsch, and S. D. Gupta, Phys. Rev. Lett. **58**, 863 (1987).
- [23] M. Colonna, M. D. Toro, A. Guarnera, *et al.*, Nucl. Phys. A **642**, 449 (1998).
- [24] P. Napolitani and M. Colonna, Phys. Lett. B **726**, 382 (2013).
- [25] Y.-X. Zhang, Y.-J. Wang, M. Colonna, P. Danielewicz, A. Ono, M. B. Tsang, H. Wolter, J. Xu, L.-W. Chen, D. Cozma, *et al.*, Phys. Rev. C **97**, 034625 (2018).
- [26] Y. M. Engel, D. M. Brink, K. Goeke, S. J. Krieger, and D. Vautherin, Nucl. Phys. A **249**, 215 (1975).
- [27] M. C. Cambiaggio, G. G. Dussel, and M. Saraceno, Nucl. Phys. A **415**, 70 (1984).
- [28] D. Lacroix and S. Ayik, Eur. Phys. J. A **50**, 95 (2014).
- [29] F. V. De Blasio, W. Cassing, M. Tohyama, P. F. Bortignon, and R. A. Broglia, Phys. Rev. Lett. **68**, 1663 (1992).
- [30] M. Tohyama and A. S. Umar, Phys. Rev. C **65**, 037601 (2002).
- [31] S. Ayik, Phys. Lett. B **658**, 174 (2008).
- [32] D. Lacroix and S. Ayik, Eur. Phys. J. A **50**, 95 (2014).

- [33] Y. P. Viyogi, T. J. M. Symons, P. Doll, *et al.*, Phys. Rev. Lett. **42**, 33 (1979).
- [34] D. R. Bowman, G. F. Peaslee, R. T. de Souza, N. Carlin, C. K. Gelbke, W. G. Gong, Y. D. Kim, M. A. Lisa, W. G. Lynch, L. Phair, M. B. Tsang, C. Williams, N. Colonna, K. Hanold, M. A. McMahan, G. J. Wozniak, L. G. Moretto, and W. A. Friedman, Phys. Rev. Lett. **67**, 1527 (1991).
- [35] W. Bauer, G. F. Bertsch, and S. Das Gupta, Phys. Rev. Lett. **58**, 863 (1987).
- [36] H. Kruse, B. V. Jacak, and H. Stöcker, Phys. Rev. Lett. **54**, 289 (1985).
- [37] A. Ono, H. Horiuchi, T. Maruyama, and A. Ohnishi, Prog. Theor. Phys. **87**, 1185 (1992).
- [38] A. Ono, H. Horiuchi, T. Maruyama, and A. Ohnishi, Phys. Rev. C **47**, 2652 (1993).
- [39] J. Su, F.-S. Zhang, and B.-A. Bian, Phys. Rev. C **83**, 014608 (2011).
- [40] J. Su and F.-S. Zhang, Phys. Rev. C **87**, 017602 (2013).
- [41] J. Su, K. Cherevko, W.-J. Xie, and F.-S. Zhang, Phys. Rev. C **89**, 014619 (2014).
- [42] C. Hartnack, Z.-X. Li, L. Neise, *et al.*, Nucl. Phys. A **495**, 303 (1989).
- [43] M. Papa, T. Maruyama, and A. Bonasera, Phys. Rev. C **64**, 024612 (2001).

- [44] M. Papa, Phys. Rev. C **87**, 014001 (2013).
- [45] Y.-X. Zhang and Z.-X. Li, Phys. Rev. C **74**, 014602 (2006).
- [46] Y.-X. Zhang, Z.-X. Li, and P. Danielewicz, Phys. Rev. C **75**, 034615 (2007).
- [47] Y.-X. Zhang, P. Danielewicz, M. Famiano, *et al.*, Phys. Lett. B **664**, 145 (2008).
- [48] Z.-Q. Feng, Phys. Rev. C **84**, 024610 (2011).
- [49] Z.-Q. Feng, Phys. Rev. C **85**, 014604 (2012).
- [50] X. G. Cao, G. Q. Zhang, X. Z. Cai, *et al.*, Phys. Rev. C **81**, 061603 (2010).
- [51] G. Q. Zhang, Y. G. Ma, X. G. Cao, *et al.*, Phys. Rev. C **84**, 034612 (2011).
- [52] W. B. He, Y. G. Ma, X. G. Cao, X. Z. Cai, and G. Q. Zhang, Phys. Rev. Lett. **113**, 032506 (2014).
- [53] D. T. Khoa, N. Ohtsuka, M. A. Matin, *et al.*, Nucl. Phys. A **548**, 102 (1992).
- [54] V. S. U. Maheswari, C. Fuchs, A. Faessler, *et al.*, Nucl. Phys. A **628**, 669 (1998).
- [55] K. Shekhter, C. Fuchs, A. Faessler, M. Krivoruchenko, and B. Martemyanov, Phys. Rev. C **68**, 014904 (2003).
- [56] M. D. Cozma, Y. Leifels, W. Trautmann, Q. Li, and P. Russotto, Phys. Rev. C **88**, 044912 (2013).

- [57] Q. Li, Z. Li, S. Soff, M. Bleicher, and H. Stocker, Phys. Rev. C **72**, 034613 (2005).
- [58] Q.-F. Li, C.-W. Shen, C.-C. Guo, *et al.*, Phys. Rev. C **83**, 044617 (2011).
- [59] P. Napolitani and M. Colonna, Phys. Rev. C **92**, 034607 (2015).
- [60] T. Gaitanos, A. B. Larionov, H. Lenske, and U. Mosel, Phys. Rev. C **81**, 054316 (2010).
- [61] A. B. Larionov, T. Gaitanos, and U. Mosel, Phys. Rev. C **85**, 024614 (2012).
- [62] O. Buss, T. Gaitanos, K. Gallmeister, *et al.*, Phys. Rep. **512**, 1 (2012).
- [63] F.-S. Zhang and E. Suraud, Phys. Rev. C **51**, 3201 (1995).
- [64] W.-J. Xie, J. Su, L. Zhu, and F.-S. Zhang, Phys. Rev. C **88**, 061601 (2013).
- [65] W.-J. Xie, J. Su, L. Zhu, and F.-S. Zhang, Phys. Lett. B **718**, 1510 (2013).
- [66] P. Danielewicz, Nucl. Phys. A **673**, 375 (2000).
- [67] B.-A. Li, L.-W. Chen, and C. M. Ko, Phys. Rep. **464**, 113 (2008).
- [68] C. Fuchs and H. H. Wolter, Nucl. Phys. A **589**, 732 (1995).
- [69] T. Gaitanos, M. D. Toro, S. Typel, *et al.*, Nucl. Phys. A **732**, 24 (2004).

- [70] G. Ferini, T. Gaitanos, M. Colonna, M. DiToro, and H. H. Wolter, Phys. Rev. Lett. **97**, 202301 (2006).
- [71] C. M. Ko and Q. Li, Phys. Rev. C **37**, 2270 (1988).
- [72] C. M. Ko and G. Q. Li, J. Phys. G **22**, 1673 (1996).
- [73] T. Song and C. M. Ko, Phys. Rev. C **91**, 014901 (2015).
- [74] A. Guarnera, M. Colonna, and P. Chomaz, Phys. Lett. B **373**, 267 (1996).
- [75] M. Colonna, Phys. Rev. Lett. **110**, 042701 (2013).
- [76] S. Ayik and C. Gregoire, Phys. Lett. B **212**, 269 (1988).
- [77] E. Suraud, S. Ayik, J. Stryjewski, and M. Belkacem, Nucl. Phys. A **519**, 171 (1990).
- [78] P. Danielewicz and G. Bertsch, Nucl. Phys. A **533**, 712 (1991).
- [79] R. J. Lenk and V. R. Pandharipande, Phys. Rev. C **39**, 2242 (1989).
- [80] P. Danielewicz, Physica A **100**, 167 (1980).
- [81] R. F. Pawula, Phys. Rev. **162**, 186 (1967).
- [82] N. L. Balazs, Physica A **94**, 474 (1978).
- [83] P. Ring and P. Schuck, *The nuclear many-body problem* (Springer Science & Business Media, 2004).
- [84] T. Hastie, R. Tibshirani, and J. Friedman, *The Elements of Statistical Learning: Data Mining, Inference, and Prediction* (Elsevier, 2017).

- [85] G. Q. Li, R. Machleidt, and Y. Z. Zhuo, Phys. Rev. C **48**, 1062 (1993).
- [86] P. Chomaz, M. Colonna, and J. Randrup, Phys. Rep. **389**, 263 (2004).
- [87] J. Rizzo, M. Colonna, and A. Ono, Phys. Rev. C **76**, 024611 (2007).
- [88] A. Ono, S. Hudan, A. Chbihi, and J. D. Frankland, Phys. Rev. C **66**, 014603 (2002).
- [89] W. J. Dou, G. H. Miao, and J. E. Subotnik, Phys. Rev. Lett. **119**, 046001 (2017).
- [90] D. J. Thouless, Nucl. Phys. **21**, 225 (1960).
- [91] H.-J. Mang, Phys. Rep. **18**, 325 (1975).
- [92] D. Gogny and P.-L. Lions, ESAIM: Math. Model. Numer. Anal. **20**, 571 (1986).
- [93] C. Ordóñez, L. Ray, and U. van Kolck, Phys. Rev. Lett. **72**, 1982 (1994).
- [94] R. Machleidt and D. R. Entem, J. Phys. G: Nucl. Part. Phys. **31**, S1235 (2005).
- [95] R. Machleidt and D. R. Entem, Phys. Rep. **503**, 1 (2011).
- [96] T. Tamura, W. R. Coker, and F. Rybicki, *Distorted Wave Born Approximation for Nuclear Reactions*, Tech. Rep. (Univ. of Texas, Austin, 1971).

- [97] L. L. Lee Jr, J. P. Schiffer, B. Zeidman, G. R. Satchler, R. M. Drisko, and R. H. Bassel, Phys. Rev. **136**, B971 (1964).
- [98] T. Tamura, Ann. Rev. Nucl. Sc. **19**, 99 (1969).
- [99] I. J. Thompson, Comp. Phys. Rep. **7**, 167 (1988).
- [100] N. Austern, Y. Iseri, M. Kamimura, M. Kawai, G. Rawitscher, and M. Yahiro, Phys. Rep. **154**, 125 (1987).
- [101] A. S. Umar and V. E. Oberacker, Phys. Rev. C **73**, 054607 (2006).
- [102] B. Avez, C. Simenel, and P. Chomaz, Phys. Rev. C **78**, 044318 (2008).
- [103] S. Ebata, T. Nakatsukasa, T. Inakura, K. Yoshida, Y. Hashimoto, and K. Yabana, Phys. Rev. C **82**, 034306 (2010).
- [104] J. A. Maruhn, P.-G. Reinhard, P. D. Stevenson, and A. S. Umar, Comp. Phys. Comm. **185**, 2195 (2014).
- [105] N. Loebel, A. S. Umar, J. A. Maruhn, P.-G. Reinhard, P. D. Stevenson, and V. E. Oberacker, Phys. Rev. C **86**, 024608 (2012).
- [106] J. Aichelin and G. Bertsch, Phys. Rev. C **31**, 1730 (1985).
- [107] Y.-X. Zhang, Y.-J. Wang, M. Colonna, P. Danielewicz, A. Ono, *et al.*, Phys. Rev. C **97**, 034625 (2018).
- [108] J. Aichelin and H. Stoecker, Phys. Lett. B **176**, 14 (1986).
- [109] J. Aichelin, Phys. Rep. **202**, 233 (1991).
- [110] Y. Kanada-En'yo, H. Horiuchi, and A. Ono, Phys. Rev. C **52**, 628 (1995).

- [111] A. Ono and H. Horiuchi, *Prog. Part. Nucl. Phys.* **53**, 501 (2004).
- [112] R. Wada, K. Hagel, J. Cibor, M. Gonin, T. Keutgen, M. Murray, J. B. Natowitz, A. Ono, J. C. Steckmeyer, A. Kerambrum, *et al.*, *Phys. Rev. C* **62**, 034601 (2000).
- [113] B. Borderie, G. Tăbăcaru, P. Chomaz, M. Colonna, A. Guarnera, M. Părlog, M. F. Rivet, G. Auger, C. O. Bacri, N. Bellaize, *et al.*, *Phys. Rev. Lett.* **86**, 3252 (2001).
- [114] J. Hong and P. Danielewicz, *Phys. Rev. C* **90**, 024605 (2014).
- [115] A. Rios, B. Barker, M. Buchler, and P. Danielewicz, *Ann. Phys. (N.Y.)* **326**, 1274 (2011).
- [116] P. Napolitani and M. Colonna, *Phys. Lett. B* **726**, 382 (2013).
- [117] H. Lin and P. Danielewicz, *Phys. Rev. C* **99**, 024612 (2019).
- [118] P. Danielewicz, *Ann. Phys. (N.Y.)* **152**, 239 (1984).
- [119] L. P. Kadanoff and G. Baym, New York (1962).
- [120] M. B. Tsang, J. R. Stone, F. Camera, P. Danielewicz, S. Gandolfi, K. Hebeler, C. J. Horowitz, J. Lee, W. G. Lynch, Z. Kohley, *et al.*, *Physical Review C* **86**, 015803 (2012).
- [121] A. Rios, B. Barker, and P. Danielewicz, in *J. Phys.: Conf. Ser.*, Vol. 427 (IOP Publishing, 2013) p. 012010.
- [122] M. H. Mahzoon, P. Danielewicz, and A. Rios, in *AIP Conf. Proc.*, Vol. 1912 (AIP Publishing, 2017) p. 020012.

- [123] H. Mahzoon, P. Danielewicz, and A. Rios, Eur. Phys. J. Special Topics **227**, 1949 (2019).
- [124] N. Schlünzen, S. Hermanns, M. Scharnke, and M. Bonitz, Journal of Physics: Condensed Matter **32**, 103001 (2019).
- [125] A. Bulgac, M. M. Forbes, K. J. Roche, and G. Wlazłowski, arXiv preprint arXiv:1305.6891 (2013).
- [126] H. Bruus and K. Flensberg, *Many-Body Quantum Theory in Condensed Matter Physics: An Introduction* (Oxford University Press, 2004).
- [127] P. Danielewicz, Ann. Phys. (N.Y.) **152**, 305 (1984).
- [128] O. Hen, G. A. Miller, E. Piasetzky, and L. B. Weinstein, Rev. Mod. Phys. **89**, 045002 (2017).
- [129] A. Rios, A. Polls, and W. H. Dickhoff, Phys. Rev. C **89**, 044303 (2014).
- [130] W. H. Dickhoff and D. Van Neck, *Many-Body Theory Exposed!: Propagator Description of Quantum Mechanics in Many-Body Systems Second Edition* (World Scientific Publishing Company, 2008).
- [131] R. Chandra, L. Dagum, D. Kohr, R. Menon, D. Maydan, and J. McDonald, *Parallel Programming in OpenMP* (Morgan Kaufmann, 2001).
- [132] N. V. Kampen, *Stochastic Processes in Physics and Chemistry (Third Edition)* (Elsevier, 2007) pp. 219 – 243.

[133] J. K. Hunter (2009), lecture notes (Math 280, University of California, Davis, Spring Quarter, 2009).